SCUOLA DI DOTTORATO
UNIVERSITÀ DEGLI STUDI DI MILANO-BICOCCA

Department of

FISICA G.OCCHIALINI

PhD program PHYSICS AND ASTRONOMY (FISICA E ASTRONOMIA) Cycle XXX

Curriculum ASTROPHYSICS (ASTROFISICA)

Whisper in the dark, scream in the light:
stellar twists and shouts when facing black holes

Surname MAINETTI Name DEBORAH

Registration number 727078

Tutors: Prof. Monica Colpi
Dr. Sergio Campana

Coordinator: Marta Calvi

ACADEMIC YEAR 2017/2018

Tutors:	Prof. M. Colpi	Università degli Studi di Milano Bicocca
	Dr. S. Campana	INAF – Osservatorio Astronomico di Brera
Reviewers:	Dr. G. Ghirlanda	INAF - Osservatorio Astronomico di Brera
	Prof. P.G. Jonker	SRON - Netherlands Institute for Space Research
Commettee:	Dr. E. Chassande-Mottin	Université Paris Diderot
	Prof. G. Lodato	Università degli Studi di Milano
	Prof. E. Rossi	Leiden Observatory, Netherlands

Milan, Italy, 2018 March

To Tam

Contents

Abstract

Quiescent massive black holes live at the centre of most galaxies. Sometimes they can accrete matter from the surroundings and become active. A contribution to the black hole turning on is given by the tidal disruption of stars orbiting around them. Indeed, stars in a galactic nuclear cluster stochastically interact with each other, increasing the probability for one of them to be scattered close enough to the central black hole to significantly feel its tidal influence. Basically, if the pericentre of the star around the black hole is less than about the so-called tidal radius, the star is completely disrupted. A fraction of the produced stellar debris circularises and accretes onto the black hole powering a characteristic flare.

Despite their scarcity and general sparseness in observations, about 70 candidates have been observed, mainly in the optical, UV and soft X-ray energy bands, thus allowing the detection of otherwise quiescent black holes. The discovery of new candidates is also important to check the theories about tidal disruption events through observations. About two years ago I classified XMMSL1J063045.9-603110 as a new candidate. Its peculiarity is to be likely associated with a very dim dwarf galaxy or even a very bright globular cluster hosting an intermediate-mass black hole. Intermediate-mass black holes are currently under study as the connecting bridge between stellar-mass and massive black holes and the raw material for

massive black holes, thus their detection would be extremely important.

Mostly, the literature of tidal disruption events deals with total tidal disruptions, but the appearance of tidal disruption flares is expected to depend on whether the star is fully or partially disrupted. Given the tidal radius definition, it first followed the need to define the effective demarcation line between total and partial disruptions. Guillochon & Ramirez-Ruiz (2013; 2015a) evaluated it through grid-based hydrodynamical simulations of tidal encounters between polytropic stars and black holes. Following their work, I investigated the same problem by comparing different simulation codes, which have different advantages and limits. The demarcation distance depended significantly on the chosen polytropic index (i.e. on the stellar internal structure), but only weakly on the adopted simulation method, provided a minimum resolution threshold.

As opposed to single stars, a great number of field stars are in binaries. Mandel & Levin (2015) demonstrated that under certain conditions both stars in a binary might be tidally disrupted in sequence immediately after the tidal binary break-up, thus powering a peculiar total accretion flare. Double-peaked light curves are expected to rise from double tidal disruptions. Via hydrodynamical simulations of double tidal disruptions, I demonstrated that kneed light curves, rather than double-peaked ones, can be more easily observed when decreasing the strength of the disruption and when elevating the mass difference between the binary components. I identified the first observational evidence of such events in PS16dtm. The detection of a knee can anticipate the onset of periodic flares if one of the binary components, only partially disrupted, remains bound to the black hole after binary separation.

List of Figures

List of Tables

Chapter 1

Sky Wars: the Black Holes awaken

-THERE ARE STORIES ABOUT WHAT HAPPENED.
- IT'S TRUE. ALL OF IT. THE DARK SIDE, THE JEDI. THEY'RE REAL.

Star Wars: the Force awakens

The formation and evolution processes of massive black holes (MBHs), which live in the centre of massive galaxies (e.g. Kormendy & Richstone 1995; Kormendy & Gebhardt 2001), are one of the main riddles in astrophysics today (e.g. Begelman et al. 2006; Volonteri 2010; Mayer 2017; Regan et al. 2017). It is commonly accepted that when these MBHs are settled at the centre of their host galaxies, they grow mainly by accretion of the surrounding gas and merging with smaller black holes (e.g. Soltan 1982; Yu & Tremaine 2002). Major inflows of gas drive the emission of huge amounts of energy that power active galactic nuclei (AGNs), even though AGNs typically have short duty cycles and galactic central MBHs are mostly in a low luminous state (Ho 2008). The lighting engine of a quiescent MBH can also be the tidal disruption of a star orbiting it (Rees 1988). Dynamical mechanisms in the nuclear star cluster increase the probability for a star to be scattered close

to the MBH on a low angular momentum orbit, in which it would experience the MBH tidal field (Alexander 2012; Merritt 2013). When the stellar self-gravity is no longer able to counteract the MBH tidal force, the star is disrupted (Hills 1975). Basically, a fraction of the resulting stellar debris is bound to the MBH, circularises and accretes onto it through an accretion disc. This triggers a bright peculiar flaring emission, lasting months to years (e.g. Rees 1988; Phinney 1989).

The critical pericentre distance of a star for tidal disruption is the BH tidal radius

$$r_{\rm t} \sim R_* \Big(\frac{M_{\rm BH}}{M_*}\Big)^{1/3} \sim 100{\rm R}_\odot \Big(\frac{R_*}{1{\rm R}_\odot}\Big)\Big(\frac{M_{\rm BH}}{10^6{\rm M}_\odot}\Big)^{1/3}\Big(\frac{1{\rm M}_\odot}{M_*}\Big)^{1/3}, \tag{1.1}$$

with R_* and M_* being the star radius and mass and $M_{\rm BH}$ the BH mass (Hills 1975; Frank & Rees 1976; Lacy et al. 1982). If

$$r_{\rm t} < r_{\rm s}, \tag{1.2}$$

where

$$r_{\rm s} = \frac{{\rm x}GM_{\rm BH}}{c^2} \sim 5{\rm R}_\odot \Big(\frac{M_{\rm BH}}{10^6{\rm M}_\odot}\Big)\Big(\frac{\rm x}{2}\Big) \tag{1.3}$$

is the BH event horizon radius (${\rm x} = 2$ for non-rotating BHs), the star enters the BH horizon before it is tidally disrupted and no flares are observable. For non-rotating BHs (Kesden 2012), Equation 1.2 implies that solar-type stars ($1{\rm M}_\odot$), white dwarfs ($1{\rm M}_\odot$) and giant stars ($5{\rm M}_\odot$) are swallowed entirely if $M_{\rm BH}$ is greater than $10^8{\rm M}_\odot$, $10^5{\rm M}_\odot$ and $10^{10}{\rm M}_\odot$, respectively. In contrast, less massive BHs in quiescent (or low-luminous) galaxies can be inferred from the observation of tidal disruption flares.

Tidal disruption events are theoretically and observationally estimated to occur at a rate of about $10^{-4} - 10^{-5}\ {\rm galaxy}^{-1}\ {\rm yr}^{-1}$ (e.g. Magorrian & Tremaine 1999;

Donley et al. 2002; Wang & Merritt 2004; Brockamp et al. 2011; Khabibullin & Sazonov 2014; Stone & Metzger 2016). Although they are rare and often observations are sparse, several candidates have been discovered to date[1], mainly in the optical, UV and soft X-ray bands (e.g. Gezari 2012; Komossa 2012; 2015 and references therein), where the peak of an accretion disc emission lies (e.g. Ulmer 1999), but also in the radio and hard X-ray bands (e.g. Bloom et al. 2011; Cenko et al. 2012b; Brown et al. 2015). Many theoretical studies have been carried out to better understand the physics of tidal disruption events and model their associated emission, considering stars approaching the BH on a variety of orbits, from parabolic to bound, and also sometimes including general relativistic effects (e.g. Nolthenius & Katz 1982; Bicknell & Gingold 1983; Carter & Luminet 1983; 1985; Luminet & Marck 1985; Luminet & Carter 1986; Evans & Kochanek 1989; Luminet & Pichon 1989; Cannizzo et al. 1990; Khokhlov et al. 1993a; 1993b; Laguna et al. 1993; Diener et al. 1995; 1997; Ivanov & Novikov 2001; Kobayashi et al. 2004; Brassart & Luminet 2008; 2010; Rosswog et al. 2008; 2009; Guillochon et al. 2009; Lodato et al. 2009; Ramirez-Ruiz & Rosswog 2009; Strubbe & Quataert 2009; 2011; Kasen & Ramirez-Ruiz 2010; Lodato & Rossi 2011; Amaro-Seoane et al. 2012; MacLeod et al. 2012; 2013; Guillochon & Ramirez-Ruiz 2013; 2015a; 2015b; Hayasaki et al. 2013; 2016; Dai et al. 2015; Piran et al. 2015; Shiokawa et al. 2015; Bonnerot et al. 2016; Bonnerot et al. 2017).

This chapter begins with an overview of the dynamical mechanisms in nuclear star clusters which favour the occurrence of stellar tidal disruption events. It continues with an inspection of the disruption phase itself, to turn then to the

[1] https://tde.space

circularisation, accretion and emission phases. Particularly, it lingers on the possible sources of emission at different wavelengths. Chapter 2 is a review of the tidal disruption candidates discovered so far. Chapter 3 deeply analyses a peculiar candidate. Chapter 4 introduces the distinction between total and partial tidal disruption events. Chapter 5 deals with the tidal disruption of stellar binaries, instead of single stars. The presentation of the first likely disruption of a stellar binary ever observed appears in chapter 6. Chapter 7 sums up results and conclusions.

1.1 Notes on the loss-cone theory

A star (M_*, R_*) orbiting a BH ($M_{\rm BH}$) on a nearly parabolic Keplerian trajectory of semi-major axis a and eccentricity e, with specific energy and specific angular momentum of moduli

$$\epsilon = \frac{GM_{\rm BH}}{2a} \tag{1.4}$$

and

$$j = \sqrt{GM_{\rm BH}r_{\rm p}(1+e)}, \tag{1.5}$$

respectively, will reach its pericentre inside the BH tidal radius ($r_{\rm p} < r_{\rm t}$; Equation 1.1) if j is less than the so-called loss-cone specific angular momentum ($j < j_{\rm LC}$), of modulus

$$j_{\rm LC} = \sqrt{GM_{\rm BH}r_{\rm t}(1+e)}. \tag{1.6}$$

Basically, the loss-cone is a set of stellar orbital velocity directions which lead to $r_{\rm p} < r_{\rm t}$ (Figure 1.1). Stars on these loss-cone orbits will be tidally disrupted by the BH roughly in an orbital period

$$P = \frac{2\pi a^{3/2}}{\sqrt{GM_{\rm BH}}}. \tag{1.7}$$

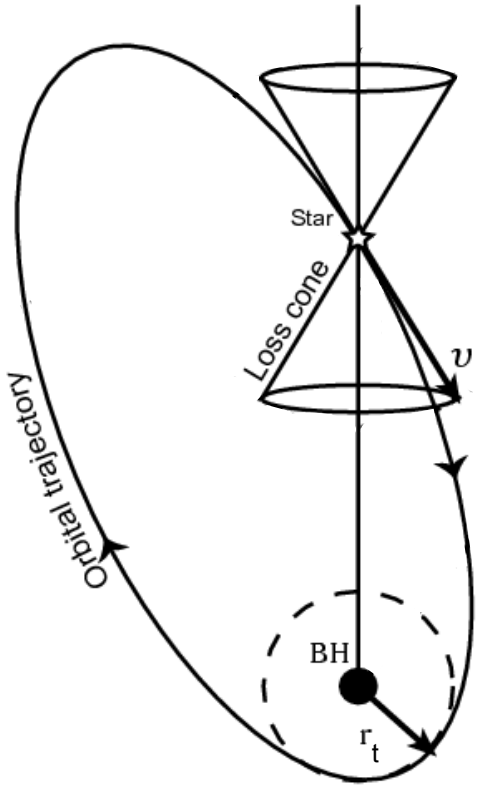

Figure 1.1: Simple representation of the loss-cone, readapted from Merritt (2013).

Thus, the rate of tidal disruption events will depend on the efficiency of some dynamical mechanisms in repopulating loss-cone orbits (Alexander 2012).

Stars in a galactic nucleus are scattered by stochastic two-body gravitational encounters with other stars. For stars on highly eccentric orbits ($e \lesssim 1$), the time ($t_{\rm r}$) for an order unity change in orbital specific energy (change in the orbital size) is significantly longer than the time ($t_{\rm j}$) it takes the orbital specific angular momentum to change by order unity (change in the orbital size and shape). Particularly,

$$t_{\rm j} \sim \left(\frac{j}{j_{\rm c}}\right)^2 t_{\rm r} \sim (1-e^2) t_{\rm r}, \tag{1.8}$$

where

$$j_{\rm c} = \sqrt{GM_{\rm BH}a}, \tag{1.9}$$

is the specific circular angular momentum, i.e. the maximum specific angular momentum for that orbit. $t_{\rm r}$ is also the time it takes j to change by order $j_{\rm c}$. Thus, stars are expected to be scattered onto loss-cone orbits more by relaxation of angular momentum than by relaxation of energy (e.g. Merritt 2013; Stone 2013).

However, the repopulation of loss-cone orbits through this mechanism occurs in two different regimes (e.g. Frank & Rees 1976; Lightman & Shapiro 1977). Close to the BH (empty loss-cone regime), the angular opening of the loss-cone is large compared to the total deflection of a star over an orbital period ($\Delta j << j_{\rm LC}$). Such a star typically would take much time to get into the loss-cone and be disrupted, and when this happens it has $\beta \sim 1$, where the impact parameter β is defined as

$$\beta = \frac{r_{\rm t}}{r_{\rm p}}. \tag{1.10}$$

Far from the BH (full loss-cone regime), the angular opening of the loss-cone is smaller than the stellar total deflection over an orbital period ($\Delta j >> j_{\rm LC}$). In this regime, stars will jump in and out from the loss-cone many times during one orbital period and will be tidally disrupted with a wider range of β values (Figure 1.2, readapted from Alexander 2012). The critical distance from the BH $r_{\rm cr}$ which separates the two loss-cone regimes can be evaluated by placing $\Delta j = j_{\rm LC}$ in

$$\frac{\Delta j}{j_{\rm c}} \sim \left(\frac{P}{t_{\rm r}}\right)^{1/2} \tag{1.11}$$

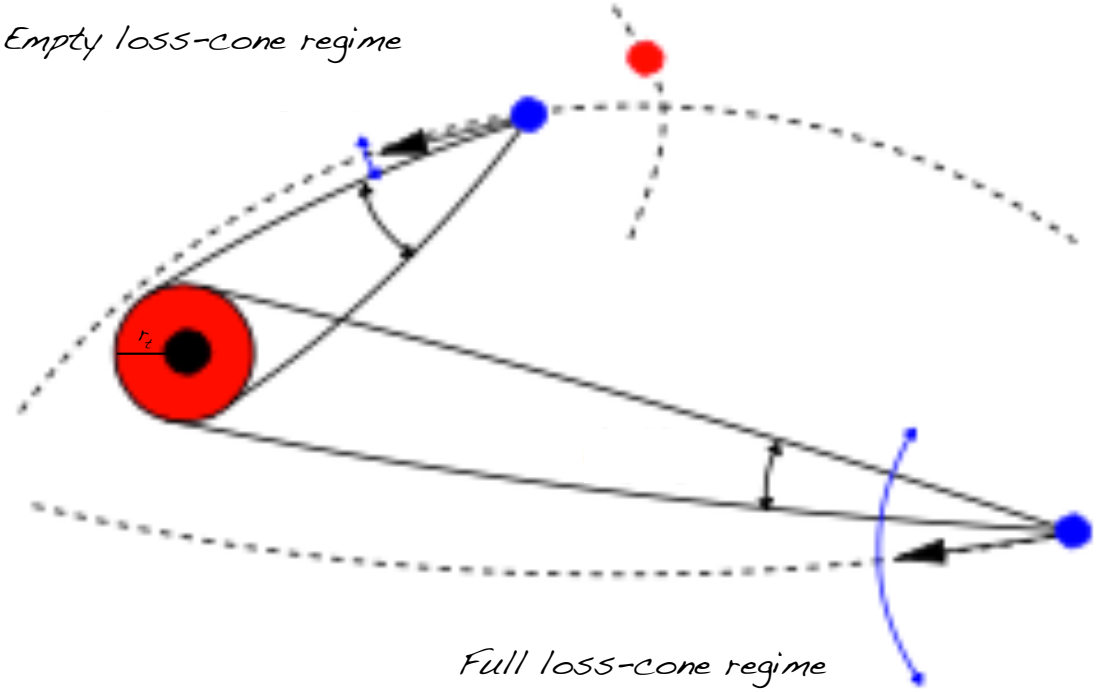

Figure 1.2: A star (blue dot) is deviated from its original orbit (dashed curve) around a BH (black dot) when interacting with a field star (red dot). In the empty loss-cone regime (that is, close to the BH), the star total deviation over an orbital period (blue double arrow) is small compared to the loss-cone angular opening (black double arrow), meaning that such a star generally will take much longer to diffuse into the loss-cone than to reach the BH. In the full loss-cone regime (that is, far from the BH), the star total deviation over an orbital period is great with respect to the loss-cone angular opening. In this case, the star is rapidly kicked into the loss-cone.

(e.g. Merritt 2013). To first approximation, by considering circular orbits and by setting

$$t_{\rm r} \sim \frac{0.34\sigma^3}{G^2 M_* \rho(r) \ln\Lambda} \tag{1.12}$$

(Spitzer 1987), where σ is the one-dimensional stellar velocity dispersion, $\rho(r)$ is the stellar mass density and $\ln\Lambda \sim \ln(M_{\rm BH}/M_*)$ is the Coulomb logarithm, Equation 1.11 for $r_{\rm cr}$ becomes

$$\frac{r_{\rm t}}{r_{\rm cr}} \sim \frac{2\pi G^{3/2} M_* \rho(r_{\rm cr}) r_{\rm cr}^{3/2} \ln\Lambda}{0.34\sqrt{M_{\rm BH}}\sigma^3}. \tag{1.13}$$

Using Equation 1.1 and choosing a singular isothermal sphere density profile $\rho(r) = \sigma^2/(2\pi G r^2)$, Equation 1.13 gets

$$r_{\rm cr} \sim \Big(\frac{0.34\sigma M_{\rm BH}^{5/6} R_*}{\sqrt{G} M_*^{4/3} \ln\Lambda}\Big)^2 \sim 1.3\times10^5 {\rm R}_\odot \Big(\frac{\sigma}{70{\rm km/s}}\Big)^2 \Big(\frac{M_{\rm BH}}{10^6{\rm M}_\odot}\Big)^{5/3} \Big(\frac{R_*}{1{\rm R}_\odot}\Big)^2 \times \Big(\frac{1{\rm M}_\odot}{M_*}\Big)^{8/3} \Big(\frac{15}{\ln\Lambda}\Big)^2, \tag{1.14}$$

where σ can be derived from Ferrarese & Ford (2005). This critical radius, from where most tidally disrupted stars originate (Magorrian & Tremaine 1999), is smaller than the radius of gravitational influence of the BH

$$r_{\rm h} = \frac{G M_{\rm BH}}{\sigma^2} \sim 3.9\times10^7 {\rm R}_\odot \Big(\frac{M_{\rm BH}}{10^6{\rm M}_\odot}\Big)\Big(\frac{70{\rm km/s}}{\sigma}\Big)^2 \tag{1.15}$$

(Peebles 1972) for a BH of mass $10^6{\rm M}_\odot$, but becomes comparable to $r_{\rm h}$ for a BH of mass $10^8{\rm M}_\odot$.

In the assumption (hitherto supposed) of spherical galaxies, composed of stars of equal masses (M_*) and radii (R_*) distributed according to a singular isothermal sphere density profile, the rate of tidal disruption events due to two-body stellar gravitational encounters is roughly 10^{-4} galaxy^{-1} yr^{-1} (Magorrian & Tremaine 1999; Wang & Merritt 2004).

Well inside $r_{\rm h}$ (Equation 1.15), but not too close to the BH, the BH gravitational influence is dominant and the stellar orbits are nearly Keplerian ellipses with

different orientations, which do not experience precession for many orbital periods ($t < t_{\rm prec}$). Averaged over this time, stars can be represented as elliptical wires, whose masses are distributed along them in proportion to the time spent there. These wires exert mutual coherent torques over $t_{\rm prec}$, leading to rapid resonant relaxation of the specific angular momenta. After $t_{\rm prec}$, precession due to the stellar potential or general relativity breaks the coherence and the change in specific angular momenta is described by a random walk (Rauch & Tremaine 1996). This process increases the tidal disruption rate in the empty loss-cone, but not in the full loss-cone, and leads to an only modest enhancement of the overall tidal disruption rate, given that most tidally disrupted stars originate from $r_{\rm cr} \lesssim r_{\rm h}$ (Rauch & Ingalls 1998).

Less symmetry in the stellar potential should allow for more freedom in orbital evolution, i.e. maybe more efficiency in repopulating loss-cone orbits. However, Magorrian & Tremaine (1999) demonstrate that axisymmetric systems do not significantly enhance the tidal disruption rate, while in triaxial potentials the large number of stars on chaotic orbits (Poon & Merritt 2004) could increase the tidal disruption rate by a factor of $\sim 10 - 100$ (Merritt & Poon 2004), but it is not clear whether such chaotic orbits exist in the presence of the BH.

Stellar orbits in a galactic nucleus can also be perturbed by massive objects, such as giant molecular clouds or star clusters. Two-body relaxation by these massive perturbers dominates over two-body relaxation by stars provided that they are numerous enough (Perets et al. 2007). This occurs far from the BH, where the loss-cone would however be full due to stellar two-body encounters alone, and poorly near the BH, where stellar two-body encounters are not able to efficiently refill the so empty loss-cone. Thus, this process does not significantly enhance the

total tidal disruption rate.

Hardening, unequal-mass central BH binaries are efficient disruptors. Kozai effects on stellar orbits around the primary (i.e. more massive) BH induced by the secondary BH (Ivanov et al. 2005) and chaotic three-body interactions (Chen et al. 2009; 2011) can lead to a short-lived phase of very high tidal disruption rate. This translates into a contribution of $\sim 10\%$ to all tidal disruption events (Chen et al. 2011). Also, the merger of binary BHs, accompanied by gravitational wave emission, can promptly refill the loss-cone and briefly increase the tidal disruption rate due to the recoil imparted to the produced BH (Stone & Loeb 2011).

The last channel, here presented, for stellar tidal disruptions arises when central BHs tidally separate stellar binaries (Hills 1988). A high number of field stars are in binary systems (e.g. Heintz 1969; Abt & Levy 1976; Abt 1983; Duquennoy & Mayor 1991; Fischer & Marcy 1992). However, the high central densities and velocity dispersions present in galactic nuclei reduce the number of them. Indeed, most binaries are 'soft', i.e. the relative velocity of their components is much smaller than the velocities of the field stars, and thus they can be separated via close encounters with other stars over the galaxy lifetime (Merritt 2013). On the contrary, some binaries are 'hard' enough, which also means close enough, to survive encounters with field stars for a longer time. A hard binary on a parabolic orbit around a BH is then tidally broken-up if its centre of mass around the BH enters a sphere of radius

$$r_{\rm tb} \sim a_{\rm bin}\Big(\frac{M_{\rm BH}}{M_{\rm bin}}\Big)^{1/3} \sim 10^3{\rm R}_\odot\Big(\frac{a_{\rm bin}}{10{\rm R}_\odot}\Big)\Big(\frac{M_{\rm BH}}{10^6{\rm M}_\odot}\Big)^{1/3}\Big(\frac{1{\rm M}_\odot}{M_*}\Big)^{1/3}, \qquad (1.16)$$

where $a_{\rm bin}$ and $M_{\rm bin}$ are the binary semi-major axis and total mass (e.g. Miller et al. 2005). It is worth noting that binary break-up comes before single-star tidal

disruptions, given that $r_{\rm tb} > r_{\rm t}$ (Equations 1.16 and 1.1). After binary separation, traditionally one star is ejected at high speed (e.g. Hills 1988), while the other becomes bound to the BH, and its subsequent orbital evolution determines whether it will be tidally disrupted (Amaro-Seoane et al. 2012). Starting from the significant rate inferred for tidal binary break-ups (Bromley et al. 2012), the rate of bound tidally disrupted stars will depend on dynamical mechanisms involved in stellar orbital evolution.

1.2 The physics of tidal disruptions

Actually, a star approaching the central BH of a galaxy on a loss-cone orbit may be swallowed whole by the compact object or be tidally disrupted outside the BH horizon. The latter event occurs if the so-called BH tidal radius $r_{\rm t}$ (Equation 1.1), which corresponds to the distance where the BH tidal force ($GM_{\rm BH}M_*R_*/r^3$) equates the star self-gravity at its surface (GM_*^2/R_*^2), is greater than the BH event horizon radius $r_{\rm s}$ (Equation 1.3), that is, if

$$M_{\rm BH} < \frac{c^3}{({\rm x}G)^{3/2}}\frac{R_*^{3/2}}{M_*^{1/2}} \sim 10^8{\rm M}_\odot\Big(\frac{R_*}{1{\rm R}_\odot}\Big)^{3/2}\Big(\frac{1{\rm M}_\odot}{M_*}\Big)^{1/2}\Big(\frac{2}{\rm x}\Big)^{3/2}. \qquad (1.17)$$

Equation 1.17 for non-rotating BHs (${\rm x} = 2$) implies that solar-type stars, white dwarfs and giant stars are entirely swallowed if $M_{\rm BH}$ exceeds $10^8{\rm M}_\odot$, $10^5{\rm M}_\odot$ and $10^{10}{\rm M}_\odot$, respectively, while less massive otherwise quiescent or low-luminous BHs can be revealed from the observation of tidal disruption flares.

In this regime, the star is completely disrupted if its pericentre distance $r_{\rm p}$ is shorter than about $r_{\rm t}$ (e.g. Hills 1975). Most of the stars in a galaxy fated to be disrupted by the central BH are scattered onto low angular momentum orbits from about the BH sphere of influence, that is, onto nearly parabolic trajectories

(Magorrian & Tremaine 1999; Wang and Merritt 2004). For this reason, much effort has been spent in considering parabolic encounters. Within these limits, the star is distorted assuming the configuration of a rugby ball, that is, stretched in the orbital direction towards the BH and compressed perpendicularly, and differentially torqued, that is, spun-up (Evans & Kochanek 1989; Khokhlov et al. 1993a; 1993b; Guillochon et al. 2009). Nearly half of the resulting stellar debris after disruption is scattered onto highly eccentric orbits bound to the BH (Lacy et al. 1982; Rees 1988; Ayal et al. 2000) with a spread in the orbital specific energies of

$$\Delta\epsilon \sim \frac{GM_{\rm BH}R_*}{r_{\rm t}^2} \tag{1.18}$$

(Stone et al. 2013). The other half of stellar debris leaves the system on hyperbolic orbits (Figure 1.3). The first returning time at pericentre of the bound debris depends on their new orbital energy through Kepler's third law, and for the most bound material it is

$$t_{\rm min} = \frac{\pi}{\sqrt{2}}\frac{GM_{\rm BH}}{\Delta\epsilon^{3/2}} \sim 40{\rm d}\Big(\frac{R_*}{1{\rm R}_\odot}\Big)^{3/2}\Big(\frac{M_{\rm BH}}{10^6{\rm M}_\odot}\Big)^{1/2}\Big(\frac{1{\rm M}_\odot}{M_*}\Big). \tag{1.19}$$

The rate of material returning at pericentre is

$$\dot{M}(t) = \frac{dM}{dt} = \frac{dM}{d\epsilon}\frac{d\epsilon}{dt} = \frac{(2\pi GM_{\rm BH})^{2/3}}{3}\frac{dM}{d\epsilon}t^{-5/3}. \tag{1.20}$$

Here $dM/d\epsilon$, which is the distribution of the bound debris mass in orbital specific energy ϵ as a function of ϵ (i.e., t, the time since disruption), is not exactly uniform (Lodato et al. 2009; Guillochon & Ramirez-Ruiz 2013; 2015a), but, to a first approximation, it can be considered as such (Rees 1988; Evans & Kochanek 1989; Phinney 1989). Considering that half of the stellar debris is bound to the BH after disruption and using Equation 1.19, the returning rate trend starting from

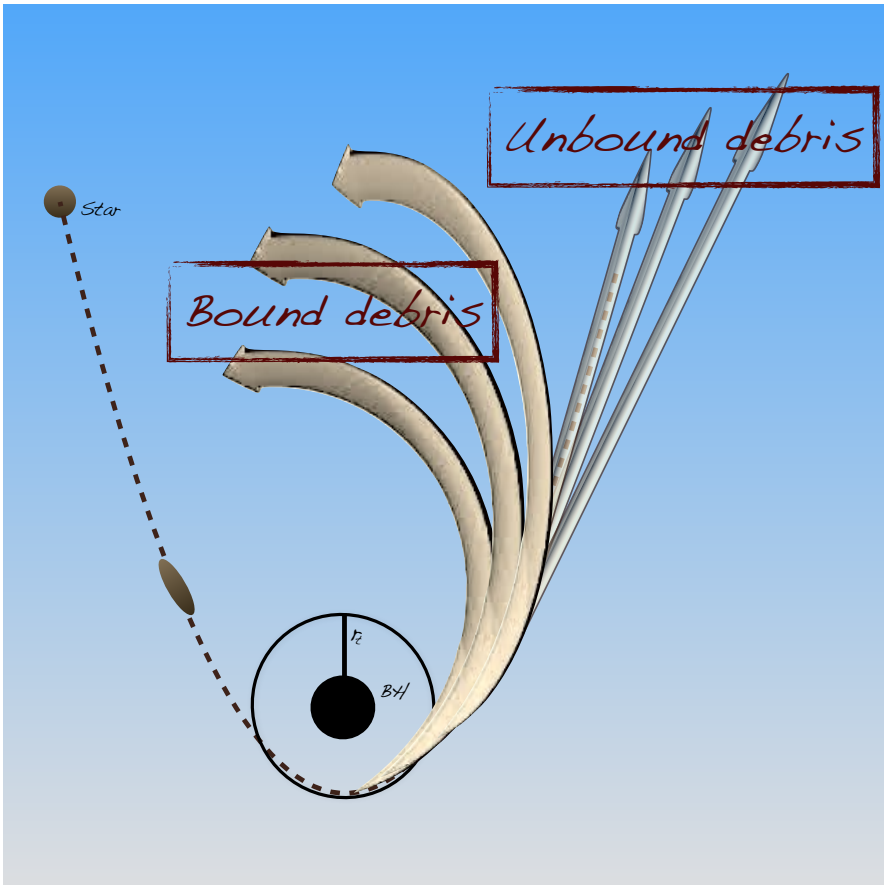

Figure 1.3: A star orbiting the central BH of a galaxy on a nearly parabolic loss-cone orbit ($r_{\rm p} \lesssim r_{\rm t}$) is tidally disrupted by the BH outside its event horizon if $r_{\rm t} > r_{\rm s}$. About half of the produced stellar debris remains bound to the BH in a range of highly eccentric orbits, while the other half escapes the system on hyperbolic trajectories.

$t_{\rm peak} \sim 1.5 t_{\rm min}$ (Evans & Kochanek 1989) reads

$$\dot{M}(t) \sim \frac{(2\pi G M_{\rm BH})^{2/3}}{3} \frac{M_*/2}{\Delta\epsilon} t^{-5/3} \sim \frac{2}{3} \frac{M_*/2}{t_{\rm min}} \left(\frac{t}{t_{\rm min}}\right)^{-5/3}$$
$$\sim 3.0 {\rm M}_\odot {\rm yr}^{-1} \left(\frac{R_*}{1{\rm R}_\odot}\right) \left(\frac{M_{\rm BH}}{10^6 {\rm M}_\odot}\right)^{1/3} \left(\frac{M_*}{1{\rm M}_\odot}\right)^{1/3} \left(\frac{t}{0.11{\rm yr}}\right)^{-5/3}. \quad (1.21)$$

Throughout this section some specifics have been neglected and some approximations have been assumed as a simplification. First of all, the critical BH mass above which a star on a loss-cone orbit is directly captured into the BH horizon depends on the value of the BH spin, as well as on the stellar mass and radius (Equation 1.17; Kesden 2012). Let's consider a solar-type star on a parabolic loss-cone orbit. In the Newtonian regime, the critical BH mass for a non-spinning BH ($\mathrm{x} = 2$ in Equation 1.17) comes out to be $\sim 10^8 \mathrm{M}_\odot$. In the general relativistic regime, however, such a critical mass drops to $\sim 4 \times 10^7 \mathrm{M}_\odot$ ($\mathrm{x} = 4$ in Equation 1.17; Bardeen et al. 1972). Maximally spinning BHs of masses greater than $\sim 3 \times 10^8 \mathrm{M}_\odot$ and $\sim 2 \times 10^7 \mathrm{M}_\odot$, instead, wholly swallowed the mentioned star when orbiting the BH progradely ($\mathrm{x} = 1$) and retrogradely ($\mathrm{x} = 5.83$), respectively (Bardeen et al. 1972).

Secondly, it has to be noted that when $r_\mathrm{p} << r_\mathrm{t}$ (but still assuming that the Newtonian approximation works), the star should be highly compressed perpendicularly to the orbital plane by the influence of the BH, during its pericentre passage. The strong compression enhances the central temperature and density of the star to the point that thermonuclear reactions could be triggered (e.g. Carter & Luminet 1983; Brassart & Luminet 2008). The subsequent energy release might change the expected spread in the debris orbital specific energies (Equation 1.18), but such a contribution results to be small compared to $\Delta\epsilon$ (Luminet & Pichon 1989). The strong compression is also expected to be followed by a rebound due to the progressive buildup of the stellar internal pressure. This leads to the production of shock waves propagating outward through the star, that eventually breaks out in a short (actually still never observed) X-ray outburst (Guillochon et al. 2009). The analysis of general relativistic tidal disruption events reveals that the star should be multiply compressed by the increased BH influence in this regime (e.g. Luminet &

Marck 1985; Laguna et al. 1993; Brassart & Luminet 2010).

Finally, as already said, the distribution of the bound stellar debris mass in

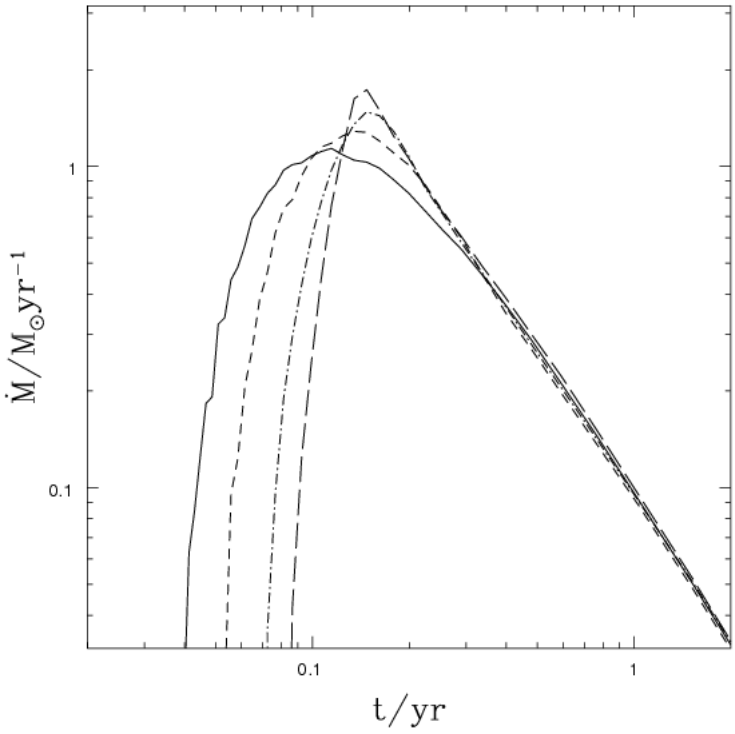

Figure 1.4: Rate of debris returning at pericentre after the disruption of a polytropic star (in units of $\mathrm{M}_\odot\mathrm{yr}^{-1}$) as a function of time (in units of yr) from Lodato et al. (2009). The adopted polytropic indexes are $\gamma = 1.4$ (solid curve), $\gamma = 1.5$ (short-dashed curve), $\gamma = 5/3$ (dot-dashed curve) and $\gamma = 1.8$ (long-dashed curve). More centrally concentrated stars (lower γ) show more gently rising and shallower trends.

orbital specific energies $dM/d\epsilon$ in Equation 1.20 is not exactly uniform. This will somehow affect the debris returning rate trend evaluated in Equation 1.21. According to Lodato et al. (2009), this distribution in the orbital specific energies ϵ

depends on the stellar internal structure. They state that the more the fully disrupted star was centrally concentrated, the more it peaks at lower ϵ (i.e. more debris less bound to the BH), at least at early times. This translates into a shallower, as well as gently rising, returning rate trend with respect to Equation 1.21 (Figure 1.4). These authors only mention the dependence of the bound debris mass distribution in ϵ on the impact parameter β (Equation 1.10), which is fully treated by Guillochon & Ramirez-Ruiz (2013; 2015a). This paper will be recovered later in this thesis, when partial tidal disruption events will be taken into account.

1.3 The circularisation and accretion phases

For years it has been assumed, but far from established, that after a few $t_{\rm min}$ (Equation 1.19) the debris returned at pericentre circularise into an accretion disc, extending to $\sim 2r_{\rm p}$, via energy dissipation, caused by shocks induced by the debris stream intersections (e.g. Ulmer 1999). With this assumption, if the viscous time, i.e. the accretion time,

$$t_{\rm v} \sim \frac{t_{\rm Kep}(2r_{\rm p})}{\alpha\pi h^2} \sim \frac{2^{5/2}R_*^{3/2}}{G^{1/2}M_*^{1/2}\alpha h^2}\beta^{-3/2} \tag{1.22}$$

(Ulmer 1999), where $t_{\rm Kep}(2r_{\rm p})$ is the Keplerian orbital period at $2r_{\rm p}$, α the viscous disc parameter (Shakura & Sunyaev 1973), h the disc half-height divided by its radius and $\beta \gtrsim 1$ (total disruptions), is smaller than $t_{\rm min}$, meaning that their ratio

$$\frac{t_{\rm v}}{t_{\rm min}} \sim 0.025\Big(\frac{0.1}{\alpha}\Big)h^{-2}\Big(\frac{M_*}{1{\rm M}_\odot}\Big)^{1/2}\Big(\frac{10^6{\rm M}_\odot}{M_{\rm BH}}\Big)^{1/2}\beta^{-3/2} \tag{1.23}$$

is low, the rate of debris returning at pericentre $\dot{M}(t)$ (Equation 1.20) coincides to a good approximation with the rate of material accreting onto the BH. The thicker the accretion disc is (i.e., $h \to 1$), the better this approximation works. The luminosity

produced by accretion can therefore be evaluated as

$$\begin{aligned} L(t) &\sim \eta \dot{M}(t) c^2 \\ &\sim 2 \times 10^{46} \frac{\mathrm{erg}}{\mathrm{s}} \Big(\frac{\eta}{0.1}\Big) \Big(\frac{R_*}{1\mathrm{R}_\odot}\Big) \Big(\frac{M_{\mathrm{BH}}}{10^6\mathrm{M}_\odot}\Big)^{1/3} \Big(\frac{M_*}{1\mathrm{M}_\odot}\Big)^{1/3} \Big(\frac{t}{0.11\mathrm{yr}}\Big)^{-5/3} \end{aligned} \tag{1.24}$$

(where η is the radiation efficiency and $\dot{M}(t)$ comes from Equation 1.21), again starting from t_{peak}. However, the accretion peak luminosity L_{peak} turns out to be a factor of ~ 100 super-Eddington for $M_{\mathrm{BH}} = 10^6\mathrm{M}_\odot$, $M_* = 1\mathrm{M}_\odot$, $R_* = 1\mathrm{R}_\odot$ and $\eta = 0.1$ ($L_{\mathrm{Edd}} \sim 1.3 \times 10^{44} \mathrm{erg\,s^{-1}} (M_{\mathrm{BH}}/10^6\mathrm{M}_\odot)$), which means that probably a fraction of the accreting mass is ejected in a wind from the disc at early times, that is before

$$\begin{aligned} t_{\mathrm{Edd}} &= \Big(\frac{2^{1/3} G^{1/3} 3 \dot{M}_{\mathrm{Edd}}}{\pi^{2/3} M_{\mathrm{BH}}^{1/3} M_*^{1/3} R_*}\Big)^{-3/5} \\ &\sim 2.1\mathrm{yr} \Big(\frac{10^6\mathrm{M}_\odot}{M_{\mathrm{BH}}}\Big)^{2/5} \Big(\frac{\eta}{0.1}\Big)^{3/5} \Big(\frac{M_*}{1\mathrm{M}_\odot}\Big)^{1/5} \Big(\frac{R_*}{1\mathrm{R}_\odot}\Big)^{3/5}, \end{aligned} \tag{1.25}$$

where Equation 1.21 has been used expliciting t_{min} and setting

$$\dot{M}(t = t_{\mathrm{Edd}}) = \dot{M}_{\mathrm{Edd}} = \frac{L_{\mathrm{Edd}}}{\eta c^2} \tag{1.26}$$

(Strubbe & Quataert 2009; 2011; Lodato & Rossi 2011).

In the context of debris circularisation, however, two mechanisms must be considered (Kochanek 1994). The first mechanism is apsidal (in-plane) general relativistic precession, which should allow the intersection of the debris on their second return at pericentre with the debris still on their first return. The greater the rate of precession is, the closer to the BH intersections occur and circularising material is deposited and the stronger the resulting shocks are (that is, the quicker circularisation is) (e.g. Hayasaki et al. 2013; Dai et al. 2015; Bonnerot et al. 2016).

The second mechanism is nodal (out-of-plane) general relativistic precession from Lense-Thirring torques around spinning BHs, which could even strongly delay intersections. According to Guillochon & Ramirez-Ruiz (2015b), when general relativistic effects are weak, that is for less massive BHs ($M_{\rm BH} \lesssim 10^6 {\rm M}_\odot$) the debris intersections and deposit occur far from the BH, resulting in a long circularisation time and viscous time (Equation 1.22) and then in a slowdown and lowering of the accretion rate with respect to the debris returning rate at pericentre (Shiokawa et al. 2015). The outcoming accretion peak luminosity, then, will not exceed the BH Eddington luminosity and the accretion luminosity will decay shallower than in Equation 1.24. For more massive non-spinning BHs, the debris intersections and deposit take place nearer the BH, allowing the accretion rate to resemble the returning rate. For massive and spinning BHs, the debris intersections and deposit, even if occurring near the BH, are delayed, and the accretion rate approximately follows the returning rate but with a fixed time delay $t_{\rm delay}$. Similar results are discussed also by Hayasaki et al. (2016). Given that, from Equation 1.24 evaluated at $t = t_{\rm peak} \sim 1.5 t_{\rm min} \propto M_{\rm BH}^{1/2}$ (or $t = t_{\rm peak} + t_{\rm delay}$) and from $L_{\rm Edd} \propto M_{\rm BH}$,

$$\frac{L_{\rm peak}}{L_{\rm Edd}} \propto \frac{M_{\rm BH}^{-1/2}}{M_{\rm BH}} \propto M_{\rm BH}^{-3/2}, \tag{1.27}$$

and given that this ratio reads ~ 100 for a BH of mass $10^6 {\rm M}_\odot$, more massive BHs will have accretion peak luminosities near or below their Eddington luminosity (also considering that the value of the radiation efficiency η depends on the BH spin amplitude and direction).

An alternative mechanism for circularisation is investigated by Ramirez-Ruiz & Rosswog (2009) in considering stars on parabolic orbits tidally disrupted by intermediate-mass BHs (i.e., $M_{\rm BH} = 10^3 {\rm M}_\odot$). After stellar disruption, the debris

bound to the BH orbit onto highly eccentric trajectories with a significant spread in apocentres and a small range of pericentres. Indeed, when returning at pericentre, they are focused into the original orbital plane at about $r_{\rm p}$. This causes shocks to occur near $r_{\rm p}$. These shocks are unlikely to be efficient in directly dissipating energy and circularising the debris, but can somehow change the orbital parameters of the debris exiting pericentre, thus starting up a process similar to general relativistic apsidal precession (Stone 2013). However, it is not clear whether and how this mechanism scales up to stellar tidal disruptions by more massive BHs.

Actually, this "nozzle-driven" circularisation (e.g. Stone 2013) appears in simulations, from Ayal et al. (2000), of disruptive parabolic encounters involving a BH of mass $10^6 \mathrm{M}_\odot$. These authors find that the strong compression and heating of debris when returning at pericentre let about the 75% of them get unbound from the BH, which means that only about the 25% of the debris returning at pericentre after stellar disruption actually gets accreted onto the BH. Yet, the reliability of these results might be limited by the low resolution of the performed simulations.

Despite the process of debris circularisation being complex and still not fully understood, it is reasonable to believe that at some point after tidal disruption it occurs, producing an accretion flow onto the BH. The next section will be focused on the radiation emitted at this stage.

1.4 Multiband emission from tidal disruption events

As previously said, if the debris circularisation goes on quickly and the viscous time in the forming accretion disc is small, the accretion rate of material onto the BH, $\dot{M}_{\rm acc}(t)$, is well defined by Equation 1.20. By assuming that $dM/d\epsilon$ in Equation 1.20 is uniform (Rees 1988; Evans & Kochanek 1989; Phinney 1989),

the accretion luminosity $L(t)$ is assessed through Equation 1.24. For a BH of mass $10^6 - 10^7 \mathrm{M}_\odot$, the accretion peak luminosity $L_{\rm peak}$ comes out to exceed the BH Eddington luminosity $L_{\rm Edd}$ (Equation 1.27), thus implying that a fraction of the accreting debris is probably ejected in an outflowing wind from the accretion disc at early times, up to $t_{\rm Edd}$ (Equation 1.25; Strubbe & Quataert 2009; Lodato & Rossi 2011).

Up to now, it has been talked about the bolometric luminosity, thus considering the emission of radiation at all frequencies. Using Equation 1.21, the bolometric luminosity from the accretion disc, modelled as a multiple black body, scales as

$$L(t) \propto T^4(t) \propto \dot{M}_{\rm acc}(t) \propto t^{-5/3}, \tag{1.28}$$

where $T(t)$ is the effective temperature of the disc at time t. A quick estimate of the effective temperature $T_{\rm peak}$ associated with the accretion peak bolometric luminosity can be obtained from

$$L_{\rm Edd} \sim 4\pi r_{\rm t}^2 \sigma T_{\rm peak}^4 \tag{1.29}$$

(Ulmer 1999), where σ is the Stefan-Boltzmann constant, $L_{\rm peak} \sim L_{\rm Edd}$ and the location of the peak bolometric disc emission is set near $r_{\rm p} \sim r_{\rm t}$ (Equation 1.1). This results in

$$T_{\rm peak} \sim 2.5 \times 10^5 \mathrm{K} \Big(\frac{M_{\rm BH}}{10^6 \mathrm{M}_\odot}\Big)^{1/12} \Big(\frac{1\mathrm{R}_\odot}{R_*}\Big)^{1/2} \Big(\frac{M_*}{1\mathrm{M}_\odot}\Big)^{1/6}, \tag{1.30}$$

meaning that the peak emission from the accretion disc is expected to essentially lie in the UV/soft X-ray band. Over in time, $T(t)$ should decrease following

$$T(t) \propto \dot{M}_{\rm acc}^{1/4}(t) \propto t^{-5/12} \tag{1.31}$$

(Equation 1.28).

However, different conclusions must be drawn when considering the accretion disc emission in specific energy bands (Lodato & Rossi 2011; Lodato 2012). In the

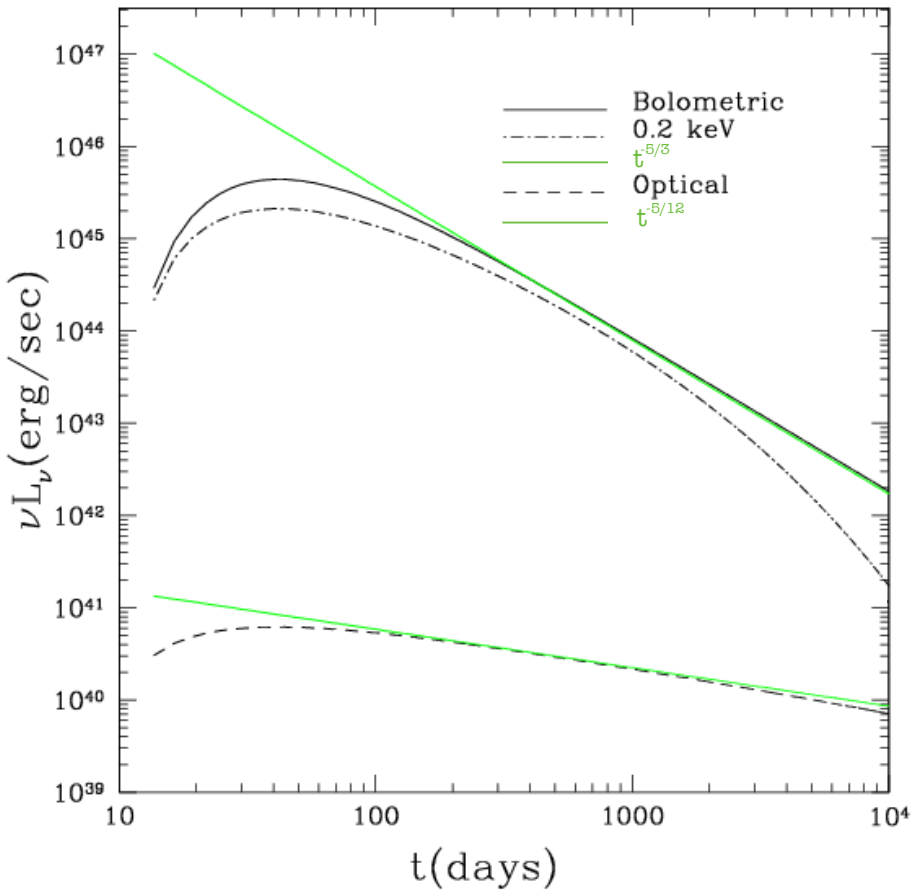

Figure 1.5: Evolution of the accretion bolometric (solid line), soft X-ray (dot-dashed line) and optical (dashed line) luminosities, adapted from Lodato & Rossi 2011. At early times, the soft X-ray curve follows the bolometric curve in decaying as $t^{-5/3}$, while at late times it drops exponentially. At optical wavelengths, instead, the luminosity scales as $\propto t^{-5/12}$ at early times and then steepens a bit.

UV/soft X-ray band, at early times the accretion luminosity follows the accretion bolometric luminosity $L(t) \propto t^{-5/3}$, given that $T(t)$ is associated with the UV/soft X-ray band. At very late times, $T(t)$ significantly decreases and shifts towards optical wavelengths, thus placing the UV/soft X-ray contribution on the Wien tail of the disc emission and making the UV/soft X-ray accretion luminosity decay exponentially. In the optical/UV band, at early times the accretion luminosity scales as $\propto T(t) \propto \dot{M}_{\rm acc}^{1/4}(t) \propto t^{-5/12}$, being the optical/UV contribution on the Rayleigh-Jeans tail of the disc emission. Only at late times it will tend to decay more steeply (Figure 1.5). In the optical/UV band, at early times ($t < t_{\rm Edd}$, Equation 1.25), the accretion disc emission could be overwhelmed by an emission produced by the super-Eddington outflowing wind of accreting material (Strubbe & Quataert 2009; Lodato & Rossi 2011).

Thus, in the absence of the super-Eddington wind one should expect to observe the accretion disc emission, essentially in the UV/soft X-ray band. In the presence of the super-Eddington wind, one could observe its associated emission at optical/UV wavelengths and the accretion disc emission at UV/soft X-ray wavelengths, or, even, at optical/UV energies as reprocessed emission. The reprocessing of the accretion disc emission by the super-Eddington wind could imply a $\propto t^{-5/3}$ decline also for the optical/UV luminosity. Such an outflowing wind would be also responsible for strong UV spectral lines (Strubbe & Quataert 2011).

Another source of reprocessing of the accretion disc emission and production of spectral lines could be the stream of unbound debris produced by stellar disruption (Strubbe & Quataert 2009; Figure 1.3). However, it is not clear whether this stream spatially spreads enough to intercept a significant fraction of the disc emission.

Everything stated in this section holds in the assumption that the debris cir-

cularisation time and the accretion disc viscous time are small, as well as that $dM/d\epsilon$ in Equation 1.20 is uniform. Let's continue to consider $dM/d\epsilon$ uniform. As already said, weaker general relativistic effects imply slower circularisation and accretion onto the BH and farther debris intersections from the BH (Guillochon & Ramirez-Ruiz 2015b). Shiokawa et al. (2015) demonstrate these intersections to quickly occur mainly near

$$a_{\rm min} = \frac{GM_{\rm BH}}{2\Delta\epsilon} \sim \frac{1}{2}\frac{r_{\rm t}^2}{R_*} \sim \frac{r_{\rm t}}{2}\Big(\frac{M_{\rm BH}}{M_*}\Big)^{1/3} \sim 50 r_{\rm t}\Big(\frac{M_{\rm BH}}{10^6{\rm M}_\odot}\Big)^{1/3}\Big(\frac{1{\rm M}_\odot}{M_*}\Big)^{1/3}, \tag{1.32}$$

the semi-major axis of the most bound material, where Equations 1.18 and 1.1 are used. Debris intersections induce shocks, which cause energy dissipation. The peak of the rate of energy dissipation by these shocks (Piran et al. 2015) can be approximately obtained from

$$\dot{E}_{\rm peak} \sim \dot{M}_{\rm peak}\Delta\epsilon \sim 10^{43}\frac{\rm erg}{\rm s}\Big(\frac{10^6{\rm M}_\odot}{M_{\rm BH}}\Big)^{1/6}\Big(\frac{M_*}{1{\rm M}_\odot}\Big)^{8/3}\Big(\frac{1{\rm R}_\odot}{R_*}\Big)^{5/2}, \tag{1.33}$$

with $\Delta\epsilon$ coming from Equation 1.18 and $\dot{M}_{\rm peak}$ obtained from Equation 1.21 evaluated at $t_{\rm peak} \sim 1.5 t_{\rm min}$, with $t_{\rm min}$ explicit. By demonstrating, as Piran et al. (2015), that the dissipated energy is then converted into black body radiation significantly before debris circularisation and accretion, the associated peak bolometric luminosity roughly coincides with $\dot{E}_{\rm peak}$ and the bolometric luminosity, as $\dot{E}(t)$, approximately scales as $\propto \dot{M}(t) \propto t^{-5/3}$. The black body temperature associated with the peak bolometric luminosity reads

$$T_{\rm peak} \sim \Big(\frac{\dot{E}_{\rm peak}}{4\pi a_{\rm min}^2\sigma}\Big)^{1/4} \sim 10^4{\rm K}\Big(\frac{10^6{\rm M}_\odot}{M_{\rm BH}}\Big)^{3/8}\Big(\frac{M_*}{1{\rm M}_\odot}\Big)\Big(\frac{1{\rm R}_\odot}{R_*}\Big)^{9/8}, \tag{1.34}$$

where σ is the Stefan-Boltzmann constant, meaning that the peak emission from the discussed shock energy dissipation essentially lies in the optical band. Optically-selected tidal disruption event candidates (e.g. van Velzen et al. 2011; Gezari et al. 2012; Arcavi et al. 2014), which generally do not show soft X-ray emission, are well explained by this model (Wevers et al. 2017). Indeed, their luminosities peak at $\sim 10^{43} - 10^{44} \mathrm{erg\ s^{-1}}$, their temperatures lie around $10^4 \mathrm{K}$, their black body radii approach a_{min} (Equation 1.32). The fact that their temperatures remain almost constant over time (e.g. Holoien et al. 2014) could be explained by a gradual shift inward of the shock location (Piran et al. 2015).[2] Conversely, soft X-ray-selected tidal disruption event candidates (e.g. Komossa & Bade 1999) seem to be powered by the true accretion onto the BH.

Recently, a new class of tidal disruption event candidates has been discovered (e.g. Bloom et al. 2011; Cenko et al. 2012b; Brown et al. 2015). Their non-thermal hard X-ray emission is hardly explainable with a single radiation mechanism (e.g. Crumley et al. 2016), but is unanimously associated with an accretion-powered relativistic jet. Their radio emission, instead, probably rises from the jet interaction with the circumnuclear medium (e.g. Bower et al. 2013). The detection of new candidates belonging to this, to date, poor class will certainly favour a greater comprehension of their emission.

[2] Thus, in optically-selected tidal disruption event candidates the accretion disc contribution would be highly suppressed. Moreover, spectral features would be produced from where debris are deposited.

Chapter 2

A trip to the zoo of tidal disruptions

This chapter was thought of as an overview of the currently (November, 2017) selected tidal disruption candidates (https://tde.space; Auchettl et al. 2017). To facilitate its reading, I grouped under the name of "the Gold Sample" the most investigated and "traditional" candidates (Table 2.1; Figure 2.1). For each candidate, I report here the associated bibliography and the main features.

THE GOLD SAMPLE OF TIDAL DISRUPTION CANDIDATES

2XMMi J1847 (Lin et al. 2011): This soft X-ray candidate tidal disruption event (RA(J2000)=18:47:25.14, DEC(J2000)=-63:17:25.04) was serendipitously detected in two *XMM-Newton* observations, on September, 2006 and April, 2007, with an absorbed X-ray flux increase by a factor of ~ 9, in the direction of the centre of IC 4765-f01-1504 (RA(J2000)=18:47:25.14, DEC(J2000)=-63:17:24.77, $z = 0.0353$), which is an inactive elliptical galaxy. It was not detected during the RASS and no clear X-ray emission came from both a ROSAT pointed observation on October,

1992 and a *Swift* XRT observation on February, 2011 (the absorbed X-ray flux variability factors of these observations with respect to the second *XMM-Newton* observation are of > 64 and > 12, respectively). Little UV variability was also noticed at the position of the transient. A fit of the two source *XMM-Newton* X-ray spectra with an accretion disc plus power law model gave $kT_{\rm bb} = 65.8 \pm 5.0$ eV and $kT_{\rm bb} = 93.1 \pm 2.2$ eV, respectively. By relating $M_{\rm BH}$ with the bulge luminosity, $M_{\rm BH} = 10^6 - 10^7 {\rm M}_\odot$, based on the allowed range of bulge/total luminosity ratios, while from the normalisation of the accretion disc component in the spectral fits, i.e. from the inner disc radius, $M_{\rm BH} = (0.06 - 3.81) \times 10^6 {\rm M}_\odot$.

3XMM J152130.7+074916 (Lin et al. 2015): This soft X-ray transient (RA(J2000)=15:21:30.75, DEC(J2000)=+07:49:16.70) was serendipitously discovered by *XMM-Newton* on 2000, but not detected in other previous and following high-energy observations, thus defining an X-ray variability factor of $\gtrsim 260$. No clear UV/optical variability was detected at the position of the X-ray flare. It coincided with the centre of a non-active galaxy (3XMM J152130.7+074916: RA(J2000)=15:21:30.73, DEC(J2000)=+07:49:16.52, $z = 0.17901$). A fit of the flare *XMM-Newton* spectrum with a thermal disc model subject to a warm absorber gave $kT_{\rm bb} \sim 0.17$ keV and Lin et al. (2015) attributed the warm absorber to the outflow associated with accretion at a super-Eddington rate in a tidal disruption event. The authors obtained $M_{\rm BH} = (1.9 \pm 0.4) \times 10^5 {\rm M}_\odot$ and $M_{\rm BH} = (1.4 \pm 0.3) \times 10^6 {\rm M}_\odot$ for respectively a non-rotating and a maximally rotating BH from spectral fits and $M_{\rm BH} \sim 2 \times 10^7 {\rm M}_\odot$ and $M_{\rm BH} \lesssim 5 \times 10^7 {\rm M}_\odot$ from different scaling relations.

ASASSN-14ae (Holoien et al. 2014): This optical/UV flare (RA(J2000)=11:08:39.96,

DEC(J2000)=+34:05:52.70) was classified as a tidal disruption event by Holoien et al. (2014). It was discovered on January, 2014 by ASAS-SN (All-Sky Automated Survey for Supernovae), at the centre of the galaxy SDSS J110840.11+340552.2 (RA(J2000)=11:08:40.12, DEC(J2000)=+34:05:52.23, $z = 0.0436$), whose spectrum resembles that of an early-type galaxy with signs of recent star formation and a very weak AGN. During the five months of ASASSN-14ae's follow-up, the outburst spectra showed a blue continuum, which weakened in time, and broad Balmer strong emission lines, together with a broad He II feature appearing at later times, its luminosity declined by ~ 1.5 orders of magnitude, following an exponential decay, its blackbody temperature roughly remained constant at $T_{\rm bb} \sim 20000$ K ($T_{\rm bb} = (22000 \pm 1000)$ K near peak) and no X-ray counterpart was detected. From $M_{\rm BH} - \sigma_*$ and $M_{\rm BH} - M_{\rm bulge}$ relations, $M_{\rm BH} \lesssim 10^{6.8} {\rm M}_\odot$, being σ_* the stellar velocity dispersion in the host galaxy bulge.

ASASSN-14li (Miller et al. 2015; Alexander et al. 2016; Cenko et al. 2016; Holoien et al. 2016a; van Velzen et al. 2016; Brown et al. 2017a): This candidate tidal disruption event (RA(J2000)=12:48:15.23, DEC(J2000)=+17:46:26.22) was discovered by ASAS-SN on November, 2014, at the centre of the post-starburst galaxy SDSS J124815.23+174626.4 (RA(J2000)=12:48:15.23, DEC(J2000)= +17:46:26.44, $z = 0.0206$), which shows evidence of weak AGN activity. Thanks to about six months of follow-up observations, a soft X-ray and an UV counterpart were also detected, thus suggesting the transient to emit at optical, X-ray and UV wavelengths, even though Holoien et al. (2016a) claimed that the X-ray emission probably arose from a different, hotter region with respect to the optical/UV emission or was non-thermal. Indeed, they found that ASASSN-14li significantly

brightened in all these energy bands, but its optical/UV luminosity decayed exponentially and its optical/UV data were fitted with a roughly constant blackbody temperature of $T_{\rm bb} \sim 35000$ K, while its X-ray luminosity, besides requiring a higher blackbody temperature of $T_{\rm bb} \sim 10^5$ K, declined slower and about forty days after discovery prevailed over the optical/UV emission. The source spectrally showed a strong blue continuum, which weakened over time, and broad Balmer and helium emission lines, which weakened and narrowed over time. By relating $M_{\rm BH}$ with the bulge stellar mass, $M_{\rm BH} \sim 10^{6.7}{\rm M}_{\odot}$. However, Miller et al. (2015) estimated the central BH mass using different methods, based on high-resolution X-ray spectra of the transient, which also revealed the likely presence of X-ray gas outflows associated with an initial super-Eddington accretion phase (see also Alexander et al. 2016 and van Velzen et al. 2016 for evidences in the radio band of outflows launched during super-Eddington accretion). From Eddington arguments, $M_{\rm BH} \simeq 2.5 \times 10^6{\rm M}_{\odot}$, by assuming the soft X-ray emission to arise from outside the innermost stable circular orbit of a non-spinning BH, $M_{\rm BH} \lesssim 1.9 \times 10^6{\rm M}_{\odot}$, while by optical, UV and X-ray light curve fitting with the TDE model discussed in Guillochon et al. (2014), $M_{\rm BH} = (0.4 - 1.2) \times 10^6{\rm M}_{\odot}$. Through about six hundred days of follow-up observations, Brown et al. (2017a) detected still a residual emission of the transient relative to its host galaxy at the end of the campaign, in the UV and X-rays. Indeed, after Holoien et al.'s campaign (2016a), the source UV and X-ray luminosities declined shallower, together with the H_{α} luminosity.

ASASSN-15oi (Holoien et al. 2016b): This was the third tidal disruption event (RA(J2000)=20:39:09.10, DEC(J2000)=-30:45:20.71) revealed by ASAS-SN, after ASASSN-14ae and ASASSN-14li. It was discovered on August, 2015, at the centre

of the (at most weakly active) galaxy 2MASX J20390918-3045201 (RA(J2000)= 20:39:09.18, DEC(J2000)=-30:45:20.10, $z = 0.0484$) and thanks to archival and follow-up observations it was classified as an UV/optical tidal disruption event. It significantly brightened over about twenty days in the UV band and in the bluer optical filters and then its optical/UV luminosity faded over about three months, approximately following an exponential decay or a $-5/3$ power law decay in time. Such a fading came out to be much more rapid than other optical/UV tidal disruption events. The transient early spectra showed a strong blue continuum and broad He emission lines, without H emission, while its late-time spectra (about three months after discovery) did not show such features. ASASSN-15oi exhibited also weak soft X-ray emission, which roughly remained constant during the flare. Late-time X-ray observations are needed to see if the X-ray emission fades in time and if it can be associated with the tidal disruption event. A fit of the early optical/UV SED of the source with a single-temperature blackbody gave $T_{\rm bb} = 2 \times 10^4$ K, which increased over about fifty days to $T_{\rm bb} = 4 \times 10^4$ K and then remained roughly constant. A fit of the source combined X-ray spectrum with a blackbody plus power law model ($N_{\rm H} = N_{\rm H_{Gal}} = 5.6 \times 10^{20} {\rm cm}^{-2}$) gave $kT_{\rm bb} = 49^{+10}_{-9}$ eV and $\Gamma = 1.8^{+1.5}_{-0.8}$. By relating $M_{\rm BH}$ with the bulge stellar mass, $M_{\rm BH} = 10^{7.1} {\rm M}_\odot$.

D1-9 (Gezari et al. 2008; Gezari et al. 2009): This UV/optical tidal disruption event was first discovered thanks to GALEX. No X-ray source was detected on 2002 by *XMM-Newton* at the position of its host inactive elliptical galaxy (GALEX J022517.0-043258: RA(J2000)=02:25:17.00, DEC(J2000)=-04:32:59.00, $z = 0.326$) and no FUV or NUV source resulted from GALEX observations on 2003. In the UV band, the flare appeared at the end of 2004 ($\Delta m \gtrsim 2$ mag) and

then decayed by ~ 1 mag over three years. At the same time, it was detected in the optical band, too. A very weak soft X-ray emission at the same position was detected by *Chandra* on 2006. A two-temperature blackbody fit of the SED from optical to X-rays of the flare near peak (2004 + *Chandra* detection on 2006) gave $T_{\rm bb_1} = (5.5 \pm 1.0) \times 10^4$ K and $T_{\rm bb_2} = (2.7 \pm 0.2) \times 10^5$ K, even though the contribution of $T_{\rm bb_2}$ at the peak of the flare is not clear due to the lack of X-rays observations at the time of UV/optical peak. From the fit of the SED, by requiring that the radius of the soft X-ray emission is greater than the radius of the innermost stable circular orbit, $M_{\rm BH} < 4 \times 10^7 {\rm M}_\odot$, while from the flare start time and the time of disruption, as estimated by Gezari et al. (2008), $M_{\rm BH} > 8.2 \times 10^6 {\rm M}_\odot$. The values of $M_{\rm BH} = 1^{+2}_{-0.7} \times 10^8 {\rm M}_\odot$, estimated by relating $M_{\rm BH}$ with the bulge luminosity, and $M_{\rm BH} = 2.4 \times 10^7 {\rm M}_\odot$, arising from an analytical solution from Lodato et al. (2009), are compatible with this range of masses.

D23H-1 (Gezari et al. 2009): This large-amplitude UV/optical flare was discovered thanks to GALEX observations ranging from 2004 to 2008. The source UV flux was roughly constant up to 2006, then it increased by a factor of 4.7 ± 1.2 in the NUV and 9.0 ± 1.5 in the FUV over a year. Palomar Large Field Camera imaging at the time of UV peak confirmed the flare to be detectable also to optical wavelengths. *Chandra* observations near the UV peak did not display any X-ray counterpart. This source coincides with the nucleus of a star-forming galaxy (SDSS J233159.53+001714.5: RA(J2000)=23:31:59.54, DEC(J2000)=+00:17:14.58, $z = 0.1855$), which could host a low-luminosity AGN at its centre. Its UV/optical SED during the peak, corrected for internal extinction, was modelled with a single-temperature blackbody, giving $T_{\rm bb} = 1.7^{+2.2}_{-0.2} \times 10^5$ K, while non-correction for internal extinction

gave $T_{\rm bb} = 4.9 \times 10^4$ K. The flare properties deviate from the average properties of AGNs, while resemble that of an UV/optical tidal disruption event. By assuming a solar-type star disrupted at $r_{\rm p} = r_{\rm t}$, the central BH mass was estimated to be $M_{\rm BH} = (0.3 - 30) \times 10^6 k^3 {\rm M}_\odot$ from fitting a power law decay to the source FUV light curve (k depends on the spin up of the star when disrupted), $M_{\rm BH} = (5.4 \pm 0.4) \times 10^7 {\rm M}_\odot$ from an analytical solution from Lodato et al. (2009), $M_{\rm BH} < 6.26 \times 10^6 {\rm M}_\odot$ from relating $M_{\rm BH}$ with the bulge stellar mass, $\log(M_{\rm BH}/{\rm M}_\odot) = 7 \pm 1$ from relating $M_{\rm BH}$ with σ_*.

D3-13 (Gezari et al. 2006; Gezari et al. 2008; Gezari et al. 2009): This UV/optical outburst was first discovered thanks to GALEX. It was not detected in the NUV and FUV on 2003, it appeared in observations taken nine and twelves months later ($\Delta m \gtrsim 2$ mag) and then it decayed by 2 mag over two years, well following the $-5/3$ power law decay in time typical of tidal disruption events. *Chandra* archival observations on April 2005 showed an extremely soft X-ray counterpart, while *Chandra* observations on September 2005 did not show any source. No variable optical source appeared at the position of the UV flare from January to June 2005, but on 2004 an optically variable object was detected. The outburst arose from an inactive elliptical galaxy (GALEX J141929.8+525206: RA(J2000)=14:19:29.81, DEC(J2000)=+52:52:06.37, $z = 0.3698$). A blackbody fit of the SED from optical to X-rays of the flare on April 2005 gave 1×10^5 K $< T_{\rm bb} < 4.9 \times 10^5$ K, while a two-temperature blackbody fit of the SED from optical to X-rays of the flare near peak (2004 + *Chandra* detections on April 2005) gave $T_{\rm bb_1} = (1.0 \pm 0.1) \times 10^4$ K and 1.2×10^5 K $< T_{\rm bb_2} < (4.9 \pm 0.2) \times 10^5$ K. From the fit of the SED near peak, by requiring that the radius of the soft X-ray emission is greater than the

radius of the innermost stable circular orbit, $M_{\rm BH} < 8.7 \times 10^7 {\rm M}_\odot$, while from the flare start time and the time of disruption, as estimated in Gezari et al. (2008), $M_{\rm BH} > 2.4 \times 10^6 {\rm M}_\odot$. The values of $M_{\rm BH} = 2^{+2}_{-1} \times 10^7 {\rm M}_\odot$, estimated by relating $M_{\rm BH}$ with σ_*, and $M_{\rm BH} = 1.2 \times 10^7 {\rm M}_\odot$, arising from an analytical solution from Lodato et al. (2009), are fully within this range of masses. Gezari et al. (2009) re-estimated the blackbody temperature from the UV/optical SED at peak (by extrapolating fluxes from the source light curves) and found $T_{\rm bb} = (4.9 \pm 0.2) \times 10^4$ K.

IC3599 (Brandt et al. 1995; Grupe et al. 1995; Vaughan et al. 2004; Sani et al. 2010; Bower et al. 2013; Campana et al. 2015; Grupe et al. 2015): Brandt et al. (1995), Grupe et al. (1995) and Vaughan et al. (2004), based on ROSAT and *Chandra* observations, classified this source as an X-ray tidal disruption event, even if arising from the nucleus of a Seyfert 1.5-1.9 galaxy (RA(J2000)=12:37:41.18, DEC(J2000)=+26:42:27.24, $z = 0.021245$). Indeed, it appeared very bright during the RASS in the soft X-rays ($kT_{\rm bb} = 83^{+4}_{-12}$ eV when fitting the source spectrum with an accretion disc plus power law model) and then rapidly weakened by a factor of ~ 100, showing also a somehow spectral hardening. Campana et al. (2015), based on *Swift* following data (2010-2014), later discovered another soft X-ray flare, similar to the first one, at the same position, which also showed transient optical and UV counterparts. They found the total ROSAT, *Chandra* and *Swift* X-ray light curve to be well fitted by a series of three (rather than two) $-5/3$ equal power laws, with periodicity of ~ 9.5 years, and the temperature evolution of the transient X-ray spectra when fitted with an accretion disc plus power law model resembled that of the accretion disc theory if such a number of flares was considered. They classified IC3599 as a multiple tidal disruption event, consisting on the periodic

partial disruption of a star on a highly eccentric orbit around the central BH, which could also be responsible of the AGN low-luminosity emission, while Grupe et al. (2015) associated this recurrent emission to accretion disc instability. From $M_{\rm BH} - L_{K_{\rm bulge}}$ and $M_{\rm BH} - \sigma_*$ relations, the central BH mass was estimated to be in the range $(2 - 12) \times 10^6 {\rm M}_\odot$. A delayed radio emission from the X-ray source position was also detected and suggested to be produced from the core of a jet.

iPTF16axa (Hung et al. 2017): This candidate tidal disruption event (RA(J2000)= 17:03:34.36, DEC(J2000)=+30:35:36.8) was discovered on May, 2016 by the intermediate Palomar Transient Factory (iPTF), at the centre of the early-type galaxy SDSS J170334.34+303536.6. It showed no significant X-ray emission but a bright UV counterpart and both its optical and UV light curves decayed over time following approximately a $-5/3$ power law. Its optical spectra displayed broad He II and H_α emission lines at $z = 0.108$, which weakened over time. A fit of the transient UV/optical SED at the time of discovery with a blackbody model gave $T_{\rm bb} = (2.85 \pm 0.37) \times 10^4$ K, while the upper limit on the source X-ray emission imposed $T_{\rm bb} < 1.85 \times 10^5$ K. Such a blackbody temperature roughly remained constant during the transient monitoring ($T_{\rm bb} \sim 3 \times 10^4$ K). By relating $M_{\rm BH}$ with σ_*, $M_{\rm BH} = 5.0^{+7.0}_{-2.9} \times 10^6 {\rm M}_\odot$.

iPTF16fnl (Blagorodnova et al. 2017; Brown et al. 2017b): This optical/UV flare (RA(J2000)=00:29:57.04, DEC(J2000)=+32:53:37.50) was discovered on August, 2016 thanks to the iPTF, at the centre of the E+A galaxy Mrk950 (RA(J2000)= 00:29:57.01, DEC(J2000)=+32:53:37.24, $z = 0.0163$), which spectrally shows no strong emission lines that are signs of ongoing or recent star formation, Balmer

absorption features and an early-type galaxy population. Its optical/UV luminosity peaked an order of magnitude below that of other optical/UV tidal disruption events and decayed exponentially on a time scale of only about sixty days. In the X-ray band, no significant emission was revealed at the position of the optical/UV flare, during and after it. iPTF16fnl early spectra showed broad He and H emission lines, but then most of them narrowed and faded. A fit of the source optical/UV SEDs at different times with a single-temperature blackbody model gave an average temperature of $T_{\rm bb} = 3 - 4 \times 10^4$ K. From Blagorodnova et al. (2017), by relating $M_{\rm BH}$ with the bulge stellar mass, $M_{\rm BH} \lesssim 10^{6.6\pm0.4}{\rm M}_\odot$, while by relating $M_{\rm BH}$ with σ_*, $M_{\rm BH} = 10^{6.33\pm0.38}{\rm M}_\odot$, fully in agreement with the previous estimate. Brown et al. (2017b), instead, estimated $M_{\rm BH} \lesssim 5.5 \times 10^6{\rm M}_\odot$ by relating $M_{\rm BH}$ with the bulge stellar mass.

LEDA 095953 (Cappelluti et al. 2009): This X-ray source (RA(J2000)=13:47:30.33, DEC(J2000)=-32:54:50.63) was serendipitously detected in a ROSAT-PSPC pointed observation of the galaxy cluster A3571 on 1992. It arose from the centre of the cluster member LEDA 095953 (RA(J2000)=13:47:30.10, DEC(J2000)= -32:54:52.00, $z = 0.0366$), which is a S0 galaxy without significant evidence of an AGN. Following ROSAT, *XMM-Newton* and *Chandra* observations revealed a flux decay of a factor > 650 over about thirteen years, which is consistent with the $-5/3$ power law trend typical of tidal disruption events. A fit of the ROSAT-PSPC spectrum of the source with a blackbody model gave $kT_{\rm bb} = 120 \pm 16$ eV. By relating $M_{\rm BH}$ with the K bulge luminosity, $M_{\rm BH} \sim 10^7{\rm M}_\odot$.

NGC 3599 (Esquej et al. 2007; Esquej et al. 2008; Esquej et al. 2012; Sax-

ton et al. 2015): This X-ray variable object was discovered in an *XMM-Newton* slew on 2003, with a soft X-ray flux 88 times higher than the source RASS upper limit and 150 times higher than a ROSAT pointed observation on 1993. Follow-up X-ray observations of the transient revealed an emission which roughly shaped the $-5/3$ power law decay in time typical of tidal disruption events but archival *XMM-Newton* observations showed it to be bright already 18 months before the estimated emission peak, thus suggesting the flare not to be produced by a classical, fast-rising and short-peak tidal disruption event, but possibly by a delayed tidal disruption event (due to late and distant circularisation) or by the stripping of a giant star envelope. The source coincided with the centre of its host galaxy, NGC 3599 (RA(J2000)=11:15:26.95, DEC(J2000)=+18:06:37.33, $z = 0.002699$), which was classified as a LINER/ low-luminosity Seyfert galaxy, based on optical spectroscopy. By fitting the transient *XMM-Newton* slew spectrum (2003) with a blackbody model ($N_{\rm H_{Gal}} = 1.42 \times 10^{20} {\rm cm}^{-2}$), Esquej et al. (2008) obtained $kT_{\rm bb} = 95^{+4}_{-3}$ eV. From $M_{\rm BH} - \sigma_*$ different relations, $M_{\rm BH} = (0.7 - 4.1) \times 10^6 {\rm M}_\odot$, by relating $M_{\rm BH}$ with the V magnitude of the host, $M_{\rm BH} = (3.5 \pm 0.9) \times 10^7 {\rm M}_\odot$, while by relating $M_{\rm BH}$ with the K bulge luminosity of the host, $M_{\rm BH} = (3.1 \pm 1.5) \times 10^7 {\rm M}_\odot$, thus giving $M_{\rm BH} = (0.7 - 46) \times 10^6 {\rm M}_\odot$.

NGC 5905 (Bade et al. 1996; Komossa & Bade 1999; Li et al. 2002; Gezari et al 2003; Gezari et al. 2004; Halpern et al. 2004): This extremely soft X-ray nuclear transient was discovered on July, 1990 during the RASS, and then re-observed on December, 1990 and January, 1991, again during the RASS, and on January, 1992 and July, 1993 via pointed ROSAT observations, showing a decay factor of ~ 80. HRI data on 1996 revealed a further decline of the source by a factor of

~ 2 and contributed to the roughly $-5/3$ power law decay in time of its X-ray light curve. Halpern et al. (2004) analysed *Chandra* data obtained on 2002 and interpreted the diffuse X-ray emission arising from the transient position to come from the starburst nature of its host barred spiral galaxy (RA(J2000)=15:15:23.32, DEC(J2000)=+55:31:01.59, $z = 0.01124$). No optical variability was detected during the X-ray outburst. A fit with a blackbody model of the transient RASS spectrum at the time of discovery ($N_{\rm H} = N_{\rm H_{Gal}} = 1.5 \times 10^{20} {\rm cm}^{-2}$) gave $kT_{\rm bb} = 56 \pm 12$ eV. The X-ray flare was suggested to be produced by the tidal disruption of a star by the central BH of its host galaxy, although Gezari et al. (2003, 2004) obtained follow-up Hubble Space Telescope (HST) optical spectra of the host galaxy and detected a low nuclear Seyfert 2 activity, which was previously probably masked by HII regions. By assuming the observed X-ray luminosity at the time of discovery to coincide with the Eddington luminosity, $M_{\rm BH} = 10^4 - 10^5 {\rm M}_\odot$. However, by relating $M_{\rm BH}$ with the bulge luminosity, $M_{\rm BH} = 10^7 - 10^8 {\rm M}_\odot$, thus implying the flare to be highly sub-Eddington. In order to explain such a low luminosity, Li et al. (2002) suggested that the X-ray flare was produced by the partial stripping of the envelope of a low-mass main sequence star, by the tidal disruption of a brown dwarf or by the tidal disruption of a giant planet.

PS1-10jh (Gezari et al. 2012; Gaskell & Rojas Lobos 2014; Guillochon et al. 2014; Strubbe & Murray 2015): This transient (RA(J2000)=16:09:28.29, DEC(J2000)=+53:40:23.52) was first discovered in the optical band on 2010 by the Pan-STARRS1 survey and then, independently, in the NUV by GALEX, with a NUV variability greater than a factor of 6.4 mag. No X-ray emission from *Chandra* data was detected at the position of the transient during the UV/optical flare. The

source coincided with the centre of an inactive galaxy (SDSS J160928.27+534023.9: RA(J2000)=16:09:28.28, DEC(J2000)=+53:40:23.99, $z = 0.1696$) and its optical/UV spectra showed broad high-ionization He II emission lines, which faded in time together with the UV/optical flare decline, and missed hydrogen lines, suggesting the event to be an optical/UV tidal disruption event involving a He-rich red giant that lost its hydrogen envelope (Gezari et al. 2012). Strubbe & Murray (2015) pointed out a BH mass of $M_{\rm BH} \lesssim 2 \times 10^5 {\rm M}_\odot$ in order to tidally disrupt such a dense He-rich core. Guillochon et al. (2014), however, based on hydrodynamical simulations, supported the idea that the disrupted object was a main-sequence star and explained the presence of He lines and the absence of H lines for this tidal disruption candidate as their production depends on the spatial extent in time of the accretion disc, meaning that H lines should be produced when the accretion disc reaches the needed distance. This interpretation was also supported by Gaskell & Rojas-Lobos (2014). The optical/UV pre-peak and late-time SEDs of the flare, corrected for the maximum internal extinction, were both modelled with a single-temperature blackbody of $T_{\rm bb} = (5.5 \pm 0.4) \times 10^4$ K, while no corrections for internal extinction gave $T_{\rm bb} = (2.9 \pm 0.2) \times 10^4$ K. By relating $M_{\rm BH}$ with the bulge stellar mass, the central BH mass was estimated to be $M_{\rm BH} = 4^{+4}_{-2} \times 10^6 {\rm M}_\odot$, while from fitting the UV/optical light curve of the flare with an appropriately adjusted model by Lodato et al. (2009), which considers a 5/3 polytropic star of mass M_* and radius R_* disrupted at $r_{\rm p} = r_{\rm t}$, $M_{\rm BH} = (1.9 \pm 0.1) \times 10^6 M_*^2 R_*^{-3} {\rm M}_\odot$ (Gezari et al. 2012).

PS1-11af (Chornock et al. 2014): This optical/UV candidate tidal disruption event (RA(J2000)=09:57:26.82, DEC(J2000)=+03:14:01.00) was discovered by

the Pan-STARRS1 survey on December 30, 2010. It reached a peak at the end of January, 2011 ($\Delta m \sim 2$ mag) and then faded, remaining detectable in the Pan-STARRS1 survey also at the end of April, 2011, when observations stopped ($\Delta m \lesssim 2$ mag). GALEX NUV observations immediately after the peak revealed the transient, while prior GALEX NUV and FUV observations did not reveal any source. The object appeared to maintain a roughly constant blue colour. It arose from the centre of SDSS J095726.82+031400.9 (RA(J2000)=09:57:26.82, DEC(J2000)=+03:14:00.94, $z = 0.4046$), which is an early-type galaxy without evidence for star formation or AGN activity, and its otherwise featureless spectra revealed transient broad absorption features at UV wavelengths. A fit of the optical/UV SED of the source with a single-temperature blackbody model gave $T_{\rm bb} = 19080 \pm 750$ K, but a more complex model could be required, internal extinction might have to be considered and no X-ray observations were available to check for high energy emission. Chornock et al. (2014) classified the event as a partial tidal disruption event, due to their estimated low accreted mass. However, if most of the radiation would be emitted at X-ray wavelengths, the accreted mass could be greater. From different scaling relations, $M_{\rm BH} = (8 \pm 2) \times 10^6 {\rm M}_\odot$ and $M_{\rm BH} < (1.6 \pm 0.4) \times 10^7 {\rm M}_\odot$.

PTF-09axc (Arcavi et al. 2014): This is one of the six tidal disruption candidates which came out from the Palomar Transient Factory (PTF) analysis by Arcavi et al. (2014) (RA(J2000)=14:53:13.06, DEC(J2000)=+22:14:32.20). Discovered on 2009, it showed broad hydrogen features in its optical spectra and it almost coincided with the centre of its host galaxy (SDSS J145313.07+221432.2: RA(J2000)=14:53:13.08, DEC(J2000)=+22:14:32.27, $z = 0.1146$), which displays

a spectrum similar to E+A galaxies. There is evidence of the possible presence of a very weak AGN in the host galaxy (very weak [OIII]$\lambda 5007$ emission and low X-ray emission from the position of the source five years after the flare peak). By fitting an event optical spectrum near peak with a blackbody model, $T_{\rm bb} \gtrsim 12000$ K, while by relating $M_{\rm BH}$ with the bulge stellar mass, $M_{\rm BH} = 2.69^{+0.66}_{-0.64} \times 10^6 {\rm M}_\odot$.

PTF-09djl (Arcavi et al. 2014): This is another tidal disruption candidate resulting from the PTF analysis by Arcavi et al. (2014) (RA(J2000)=16:33:55.94, DEC(J2000)=+30:14:16.30). Similarly to PTF-09axc, it was discovered on 2009, it showed broad hydrogen features in its optical spectra and it almost coincided with the centre of its host galaxy (SDSS J163355.97+301416.6: RA(J2000)=16:33:55.97, DEC(J2000)=+30:14:16.65, $z = 0.184$), which spectrally resembles an E+A galaxy. Unlike PTF-09axc, there is no evidence of AGN activity. By fitting an event optical spectrum near peak with a blackbody model, $T_{\rm bb} \gtrsim 26000$ K, while by relating $M_{\rm BH}$ with the bulge stellar mass, $M_{\rm BH} = 3.57^{+9.97}_{-2.96} \times 10^6 {\rm M}_\odot$.

PTF-09ge (Arcavi et al. 2014): This is another tidal disruption candidate which came out from the PTF analysis by Arcavi et al. (2014) (RA(J2000)=14:57:03.10, DEC(J2000)=+49:36:40.80). Discovered on 2009, it was spectroscopically He-rich and it almost coincided with the centre of its host galaxy (SDSS J145703.17+493640.9: RA(J2000)=14:57:03.18, DEC(J2000)=+49:36:40.97, $z = 0.064$), which spectrally resembles a very low star-forming galaxy without evidence of AGN activity. By fitting an event optical spectrum near peak with a blackbody model, $T_{\rm bb} \gtrsim 22000$ K, while by relating $M_{\rm BH}$ with the bulge stellar mass, $M_{\rm BH} = 5.65^{+3.02}_{-0.98} \times 10^6 {\rm M}_\odot$.

RBS 1032 (Ghosh et al. 2006; Maksym et al. 2014a): This luminous, soft X-ray flare arising from the non-active dwarf galaxy SDSS J114726.69+494257.8 (RA(J2000)=11:47:26.80, DEC(J2000)=+49:42:59.00, $z = 0.026$) was discovered by Ghosh et al. (2006) thanks to RASS and two- and four-years later ROSAT pointed observations. Follow-up *XMM-Newton* observations (2009) analysed by Maksym et al. (2014a) revealed a very faint soft X-ray emission (lower by a factor of ~ 200 with respect to ROSAT data) from within the $30''$ error radius of the source ROSAT position. The transient spectra associated with the ROSAT pointed observations were fitted with accretion disc models, thus respectively giving $kT_{\rm bb} = 72.5^{+30.4}_{-18.1}$ eV and $kT_{\rm bb} = 64.9^{+12.2}_{-11.2}$ eV and $M_{\rm BH} \sim 5 \times 10^4 {\rm M}_{\odot}$, in agreement with $\log(M_{\rm BH}/M_{\odot}) \lesssim 6.4$, estimated by relating $M_{\rm BH}$ with the bulge luminosity. Also the transient *XMM-Newton* spectrum was fitted with an accretion disc model ($N_{\rm H} = N_{\rm H_{Gal}} = 1.98 \times 10^{20} {\rm cm}^{-2}$), giving $kT_{\rm bb} = 150 \pm 20$ eV. Maksym et al. (2014a) identified the event as an X-ray tidal disruption event, while Ghosh et al. (2006) suggested that the observed flare could be produced by a binary involving an intermediate-mass BH. The transient host galaxy has an optically bright nucleus, thanks to its nuclear supermassive globular clusters, of which one may host the intermediate-mass BH system.

RX J1242-11A (Komossa & Greiner 1999; Gezari et al. 2003; 2004; Halpern et al. 2004; Komossa et al. 2004): This candidate tidal disruption event (RA(J2000)= 12:42:38.55, DEC(J2000)=-11:19:20.80) was observed between December, 1990 and January, 1991, during the RASS, and serendipitously re-observed on 1992 in a pointed ROSAT observation, displaying a rise in brightness by a factor of > 20. It was associated with the inactive galaxy RX J1242.6-1119A (RA(J2000)=12:42:36.90,

DEC(J2000)=-11:19:35.00, $z = 0.05$) thanks to *Chandra* observations, even though a second weaker inactive galaxy was detected in optical observations within the source ROSAT error circle. *Chandra* and *XMM-Newton* follow-up observations on 2001 showed a decline in its X-ray emission by a factor of ~ 200 and a spectral hardening. A fit with a blackbody model ($N_{\rm H} = N_{\rm H_{Gal}} = 3.74 \times 10^{20} {\rm cm}^{-2}$) of the transient soft X-ray spectrum at the time of putative peak gave $kT_{\rm bb} = 0.06 \pm 0.01$ keV. By assuming that the observed X-ray luminosity at putative peak roughly coincided with the Eddington luminosity, $M_{\rm BH} \sim 7 \times 10^5 {\rm M}_\odot$, while by relating $M_{\rm BH}$ with the bulge luminosity, $M_{\rm BH} \sim 2 \times 10^8 {\rm M}_\odot$.

RX J1420+53 (Greiner et al. 2000): This soft X-ray transient (RA(J2000)= 14:20:24.20, DEC(J2000)=+53:34:11.00) was discovered thanks to the high flux variation ($\gtrsim 150$) displayed between a RASS observation and a six-month previous ROSAT pointed observation in 1990. Optical observations revealed two inactive galaxies within the X-ray source position error circle, but source "A" (RX J1420.4+5334: RA(J2000)=14:20:24.37, DEC(J2000)=+53:34:11.72, $z = 0.147$) is likely to be the transient host. Greiner et al. (2000) tentatively classified this transient as an X-ray tidal disruption event. A fit of the source RASS spectrum with a single-temperature blackbody model ($N_{\rm H} = N_{\rm H_{Gal}} = 1.2 \times 10^{20} {\rm cm}^{-2}$) gave $kT_{\rm bb} = 38 \pm 10$ eV, while a fit with an accretion disc model ($N_{\rm H} = N_{\rm H_{Gal}}$) gave $M_{\rm BH} = 7 \times 10^5 {\rm M}_\odot$.

RX J1624+75 (Grupe et al. 1999; Gezari et al. 2003; 2004; Halpern et al. 2004): This X-ray tidal disruption candidate (RA(J2000)=16:24:56.70, DEC(J2000)= +75:54:57.50) was detected bright on 1990, during the RASS, and turned off in two

following pointed observations on 1992. Based on *Chandra* follow-up observations on 2002, Halpern et al. (2004) estimated the decay factor to be ~ 6000. The flare arose from the inactive spiral galaxy RX J1624.9+7554 (RA(J2000)=16:24:56.66, DEC(J2000)=+75:54:56.09, $z = 0.0636$). A fit of the transient RASS spectrum with a blackbody plus power law model ($N_{\rm H} = N_{\rm H_{Gal}} = 3.9 \times 10^{20}{\rm cm}^{-2}$) gave $kT_{\rm bb} = 107 \pm 58$ eV. By assuming that the observed RASS X-ray luminosity coincided with the Eddington luminosity, $M_{\rm BH} \sim 10^6 {\rm M}_\odot$.

SDSS J1311 (Maksym et al. 2010; Bower et al. 2013): This soft X-ray flare (RA(J2000)=13:11:22.18, DEC(J2000)=-01:23:45.20) arose from the centre of a member of the galaxy cluster A1689 (SDSS J131122.15-012345.6: RA(J2000)= 13:11:22.15, DEC(J2000)=-01:23:45.61, $z = 0.18$) and was discovered on 2004 on the occasion of a monitoring of galaxy clusters for flares, based on six epochs (2000-2007) of *Chandra* and one epoch (2001) of *XMM-Newton* archival observations. Its luminosity rose by a factor of ~ 30 over about two years and decayed by a factor of ~ 9 over about two years, approximately following a $-5/3$ power law decay in time, and a fit of its X-ray spectrum at peak with a blackbody model ($N_{\rm H} = N_{\rm H_{Gal}} = 1.82 \times 10^{20}{\rm cm}^{-2}$) gave $kT_{\rm bb} = 0.12 \pm 0.02$ keV. A fit with the same model of a *Chandra* X-ray spectrum of the flare after the decay (2006) gave $kT_{\rm bb} = 0.10 \pm 0.02$ keV. The event host galaxy is likely to be a spiral which does not show strong optical emission lines that would indicate the presence of an AGN. From $M_{\rm BH} - L_{\rm bulge}$ relations, $\log(M_{\rm BH}/M_\odot) = 6.46 \pm 0.38$. Maksym et al. (2010) suggested the outburst to be associated with an X-ray tidal disruption event. Late-time radio observations of the source were discussed by Bower et al. (2013), who did not find any radio counterpart, which would be indicative of the formation

of a jet.

TDE1 (van Velzen et al. 2011): This tidal disruption candidate was discovered in the context of a systematic search for tidal disruption events based on archival SDSS data, with the requirement of arising from the nuclei of non-active galaxies. Indeed, it turned on at the centre of the inactive E/S0 galaxy SDSS J234201.40+010629.2 (RA(J2000)=23:42:01.41, DEC(J2000)=+01:06:29.30, $z = 0.136$). Its optical/UV light curve was obtained thanks to the SDSS data and also to GALEX archival data taken about eight hundred days after its first SDSS observation. A fit of the optical SED of the flare (2006) with a blackbody model gave $T_{\rm bb} = 2.4^{+0.3}_{-0.2} \times 10^4$ K. By relating $M_{\rm BH}$ with the bulge luminosity, $M_{\rm BH} = (6 - 20) \times 10^{6\pm0.3}{\rm M}_{\odot}$; the uncertainty on the coefficient reflects the uncertainty in the $L_{\rm bulge}$ estimate, while the uncertainty on the exponent reflects the scatter in the $M_{\rm BH} - L_{\rm bulge}$ relation.

TDE2 (van Velzen et al. 2011): As in the case of TDE1, this transient was discovered during a systematic search for tidal disruption candidates based on archival SDSS data, with the requirement of arising from the nuclei of non-active galaxies. It turned on at the centre of the inactive star-forming E/S0 galaxy SDSS J232348.61-010810.3 (RA(J2000)=23:23:48.62, DEC(J2000)=-01:08:10.34, $z = 0.2515$). Its optical/UV light curve was obtained thanks to the SDSS data together with pre-flare and post-flare GALEX and CRTS archival observations, and CRTS data revealed that the flare was even brighter by approximately one magnitude about ninety five days before its first SDSS observation. A fit of the optical SED of the flare (2007) with a blackbody model gave $T_{\rm bb} = 1.82^{+0.07}_{-0.06} \times 10^4$ K. By relating $M_{\rm BH}$ with the bulge luminosity, $M_{\rm BH} = (2 - 10) \times 10^{7\pm0.3}{\rm M}_{\odot}$; the uncertainty on the coefficient

reflects the uncertainty in the $L_{\rm bulge}$ estimate, while the uncertainty on the exponent reflects the scatter in the $M_{\rm BH} - L_{\rm bulge}$ relation.

WINGS (A1795) (Maksym et al. 2013; Donato et al. 2014; Maksym et al. 2014b): The galaxy cluster Abell 1795 ($z = 0.062$) was observed by *Chandra* on different epochs, between December, 1999 and June, 2011, and once by *XMM-Newton*, on June, 2000. At the *Chandra* X-ray position of RA(J2000)=13:48:49.86, DEC(J2000)=+26:35:57.49, an highly variable (by a factor of ~ 50) long (> 5 yr) soft X-ray flare was identified, within 1 arcmin of Abell 1795 centre, possibly associated with a tidal disruption event. Multiwavelength observations revealed as possible host the galaxy WINGS J134849.88+263557.5 (RA(J2000)=13:48:49.88, DEC(J2000)=+26:35:57.50), which should be an early-type non-active (or very weakly active) compact dwarf galaxy hosting an intermediate-mass BH, if it is a member of Abell 1795, as likely (Maksym et al. 2014b). The galaxy is unusually faint, probably due to previous tidal stripping in the cluster core. A fit of the transient *Chandra* X-ray spectrum at the epoch of putative peak (December, 1999) with a blackbody model gave $kT_{\rm bb} = 0.084 \pm 0.003$ keV, while a fit with an accretion disc model gave $kT_{\rm bb} = 0.103 \pm 0.007$ keV and $M_{\rm BH} = 1.06^{+0.24}_{-0.31} \times 10^5 (R_{\rm S}/R_{\rm ISCO})(\cos i)^{-1/2} {\rm M}_\odot$, being $R_{\rm S}$, $R_{\rm ISCO}$ and i the Schwarzschild radius, the radius of the innermost stable circular orbit and the disc inclination, respectively. From different $M_{\rm BH} - L_{\rm bulge}$ and $M_{\rm BH} - M_{\rm bulge}$ relations, $\log(M_{\rm BH}/{\rm M}_\odot) \sim 5.4$, $\log(M_{\rm BH}/{\rm M}_\odot) \sim 4.9$, $\log(M_{\rm BH}/{\rm M}_\odot) \sim 5.1 - 5.7$, by relating $M_{\rm BH}$ with σ_*, $M_{\rm BH} \sim 7 \times 10^5 {\rm M}_\odot$, while by assuming that the observed X-ray luminosity at the putative peak coincided with the Eddington luminosity, $M_{\rm BH} \sim 1.3 \times 10^4 {\rm M}_\odot$. Similar estimates of $M_{\rm BH}$ are reported in Donato et al.

(2014). Archival extreme UV observations taken between January, 1997 and July, 2000 suggested a strong correlation between the discussed X-ray flare and an EUV bright transient. By assuming that the soft X-ray luminosity inferred from the peak of the EUV outburst coincided with the Eddington luminosity, $M_{\rm BH} \sim 1.5{\times}10^5 {\rm M}_\odot$.

XMMSL1J0630-60 (Kann et al. 2011; Read et al. 2011a; Read et al. 2011b; Mainetti et al. 2016a): see chapter 3.

OTHER CURRENTLY SELECTED TIDAL DISRUPTION CANDIDATES

2MASX J0203 (Esquej et al. 2007; Strotjohann et al. 2016): Esquej et al. (2007) suggested it to be a candidate X-ray tidal disruption event, based on its discovery in an *XMM-Newton* slew on 2004 with a soft X-ray flux 63 times higher than its RASS (ROSAT All-Sky Survey) upper limit. However, its host galaxy (2MASX J02030314-0741514: RA(J2000)=02:03:03.14, DEC(J2000)=-07:41:51.41, $z = 0.0615$) was classified as a Seyfert 1 and, thanks to follow-up observations, Strotjohann et al. (2016) considered also AGN variability as the cause of the event.

2MASX J0249 (Esquej et al. 2007; Strotjohann et al. 2016): Again, Esquej et al. (2007) suggested it to be a candidate X-ray tidal disruption event, based on its discovery in an *XMM-Newton* slew on 2004 with a soft X-ray flux 21 times higher than its RASS upper limit. Its host (2MASX J02491731-0412521: RA(J2000)=02:49:17.32, DEC(J2000)=-04:12:52.20, $z = 0.0186$) was classified as a Seyfert 1.9 galaxy and, thanks to follow-up observations, Strotjohann et al. (2016) pointed out how the source X-ray light curve and thermal soft spectra resembled

that of typical tidal disruptions, even though AGN variability can not be ruled out.

ASASSN-15lh (Dong et al. 2016b; Leloudas et al. 2016; Godoy-Rivera et al. 2017; Margutti et al. 2017): This optical/UV ultra-luminous transient (RA(J2000)= 22:02:15.45, DEC(J2000)=-61:39:34.64) was discovered by ASAS-SN on June, 2015, at the centre of the galaxy APMUKS (BJ) B215839.70-615403.9 (RA(J2000)= 22:02:15.39, DEC(J2000)=-61:39:34.60, $z = 0.2326$). At early times it showed features which resembled those of super-luminous supernovae (SLSNe), even though its luminosity was even higher than that of any other known SLSN and its host is a luminous galaxy with little star formation, unlike the star-forming dwarf galaxies which typically host SLSNe. Its optical/UV spectra were mostly featureless, and its optical/UV SED near peak showed a blackbody temperature of $T_{\rm bb} = 2.1 \times 10^4$ K. After a decay phase in luminosity and temperature, *Swift* follow-up observations revealed a UV rebrightening of the source, accompanied by a blackbody temperature rise towards a roughly constant value and followed by a new luminosity decay. However, the transient spectra continued to be mostly featureless. ASASSN-15lh behaved unlike any other known SLSN and also tidal disruption event, but both these classes were considered to explain the transient origin. If a (peculiar) tidal disruption event was responsible for the observed emission, the mass of the destroyer BH could be estimated by relating it with the total stellar mass of the host galaxy ($\log(M_{\rm BH}/{\rm M}_\odot) = 8.88 \pm 0.60$) or with the galaxy bulge luminosity ($\log(M_{\rm BH}/{\rm M}_\odot) = 8.50 \pm 0.52$). Both these estimates imply a rapidly spinning BH to destroy a solar-mass star. Margutti et al. (2017), thanks to *Swift* and *Chandra* data, discovered a persistent weak soft X-ray emission from the position of the optical/UV transient.

CSS100217 (Drake et al. 2011): This luminous source was discovered during the optical Catalina Real-time Transient Survey (CRTS) on 2010. A past SDSS spectrum to its position resembled that of a narrow-line Seyfert 1 galaxy with significant ongoing star formation (CSS100217:102913+404220: RA(J2000)=10:29:12.56, DEC(J2000)=+40:42:20.00, $z = 0.148$), but the observed outburst was atypically rapid and large for an AGN and the lack of any archival radio counterpart excluded a jet. Due to the peculiarity of this source, Drake et al. (2011) performed follow-up multiwavelength observations. First of all, they found the optical flare to arise from the centre of its host galaxy and they detected an X-ray emission at the same position, making it a good candidate for a tidal disruption event. However its optical light curve, peak magnitude and blackbody temperature near peak were inconsistent with theoretical predictions for tidal disruption events. Spectroscopically, the transient showed strong variable narrow Balmer features typical of SNe IIn and also its optical light curve and temperature resembled that of supernovae, thus suggesting a possible association with a bright SN IIn, even though it is rare to find luminous supernovae near the core of AGNs.

CXOU J0332 (Bauer et al. 2017): This fast X-ray transient (RA(J2000)=03:32:38.77, DEC(J2000)=-27:51:33.7) was discovered by the *Chandra* Deep Field-South survey on October, 2014 and it was associated with a faint dwarf galaxy (RA(J2000)= 03:32:38.78, DEC(J2000)=-27:51:33.8, $z = 2.23$). Its X-ray emission exceptionally rose in about one hundred seconds and decayed in about three hundred seconds following a -1.53 power law trend in time. No optical, NIR and radio variable counterparts were detected. One possibility is that it was a highly beamed tidal disruption

event involving a white dwarf and an intermediate-mass BH ($\sim 10^3 - 10^4 \mathrm{M}_\odot$), even though this scenario can not completely explain all the observed properties.

DES14C1kia (Foley et al. 2015; Ravi & Shannon 2015; Yu et al. 2015): This UV/optical candidate tidal disruption event was discovered on November, 2014 by the Dark Energy Survey, at the centre of a passive galaxy (RA(J2000)=03:34:47.49, DEC(J2000)=-26:19:35.00, $z = 0.162$). It rose to the peak for seven weeks and then decayed, without significantly change its blue colour, and its optical spectrum during the bright state showed He II and He I emission lines. The flare was not detected in X-ray and radio observations on January, 2015.

Dougie (Vinkò et al. 2015): This optical transient (RA(J2000)=12:08:47.87, DEC(J2000)=+43:01:20.1) was discovered on 2009 by ROTSE, followed-up in the optical and UV by ROTSE-IIIb and *Swift*/UVOT and monitored in the X-rays by *Swift*/XRT, even though no X-ray source was detected at the position of the transient. Its light curve showed a fast rise (about ten days) and a steep decline (about sixty days). The source was slightly off-set from the centre of its likely host galaxy (SDSS J120847.77+430120.1: RA(J2000)=12:08:47.78, DEC(J2000)=+43:01:20.27, $z = 0.191$), which does not show any spectral feature typical of AGNs or star-forming galaxies. From the optical/UV SED of the transient near its peak, $T_{\rm bb} \sim 13000$ K, while by assuming the flare to be caused by the tidal disruption of a star by the central BH of the host galaxy, $\log M_{\rm BH}/\mathrm{M}_\odot = 5.29^{+0.91}_{-0.45}$ (Vinkò et al. (2015) fitted the flare with an amended version of a TDE model presented in Guillochon et al. (2014)).

F01004-2237 (Dou et al. 2017; Tadhunter et al. 2017): Ultraluminous infrared galaxies are the product of mergers between gas-rich galaxies, where the concentration of gas in the nuclear region leads to star formation and AGN activity, typically enshrouded in dust. Among them, F01004-2237 (RA(J2000)=01:02:50.007, DEC(J2000)=-22:21:57.22, $z = 0.118$) was suggested to harbour a UV/optical tidal disruption event. Indeed, Tadhunter et al. (2017), thanks to CSS (Catalina Sky Survey) data, discovered a luminous optical flare arising from its centre on June, 2010, which showed a significant flattening three years later. Such a flare was followed by the onset of broad helium emission lines in the source spectra. During the peak of the optical flare, F01004-2237 did not show variability in the mIR, but about three years later it displayed a rise at these wavelengths, which was interpreted as the dust reprocessed emission of the flare. The late-time flattening of the source optical light curve was also suggested to come from dust scattering of the flare. By relating $M_{\rm BH}$ with σ_*, $M_{\rm BH} \sim 2.5 \times 10^7 {\rm M}_\odot$.

IGR J12580 (Nikołajuk & Walter 2013; Irwin et al. 2015; Lei et al. 2016): This non-thermal, strong (variability factor of > 100), hard X-ray flare (RA(J2000)= 12:58:05.09, DEC(J2000)=+01:34:25.70) was discovered on 2011 by INTEGRAL and followed-up by *XMM-Newton*, *Swift* and MAXI. At these wavelengths, its flux increased in a few weeks, decreased over about a year, approximately following a $-5/3$ power law decay in time, and then suddenly dropped. A soft X-ray excess ($kT_{\rm bb} = 0.33 \pm 0.04$ keV) was also noticed, which was ascribed, however, to diffuse galaxy emission from outside the dusty torus of its host Seyfert 2 spiral galaxy (NGC 4845: RA(J2000)=12:58:01.24, DEC(J2000)=+01:34:32.09, $z = 0.00411$). This transient was interpreted as a candidate tidal disruption event involving a super-

Jupiter object. From X-ray short-term variability studies, $M_{\rm BH} \leq 9.6 \times 10^6 {\rm M}_\odot$ and $M_{\rm BH} = 2.3^{+1.1}_{-1.0} \times 10^5 {\rm M}_\odot$, while from a series of different relations, $M_{\rm BH}$ was estimated to be in the range $3 \times 10^5 - 1.8 \times 10^7 {\rm M}_\odot$. Irwin et al. (2015) also discovered a radio variable counterpart, which was suggested to be caused by the interaction of an off-beam relativistic jet associated with the tidal disruption event with the circumnuclear environment.

MAXI J1807+132 (Armas Padilla et al. 2017; Denisenko 2017; Kennea et al. 2017a; Kennea et al. 2017b; Kong et al. 2017; Munoz-Darias et al. 2017; Negoro et al. 2017; Shidatsu et al. 2017; Shields et al. 2017; Tachibana et al. 2017): This short-lived, quite soft X-ray flare was discovered by MAXI on March, 2017, at the position of a flare still detected about six years before. Follow-up optical and UV observations revealed also a highly variable optical/UV counterpart (RA(J2000)=18:08:07.549, DEC(J2000)=+13:15:05.40), while archival data suggested it to be a recurrent event. It could be a tidal disruption event, but optical spectra of the flare could resemble that of a low-mass X-ray binary.

NGC 1097 (Storchi-Bergmann et al. 1995): NGC 1097 (RA(J2000)=02:46:19.06, DEC(J2000)=-30:16:29.68, $z = 0.0042$) is a barred spiral galaxy, originally classified as a LINER. In 1991, broad, double-peaked Balmer lines emerged in its spectrum, and it entered the class of Seyfert 1 galaxies. Over three years, the optical flux and shape of these lines changed. Storchi-Bergmann et al. (1995) suggested the double-peaked Balmer lines to be produced by an elliptical ring consisting of debris produced in the tidal disruption of a star by the central BH of the galaxy. The precession of such a ring could also explain the profile variations.

NGC 2110 (Moran et al. 2007; Marinucci et al. 2015): NGC 2110 (RA(J2000)= 05:52:11.41, DEC(J2000)=-07:27:22.23, $z = 0.007579$) is an S0/E Seyfert 2 galaxy, more precisely classified as a double-peaked emission-line AGN. Indeed, Moran et al. (2007) discovered a broad, transient, double-peaked H_α emission line in its spectra (2005), which could be associated to an optical tidal disruption event. By relating $M_{\rm BH}$ with σ_*, $M_{\rm BH} = 2 \times 10^8 {\rm M}_\odot$.

NGC 247 (Feng et al. 2015): NGC 247 (RA(J2000)=00:47:08.55, DEC(J2000)= -20:45:37.44, $z = 0.000531$) is a quiescent nearby late-type spiral galaxy. Up to 2014, no X-ray emission from its nuclear region was detected in X-ray observations, but on July, 2014 *XMM-Newton* serendipitously discovered a bright X-ray nuclear flare ($L_{\rm X} \sim 2 \times 10^{39}$ erg ${\rm s}^{-1}$). Follow-up *Swift* XRT observations showed a fast rise and an exponential decay in its X-ray light curve, with a variability factor of ~ 17. On the contrary, simultaneous nuclear *Swift* UVOT observations displayed a constant UV flux, consistent with previous values, which was interpreted as arising from the galaxy nuclear star cluster. The X-ray flare was associated to a low-mass X-ray binary which contains a stellar-mass BH emitting near its Eddington limit in the nuclear star cluster or to a tidal disruption event caused by a nuclear low-mass BH. A fit of the *XMM-Newton* spectrum with a double-component model (accretion disc + power law) gave $T_{\rm bb} = 1.92^{+0.16}_{-0.33}$ keV as a sign of a hard X-ray spectrum.

NGC 6021 (Hryniewicz & Walter 2016): Based on *Swift* BAT archival data, Hryniewicz & Walter (2016) searched for hard X-ray flares in over 50000 galaxies which could be associated with unbeamed tidal disruption flares in inactive

galaxies. They found nine candidates, with NGC 6021 (RA(J2000)=15:57:30.72, DEC(J2000)=+15:57:21.60) being one of them. It was detected between January and March, 2005 with a hard X-ray variability factor of > 28 and it coincided with the centre of its homonymous galaxy (RA(J2000)=15:57:30.68, DEC(J2000)= +15:57:22.37, $z = 0.015607$).

OGLE16aaa (Wyrzykowski et al. 2017): This UV/optical tidal disruption candidate was discovered on 2016 by the OGLE-IV survey, coinciding with the centre of GALEXASC J010720.81-641621.4 (RA(J2000)=01:07:20.88, DEC(J2000)= -64:16:20.70, $z = 0.1655$), a galaxy that displays weak star formation and weak AGN emission. It showed a long rise, a slow decay, broad He II and H spectral lines and a blackbody temperature near peak of $T_{\rm bb} > 22000$ K. No X-ray counterpart was detected at the time of the UV/optical flare. Based on the light distribution of the source host galaxy and on light curve fitting with a TDE model discussed in Guillochon et al. (2014), Wyrzykowski et al. (2017) estimated the central BH mass to be $\log(M_{\rm BH}/{\rm M}_\odot) = 6.58$ and $M_{\rm BH} = 10^{6.2\pm0.1}{\rm M}_\odot$.

OGLE17aaj (Gromadzki et al. 2017; Sokolovsky et al. 2017; Stanway et al. 2017): This optical transient (RA(J2000)=1:56:24.93, DEC(J2000)=-71:04:15.7, $z = 0.116$) was discovered on 2017 by the OGLE-IV survey, at the centre of a likely star-forming non-active galaxy. Follow-up *Swift* observations revealed no X-ray emission at the position of the source and an UV counterpart consistent with a blackbody temperature of $T_{\rm bb} \sim 20000$ K.

PGC 015259 (Hryniewicz & Walter 2016): This is a candidate hard X-ray un-

beamed tidal disruption event (RA(J2000)=04:29:21.84, DEC(J2000)=-04:45:36.00) belonging to Hryniewicz & Walter's sample (2016). It was detected between February and April, 2010 with a hard X-ray variability factor > 30 and Hryniewicz & Walter (2016) suggested it to arise from the galaxy 2MFGC 3645 (RA(J2000)=04:29:21.82, DEC(J2000)=-04:45:35.60, $z = 0.014665$).

PGC 1127938 (Hryniewicz & Walter 2016): This is another candidate hard X-ray unbeamed tidal disruption event (RA(J2000)=01:18:56.64, DEC(J2000)= -01:03:10.80) belonging to Hryniewicz & Walter's sample (2016). It was detected between January and March, 2007 with a hard X-ray variability factor of > 29 and it was suggested to arise from the galaxy 2SLAQ J011844.35-010906.8 (RA(J2000)=01:18:44.36, DEC(J2000)=-01:09:06.87, $z = 0.02$).

PGC 1185375 (Hryniewicz & Walter 2016): This is another member of Hryniewicz & Walter's sample (2016) of hard X-ray unbeamed candidate tidal disruption events (RA(J2000)=15:03:50.40, DEC(J2000)=+01:07:37.20). It was detected on February, 2010, lasting forty one days, with a hard X-ray variability factor > 51.5 and it was suggested to arise from the galaxy 2MASX J15035028+0107366 (RA(J2000)=15:03:50.29, DEC(J2000)=+01:07:36.70, $z = 0.00523$).

PGC 1190358 (Hryniewicz & Walter 2016): PGC 1190358 (RA(J2000)=15:05:28.56, DEC(J2000)=+01:17:31.20) is another candidate hard X-ray unbeamed tidal disruption event, belonging to Hryniewicz & Walter's sample (2016). It was detected between December, 2009 and April, 2010, peaking forty days before becoming undetectable, with a hard X-ray variability factor of > 34 and it arose from the galaxy

N5846-162 (RA(J2000)=15:05:28.75, DEC(J2000)=+01:17:33.17, $z = 0.00766$).

PGC 133344 (Hryniewicz & Walter 2016): This is another candidate hard X-ray unbeamed tidal disruption event (RA(J2000)=21:42:55.92, DEC(J2000)= -30:07:58.80), belonging to Hryniewicz & Walter's sample (2016). It was detected between March and May, 2005 with a hard X-ray variability factor of > 14 and it was suggested to arise from the galaxy 6dFGS gJ214256.0-300758 (RA(J2000)=21:42:55.98, DEC(J2000)=-30:07:57.91, $z = 0.02365$).

PGC 170392 (Hryniewicz & Walter 2016): PGC 170392 is a candidate hard X-ray unbeamed tidal disruption event (RA(J2000)=22:26:46.32, DEC(J2000)= -15:01:22.80) which belongs to Hryniewicz & Walter's sample (2016). It was detected between November, 2005 and January, 2006 with a hard X-ray variability factor of > 35 and it was suggested to arise from the galaxy 6dFGS gJ222646.4-150123 (RA(J2000)=22:26:46.35, DEC(J2000)=-15:01:23.04, $z = 0.016246$).

Pictor A (Sulentic et al. 1995; Perley et al. 1997; Wilson et al. 2001): This radio galaxy (RA(J2000)=05:19:49.72, DEC(J2000)=-45:46:43.85, $z = 0.034$) showed a broad double-peaked H_α emission line, which increased in strength and complexity from 1983 to 1993, and which could be associated to an optical tidal disruption event. Perley et al. (1997) discovered a weak radio jet associated with the galaxy while Wilson et al. (2001), thanks to *Chandra* observations, discovered an X-ray jet at the same position.

PS1-12yp (Lawrence et al. 2016): Lawrence et al. (2016) discussed the pro-

ject of finding in the Pan-STARRS1 survey large amplitude transients associated with the centres of galaxies without previous evidence of AGNs. PS1-12yp (RA(J2000)=13:31:55.91, DEC(J2000)=+23:54:05.70; SDSS J133155.90+235405.8: RA(J2000)=13:31:55.90, DEC(J2000)=+23:54:05.8, $z = 0.581$) was the bluest transient of the sample and its optical luminosity experienced a significant increase and a decay similar to that of PS1-10jh, thus suggesting a possible tidal disruption nature.

PS16dtm (Blanchard et al. 2017): see chapter 6.

PTF-10iam (Arcavi et al. 2014; Arcavi et al. 2016): This is another of the tidal disruption candidates presented in Arcavi et al. (2014) (discovered on 2010, RA(J2000)=15:45:30.85, DEC(J2000)=+54:02:33.00), the only one clearly offset from the centre of its star-forming host galaxy (SDSS J154530.83+540231.9: RA(J2000)=15:45:30.83, DEC(J2000)=+54:02:31.91, $z = 0.109$). Its light curve rises faster to peak luminosity with respect to the other tidal disruption candidates presented in Arcavi et al. (2014) and its optical spectra showed broad H_α emission, typical of SNe II, and an unusual absorption feature, associated to high velocity H_α or Si II, typical of SNe Ia. Arcavi et al. (2016) suggested the event to be a peculiar SN II or a hybrid SN Ia-SN II. By fitting an event optical spectrum near peak with a blackbody model, $T_{\rm bb} \gtrsim 11000$ K.

PTF-10iya (Cenko et al. 2012a): This short-lived (about ten days) luminous UV/optical flare (RA(J2000)=14:38:41.00, DEC(J2000)=+37:39:33.60) was discovered on 2010 thanks to the PTF survey and coincided with the centre of SDSS

J143840.98+373933.4 (RA(J2000)=14:38:40.98, DEC(J2000)=+37:39:33.45, $z = 0.22405$), a star-forming, non-active galaxy. A significant X-ray emission at the position of the source was detected by *Swift* immediately after its discovery, but following observations did not reveal any X-ray counterpart. Cenko et al. (2012a) suggested that such an X-ray emission might come from a different process than that which produced the UV/optical flare (tidal disruption event). By fitting the source UV/optical SED near peak with a blackbody model, Cenko et al. found $T_{\rm bb} = (2.1 \pm 0.3) \times 10^4$ K and $T_{\rm bb} = (1.3 \pm 0.2) \times 10^4$ K with and without corrections for internal extinction. By relating $M_{\rm BH}$ with the bulge luminosity, $\log(M_{\rm BH}/{\rm M}_\odot) \lesssim 7.5$ and $\log(M_{\rm BH}/{\rm M}_\odot) \lesssim 7.0$, again with and without corrections for internal extinction.

PTF-10nuj (Arcavi et al. 2014): This is one of the two tidal disruption candidates presented in Arcavi et al. (2014) (discovered on 2010, RA(J2000)=16:26:24.70, DEC(J2000)=+54:42:21.60) with a very uncertain offset from the centre of their host galaxies (SDSS J162624.66+544221.4: RA(J2000)=16:26:24.66, DEC(J2000)= +54:42:21.44, $z = 0.132$). Its optical emission rises very quickly (about ten days) and then declines steeply (about thirty days) and its spectra showed strong emission lines. By fitting an event optical spectrum near peak with a blackbody model, $T_{\rm bb} \gtrsim 7000$ K.

PTF-11glr (Arcavi et al. 2014): This is the other tidal disruption candidate presented in Arcavi et al. (2014) (discovered on 2011, RA(J2000)=16:54:06.13, DEC(J2000)=+41:20:14.80) with a very uncertain offset from the centre of its host galaxy (SDSS J165406.16+412015.4: RA(J2000)=16:54:06.17, DEC(J2000)=

+41:20:15.45, $z = 0.207$). Its optical emission rises and declines very similarly to PTF-10nuj and its spectra showed strong emission lines. By fitting an event optical spectrum near peak with a blackbody model, $T_{\rm bb} \gtrsim 12500$ K.

PTF-15af (French et al. 2016): This transient was cited as an optical/UV tidal disruption event arising from the centre of the quiescent Balmer-strong galaxy SDSSJ084828.13+220333.4 (RA(J2000)=08:48:28.13, DEC(J2000)=+22:03:33.4, $z = 0.0790$), even if its discovery paper has not yet been published.

SDSS J0159 (LaMassa et al. 2015; Merloni et al. 2015): This source jumped to the eye because of significant differences in its classification from different epochs. It was classified on 2000 as a $z = 0.31167$ broad-line QSO from its optical spectrum (SDSS J015957.64+003310.4: RA(J2000)=01:59:57.64, DEC(J2000)=+00:33:10.49). On 2010 (and 2014), it was spectroscopically re-observed and classified as a $z = 0.31167$ weakly-active star-forming galaxy. SDSS J0159 showed a factor of 6 decay in its optical flux in these ten years. It was not detected in a RASS X-ray observation on 1991, and only upper limits were available from two ROSAT PSPC pointed observations on 1992. Following *XMM-Newton* observations on 2000 showed it in a bright X-ray state, with a flux decay by a factor of ~ 7 in a *Chandra* X-ray observation on 2005. Optical spectra thus revealed prominent broad emission lines at early times (2000) and narrow emission lines. Broad lines could be produced after the tidal disruption of a main sequence star by the central BH of the galaxy, when the tidal disruption flare illuminated a pre-existing structure (Broad Line Region) in a formerly active galaxy, narrow lines could be produced by ionisation from nuclear activity or from newly formed stars (Merloni et al. 2015). Based

on line width, continuum luminosity and BH mass relations, LaMassa et al. (2015) derived $M_{\rm BH} \sim 1.7 \times 10^8 {\rm M}_\odot$. Merloni et al. (2015) confirmed $M_{\rm BH} \sim 10^8 {\rm M}_\odot$ thanks to line width, line luminosity and BH mass relations.

SDSS J0748 (Wang et al. 2011; Wang et al. 2012; Dou et al. 2016): An SDSS spectrum (2004) of the star-forming galaxy SDSS J074820.67+471214.3 (RA(J2000)=07:48:20.67, DEC(J2000)=+47:12:14.23, $z = 0.0615$) was analysed by Wang et al. (2011; 2012), who detected strong high-ionisation emission lines and broad bumps, together with a brightening by ~ 0.2 magnitudes over four months. Follow-up observations of the galaxy four-five years later displayed a fading of the high-ionisation lines, of the broad bumps and of the continuum emission. Wang et al. (2011; 2012) identified as the cause of such spectral features the tidal disruption of an evolved star by the central BH of the galaxy. Indeed, the UV/X-ray radiation emitted by the tidal disruption flare could highly ionise the circumnuclear gas, thus producing the high-ionisation emission lines, while the broad bumps could be the blushifted He II and Balmer lines produced, for example, via reprocession by the unbound debris (Strubbe & Quataert 2009). A fit of the first SDSS spectrum of the galaxy with a blackbody model plus gaussians for bumps gave $T_{\rm bb} = (1.3 \pm 0.4) \times 10^4$ K. From scaling relations involving the luminosity of the galaxy and the stellar velocity dispersion, $M_{\rm BH} = 10^5 - 10^6 {\rm M}_\odot$. Dou et al. (2016) noticed a significant mIR emission arising from the source position many years later and associated it to the heating of the circumnuclear environment by the tidal disruption flare.

SDSS J0938 (Wang et al. 2012; Yang et al. 2013): Wang et al. (2012) per-

formed a systematic search for extreme coronal line emitters among SDSS galaxies, assuming that these lines come from the high ionisation by tidal disruption flares of their circumnuclear gas. SDSS J0938 (SDSS J093801.64+135317.0: RA(J2000)=09:38:01.64, DEC(J2000)=+13:53:17.08, $z = 0.1006$) was one of the resulting candidates. However, based on follow-up spectroscopic observations, Yang et al. (2013) still detected these high-ionisation emission lines, superimposed over narrower low-ionisation lines which came from star-forming regions, thus suggesting that this source could be an AGN.

SDSS J0939 (Esquej et al. 2007): Esquej et al. (2007) suggested it to be a candidate X-ray tidal disruption event, based on its discovery in an *XMM-Newton* slew on 2004 with a soft X-ray flux 81 times higher than its RASS upper limit. However, the candidate host (SDSS J093922.90+370944.0: RA(J2000)=09:39:22.89, DEC(J2000)=+37:09:43.90, $z = 0.18589$) is a narrow-line Seyfert 1 galaxy, thus questioning whether it came from AGN variability.

SDSS J0952 (Komossa et al. 2008; Dou et al. 2016; Palaversa et al. 2016): Strong, high-ionisation emission lines were discovered in an optical/UV spectrum (2005) of the galaxy SDSS J095209.56+214313.3 (RA(J2000)=09:52:09.56, DEC(2000)=+21:43:13.24, $z = 0.0789$), together with a strong He II emission and multi-component Balmer lines. These lines significantly faded over two years. Multiwavelength photometry showed variability at NUV, optical and NIR wavelengths. Komossa et al. (2008) associated this variability to a large-amplitude EUV-X-ray outburst, not directly observed at these wavelengths, associated with a tidal disruption event, with the emission lines being the "light echo" of the flare when it crossed

the circumnuclear gas. Based on additional optical and UV observations, Palaversa et al. (2016) associated the outburst with the centre of the discussed galaxy and detected a long-lived UV emission, linked at late times with star formation in the host, likely non-active (no typical emission of AGNs was detected), galaxy. Dou et al. (2016) noticed a fading long-lasting mIR emission, which they associated to the heating of the circumnuclear dust by the tidal disruption flare. By relating $M_{\rm BH}$ with σ_*, $M_{\rm BH} = 7 \times 10^6 {\rm M}_\odot$.

SDSS J1011 (Runnoe et al. 2016): This source was classified as a "changing look" quasar (SDSS J101152.98+544206.4: RA(J2000)=10:11:52.99, DEC(J2000)= +54:42:06.50, $z = 0.24608$). On 2003, during its bright state, its optical spectrum showed a blue continuum and broad emission lines, while on 2015, during its dim state, these features faded and only a weak H_α emission line remained. Runnoe et al. (2016) attributed the changes in the spectra to abrupt changes in the accretion onto the BH, but they considered also a tidal disruption scenario. The decay rate of the source light curve was consistent with a tidal disruption event but its bright phase before decay was too long for a typical tidal disruption event. Based on line width, continuum luminosity and BH mass relations, $M_{\rm BH} = (3.6 \pm 0.2) \times 10^7 {\rm M}_\odot$ and $M_{\rm BH} = (4.7 \pm 0.1) \times 10^7 {\rm M}_\odot$ in the bright phase from H_β and H_α, $M_{\rm BH} = (1.8 \pm 0.3) \times 10^7 {\rm M}_\odot$ in the dim phase from H_α (H_β was not detected).

SDSS J1055 (Wang et al. 2012; Yang et al. 2013): This source (SDSS J105526.41 +563713.1: RA(J2000)=10:55:26.42, DEC(J2000)=+56:37:13.09, $z = 0.0743$) is one of the extreme coronal line emitters identified by Wang et al. (2012). It

spectrally showed strong high-ionisation emission lines and broad Balmer lines and thus it was classified as a tidal disruption event. However it also showed features typical of Seyfert 1 galaxies.

SDSS J1201 (Saxton et al. 2012; Liu et al. 2014): This candidate tidal disruption event was discovered in the context of a systematic search for extragalactic flaring sources, found in *XMM-Newton* slews with a strong increase in flux with respect to their RASS upper limits. It was detected in an *XMM-Newton* slew on June, 2010, with a flux 56 times greater than during the RASS, at the centre of the inactive galaxy SDSS J120136.02+300305.5 (RA(J2000)=12:01:36.03, DEC(J2000)=+30:03:05.52, $z = 0.146$). A fit of its poor *XMM-Newton* slew spectrum with a blackbody model ($N_{\rm H} = N_{\rm H_{Gal}} = 1.4 \times 10^{20} {\rm cm}^{-2}$) gave $kT_{\rm bb} \sim 0.1$ keV and optical spectra of the transient did not show emission lines. Follow-up *Swift* and *XMM-Newton* pointed X-ray observations displayed an approximately $-5/3$ power law flux decay and an unusual spectral softening in time (X-ray spectra were not well fitted by blackbody models), while follow-up *Swift* and *XMM-Newton* UV observations revealed the source to be faint at these wavelengths. The transient was not detected in the radio band. By relating $M_{\rm BH}$ with the K bulge luminosity, accounting for uncertainties in the host galaxy type, $3 \times 10^5 {\rm M}_\odot < {\rm M_{BH}} < 2 \times 10^7 {\rm M}_\odot$, even though the maximum value seems to be the most likely because of evidences that the host is an early-type galaxy. Actually, the transient light curve showed strong dips in the X-ray flux. Liu et al. (2014) interpreted these features as coming from the tidal disruption of a star in a BH binary system, where the star is disrupted by the primary BH while the secondary perturbs the produced stream, causing the interruptions.

SDSS J1241 (Gelbord et al. 2009; Wang et al. 2012; Yang et al. 2013): This source (SDSS J124134.25+442639.2: RA(J2000)=12:41:34.26, DEC(J2000)=+44:26:39.23, $z = 0.0419$) was classified as an extreme coronal line emitter. However, Yang et al. (2013) noticed that these lines did not vary significantly over time, thus suggesting that they were associated with a persistent AGN rather than with a tidal disruption event.

SDSS J1323 (Esquej et al. 2007; Esquej et al. 2008; Esquej et al. 2012): This highly variable X-ray source was discovered in an *XMM-Newton* slew on 2003, with a soft X-ray flux 83 times higher than its RASS upper limit. Optical observations of its host taken before the outburst showed no emission lines, thus suggesting a non-active galaxy (SDSS J132341.97+482701.3: RA(J2000)=13:23:41.97, DEC(J2000)=+48:27:01.26, $z = 0.08754$). Following *XMM-Newton* and *Swift* observations of the source taken about two years after the *XMM-Newton* slew showed an X-ray flux decline by a factor of ~ 40, following the $-5/3$ power law decay in time typical of tidal disruption events. The flare *XMM-Newton* slew spectrum had too few counts to allow spectral fitting. From $M_{\rm BH} - \sigma_*$ different relations, $M_{\rm BH} = (1.3 - 6.4) \times 10^6 {\rm M}_\odot$, by relating $M_{\rm BH}$ with the V magnitude of the host galaxy, $M_{\rm BH} = (3.3 \pm 0.9) \times 10^7 {\rm M}_\odot$.

SDSS J1342 (Yang et al. 2013; Dou et al. 2016): This source (SDSS J134244.41 +053056.1: RA(J2000)=13:42:44.42, DEC(J2000)=+05:30:56.14, $z = 0.0366$) was identified as a potential tidal disruption event. Indeed, it showed high-ionisation emission lines in an SDSS spectrum, but these lines disappeared some years later. Moreover, Dou et al. (2016) detected late-time mIR emission arising from the

source position and associated it to the heating of the circumnuclear environment by the tidal disruption flare.

SDSS J1350 (Yang et al. 2013; Dou et al. 2016): This is another candidate tidal disruption event classified thanks to its high-ionisation emission lines (SDSS J135001.49+291609.7: RA(J2000)=13:50:01.51, DEC(J2000)=+29:16:09.71, $z = 0.0777$). Dou et al. (2016) identified a fading long-lasting mIR emission at the position of the source, which they associated to the heating of the circumnuclear environment by the tidal disruption flare.

Swift J1112-82 (Brown et al. 2015; Peng et al. 2016): This source was discovered in the hard X-rays on June, 2011 by the *Swift* BAT telescope and became quiescent at these wavelengths after a few days. It showed a non-thermal softer X-ray bright counterpart, whose luminosity early decayed over time following a -1.1 power law and later displayed a sharper decline, and a faint UV/optical counterpart, at RA(J2000)=11:11:47.32, DEC(J2000)=-82:38:44.20. Its optical spectra revealed only a single emission line at $z = 0.89$. Swift J1112-82 was suggested to be a relativistic tidal disruption event occurring at the centre of the faint galaxy Swift J1112.2-8238 (RA(J2000)=11:11:47.80, DEC(J2000)=-82:38:44.71). Based on relations between the total stellar mass of the host galaxy, the bulge mass and the central BH mass, $M_{\rm BH} \sim 5 \times 10^6 {\rm M}_\odot$ and $M_{\rm BH} \sim 2 \times 10^6 {\rm M}_\odot$.

Swift J1644+57 (Bloom et al. 2011; Burrows et al. 2011; Levan et al. 2011; Zauderer et al. 2011; Cheng et al. 2016; Levan et al. 2016; Mangano et al. 2016): This source was discovered in the hard X-rays on March, 2011 by the *Swift* BAT

telescope and at these wavelengths it displayed multiple flares before dropping dramatically within a few days. It showed a non-thermal softer X-ray bright counterpart at RA(J2000)=16:44:49.92, DEC(J2000)=+57:35:00.6, which displayed a short phase of multiple flares, a rapid flux decline, an abrupt rise and a final decay (with occasional dips) which approximately followed a $-5/3$ power law trend in time, before suddenly drop. A NIR and a bright radio counterparts were also detected. Swift J1644+57 was suggested to be a relativistic tidal disruption event occurring at the centre of the star-forming inactive galaxy Swift J164449.3+573451 (RA(J2000)=16:44:49.30, DEC(J2000)=+57:34:51.00, $z = 0.3534$). The X-ray emission probably arose in the base of the tidal disruption accretion-powered jet, the radio and NIR emission likely came from the forward shock of the jet, while the flare optical/UV emission was possibly obscured by dust. By equalising the light crossing time of the Schwarzschild radius and the time of minimum variability in the transient X-ray light curve, $M_{\rm BH} \sim 8 \times 10^6 {\rm M}_\odot$, while by relating $M_{\rm BH}$ with the bulge luminosity, $M_{\rm BH} \lesssim 2 \times 10^7 {\rm M}_\odot$.

Swift J2058+05 (Krimm et al. 2011; Cenko et al. 2012b; Pasham et al. 2015): This source was discovered in the hard X-rays on May, 2011 by the *Swift* BAT telescope and became quiescent at these wavelengths after about fifteen days. It showed a non-thermal softer X-ray bright counterpart at RA(J2000)=20:58:19.90, DEC(J2000)=+05:13:32.0, whose luminosity early decayed over time following a -2.2 power law and later displayed a sudden intense decrease, an optical relatively faint counterpart at RA(J2000)=20:58:19.90, DEC(J2000)=+05:13:32.2, which abruptly dimmed as the X-ray counterpart, and a luminous radio counterpart at RA(J2000)=20:58:19.898, DEC(J2000)=+05:13:32.25, which slightly weakened

over time. Its optical spectra revealed no emission lines, unlike narrow-line Seyfert galaxies, and strong absorption features at $z = 1.1853$ at early times, which, however, do not resembled those typically observed in BL Lac spectra. The transient UV/optical/IR SED near the time of discovery came out to be well fitted by a blackbody of $T_{\rm bb} = (2.9 \pm 0.5) \times 10^4$ K, while two of its optical/NIR spectra revealed blackbody temperatures of $T_{\rm bb} = (1.8 \pm 0.2) \times 10^4$ K and $T_{\rm bb} = (2.3 \pm 0.1) \times 10^4$ K, respectively, in agreement with the SED fit. Swift J2058+05 was suggested to be a relativistic tidal disruption event occurring at the centre of the galaxy Swift J205819.7+051329 (RA(J2000)=20:58:19.85, DEC(J2000)=+05:13:33.00). The radio emission probably came from the forward shock of a relativistic jet, the X-ray emission likely arose in the base of the jet, the optical emission maybe represented the flare reprocessing. The sudden flux decrease in the optical and X-rays was associated with a transition from a super-Eddington to a sub-Eddington accretion phase. Based on this interpretation and on Eddington assumptions, the central BH mass was estimated to be $10^4 {\rm M}_\odot \lesssim {\rm M}_{\rm BH} \lesssim 2 \times 10^6 {\rm M}_\odot$, setting the X-ray-emitting radius equal to the Schwarzschild radius $M_{\rm BH} \sim 5 \times 10^7 {\rm M}_\odot$, while from $M_{\rm BH} - L_{\rm bulge}$ relations $M_{\rm BH} \lesssim 3 \times 10^7 {\rm M}_\odot$.

UGC 01791 (Hryniewicz & Walter 2016): This is another candidate hard X-ray unbeamed tidal disruption event (RA(J2000)=02:19:53.52, DEC(J2000)=+28:14:52.80) belonging to Hryniewicz & Walter's sample (2016). It was detected between January and April, 2005, peaking about thirty days before becoming undetectable, with a hard X-ray variability factor of > 47 and Hryniewicz & Walter (2016) suggested it to arise from its homonymous galaxy (RA(J2000)=02:19:53.66, DEC(J2000)=+28:14:52.60, $z = 0.015881$).

UGC 03317 (Hryniewicz & Walter 2016): This is the last of hard X-ray unbeamed tidal disruption candidates selected by Hryniewicz & Walter (2016) (RA(J2000)= 05:33:37.68, DEC(J2000)=+73:43:26.40). It was detected between September and November, 2010 with a hard X-ray variability factor of > 40 and it arose from its homonymous galaxy (RA(J2000)=05:33:37.54, DEC(J2000)=+73:43:26.30, $z = 0.004136$).

X J1231+1106 (Ho et al. 2012; Lin et al. 2013; Lin et al. 2017a): This soft X-ray candidate tidal disruption event was serendipitously detected in two *XMM-Newton* epochs, on July, 2003 and December, 2005, slightly increasing its X-ray luminosity. It arose from the galaxy SDSS J123103.24+110648.6 ($z = 0.11871$), which is a low-luminosity Seyfert 2 dwarf galaxy with evidences of star-forming activity. Follow-up *Swift* (2013-2014) and *Chandra* (2016) observations of the source revealed a significant X-ray flux decline compared to *XMM-Newton* observations. A fit with an accretion disc plus power law model of the last source *XMM-Newton* X-ray spectrum gave $kT_{\rm bb} = 0.18 \pm 0.01$ keV, while a fit with the same model of the source *Swift* and *Chandra* X-ray spectra gave $kT_{\rm bb} = 0.15^{+0.07}_{-0.05}$ keV and $kT_{\rm bb} = 0.09^{+0.03}_{-0.02}$ keV, respectively. Faint UV emission was noticed at the position of the X-ray transient, without significant variability, and it was associated with the host star-forming activity. By relating $M_{\rm BH}$ with σ_*, $M_{\rm BH} \sim 10^5 {\rm M}_\odot$, while linking $M_{\rm BH}$ to the total galaxy stellar mass, $M_{\rm BH} = 1.5 \times 10^6 {\rm M}_\odot$. The long duration of the event could be caused by a long super-Eddington accretion phase or by slow circularisation.

X J1500+0154 (Lin et al. 2017b): This super-long (> 11 yr) candidate tidal disruption event (RA(J2000)=15:00:52.068, DEC(J2000)=+01:54:53.79) appeared in several *Chandra* and *XMM-Newton* X-ray observations from 2005 to 2011. It remained undetected in a *Chandra* observation on April, 2005, it was detected in an *XMM-Newton* observation on July, 2005, it appeared even brighter in *Chandra* and *XMM-Newton* observations about three years later and it weakened only slightly in other *Chandra* observations. Moreover, follow-up *Chandra* and *Swift* observations revealed the X-ray transient at similar luminosities. The long duration of the flare was suggested to be caused by slow circularisation of the accretion disc. It arose from the centre of the likely inactive dwarf starburst galaxy SDSS J150052.07+015453.8 ($z = 0.145$). By relating the total stellar mass of the galaxy with the central BH mass, $M_{\rm BH} \sim 10^6 {\rm M}_{\odot}$. The transient X-ray spectra are soft and well fitted by a Comptonsation model, which could be explained by a super-Eddington accretion state. A late-time *Chandra* spectrum was even softer and also cooler, suggesting a temporal transition to the standard thermal state or the presence of a transient warm absorber.

XMMSL1J0740-85 (Alexander et al. 2017; Saxton et al. 2017): This candidate tidal disruption event (RA(J2000)=07:40:08.43, DEC(J2000)=-85:39:31.4) was discovered on April, 2014 during an *XMM-Newton* slew, at the centre of the quiescent post-starburst galaxy 2MASX J2007400785-8539307 (RA(J2000)=07:40:08.09, DEC(J2000)=-85:39:31.30, $z = 0.0173$). At X-ray wavelengths, its non-thermal hard and thermal ($kT_{\rm bb} = 86 \pm 2$ eV) soft emission increased by a factor of 20 and then decreased by a factor of 70, approximately following a $-5/3$ power law decay in time, while at UV wavelengths, the source thermal emission decayed by a factor

of 12 following a -1.2 power law. A weak radio counterpart was also detected and associated with a non-relativistic gas outflow. By relating $M_{\rm BH}$ with the bulge luminosity, $M_{\rm BH} \sim 6 \times 10^6 {\rm M}_\odot$, while from the short-term X-ray variability study $M_{\rm BH} = 3.5^{+6.5}_{-2.4} \times 10^6 {\rm M}_\odot$.

Name	Disc. year	Host name	Host RA(J2000), DEC(J2000)	z	$T_{\rm peak}$ (K)	$L_{\rm peak}$ (erg $\rm s^{-1}$)	Variab. factor	$M_{\rm BH}$ ($\rm M_\odot$)	References
2XMMi J1847	2006	IC 4765-f01-1504	18:47:25.14, -63:17:24.77	0.0353	1.1×10^6	6.4×10^{43}	> 64[r] > 12[d]	$10^6 - 10^7$ [a] $(0.06 - 3.81) \times 10^6$ [b]	Lin et al. (2011)
3XMM J152130.7 +074916	2000	3XMM J152130.7 +074916	15:21:30.73, +07:49:16.52	0.1790	2×10^6	5×10^{43}	> 260	$(1.9 \pm 0.4) \times 10^5$ [b] $(1.4 \pm 0.3) \times 10^6$ [b] 2×10^7 [c] $\lesssim 5 \times 10^7$ [a]	Lin et al. (2015)
ASASSN-14ae	2014	SDSS J110840.11 +340552.2	11:08:40.12, +34:05:52.23	0.0436	2×10^4	8×10^{43}	> 30[d]	$\lesssim 10^{6.8}$ [c,d]	Holoien et al. (2014)
ASASSN-14li	2014	SDSS J124815.23 +174626.4	12:48:15.23, +17:46:26.44	0.0206	3.5×10^4 (UV/opt)	10^{44}	> 16[d] (UV/opt)	$10^{6.7}$ [d]	Miller et al. (2015) Alexander et al. (2016) Cenko et al. (2016)

(Continue to the next page)

(Continue from the previous page)

Name	Disc. year	Host name	Host RA(J2000), DEC(J2000)	z	$T_{\rm peak}$ (K)	$L_{\rm peak}$ (erg $\rm s^{-1}$)	Variab. factor	$M_{\rm BH}$ ($\rm M_\odot$)	References
					10^5 (X)			2.5×10^6 [e] $\lesssim 1.9 \times 10^6$ [f] $(0.4-1.2) \times 10^6$ [g]	Holoien et al. (2016a) van Velzen et al. (2016) Brown et al. (2017a)
ASASSN-15oi	2015	2MASX J20390918 -3045201	20:39:09.18, -30:45:20.10	0.0484	2×10^4	1.3×10^{44}	> 5.5[d]	$10^{7.1}$ [d]	Holoien et al. (2016b)
D1-9	2004	GALEX J022517.0 -043258	02:25:17.00, -04:32:59.00	0.326	5.5×10^4	4×10^{43}	> 6[r] > 2.5[d]	< 4×10^7 [f] > 8.2×10^6 [h] $1^{+2}_{-0.7} \times 10^8$ [a] 2.4×10^7 [i]	Gezari et al. (2008) Gezari et al. (2009)
D23H-1	2007	SDSS J233159.53 +001714.5	23:31:59.54, +00:17:14.58	0.1855	1.7×10^5	3×10^{45}	> 6[d]	$(5.4 \pm 0.4) \times 10^7$ [i]	Gezari et al. (2009)

(Continue to the next page)

(Continue from the previous page)

Name	Disc. year	Host name	Host RA(J2000), DEC(J2000)	z	$T_{\rm peak}$ (K)	$L_{\rm peak}$ (erg $\rm s^{-1}$)	Variab. factor	$M_{\rm BH}$ ($\rm M_\odot$)	References
								$< 6.26 \times 10^6$ [d] $10^{7\pm1}$ [c]	
D3-13	2004	GALEX J141929.8 +525206	14:19:29.81, +52:52:06.37	0.3698	4.9×10^4	6.3×10^{43}	> 6[d]	$< 8.7 \times 10^7$ [f] $> 2.4 \times 10^6$ [h] $2^{+2}_{-1} \times 10^7$ [c] 1.2×10^7 [i]	Gezari et al. (2006) Gezari et al. (2008) Gezari et al. (2009)
IC3599	1990	IC 3599*	12:37:41.18, +26:42:27.24	0.0212	9.6×10^5	5.5×10^{43}	> 100	$(2-12) \times 10^6$ [a,c]	Brandt et al. (1995) Grupe et al. (1995) Vaughan et al. (2004) Sani et al. (2010) Bower et al. (2013) Campana et al. (2015) Grupe et al. (2015)
iPTF16axa	2016	SDSS J170334.34	17:03:34.34, +30:35:36.6	0.108	3×10^4	1.1×10^{44}	> 4[d]	$5.0^{+7.0}_{-2.9} \times 10^6$ [c]	Hung et al. (2017)

(Continue to the next page)

(Continue from the previous page)

Name	Disc. year	Host name	Host RA(J2000), DEC(J2000)	z	$T_{\rm peak}$ (K)	$L_{\rm peak}$ (erg s^{-1})	Variab. factor	$M_{\rm BH}$ ($M_\odot$)	References
		+303536.6							
iPTF16fnl	2016	Mrk950	00:29:57.01, +32:53:37.24	0.0163	3×10^4	10^{43}	> 40[d]	$\lesssim 10^{6.6\pm0.4}$ [d] $10^{6.33\pm0.38}$ [c] $\lesssim 5.5 \times 10^6$ [d]	Blagorodnova et al. (2017) Brown et al. (2017b)
LEDA 095953	1992	LEDA 095953	13:47:30.10, -32:54:52.00	0.0366	1.4×10^6	6.3×10^{42}	> 650[d]	10^7 [a]	Cappelluti et al. (2009)
NGC3599	2003	NGC 3599*	11:15:26.95, +18:06:37.33	0.0027	1.1×10^6	5×10^{41}	> 100	$(0.7-4.1)\times10^6$ [c] $(3.5\pm0.9)\times10^7$ [j] $(3.1\pm1.5)\times10^7$ [a]	Esquej et al. (2007) Esquej et al. (2008) Esquej et al. (2012) Saxton et al. (2015)
NGC5905	1990	NGC 5905	15:15:23.32,	0.0112	6.5×10^5	2.6×10^{42}	> 80[d]	$10^4 - 10^5$ [e]	Bade et al. (1996)

(Continue to the next page)

(Continue from the previous page)

Name	Disc. year	Host name	Host RA(J2000), DEC(J2000)	z	$T_{\rm peak}$ (K)	$L_{\rm peak}$ (erg s^{-1})	Variab. factor	$M_{\rm BH}$ ($M_\odot$)	References
			+55:31:01.59					$10^7 - 10^8$ [a]	Komossa & Bade (1999) Li et al. (2002) Gezari et al. (2003) Gezari et al. (2004) Halpern et al. (2004)
PS1-10jh	2010	SDSS J160928.27 +534023.9	16:09:28.28, +53:40:23.99	0.1696	$\gtrsim 3 \times 10^4$	$\gtrsim 2.2 \times 10^{44}$	> 100	$4^{+4}_{-2} \times 10^6$ [d] $(1.9 \pm 0.1) \times 10^6$ [i]	Gezari et al. (2012) Gaskell & Rojas Lobos (2014) Guillochon et al. (2014) Strubbe & Murray (2015)
PS1-11af	2010	SDSS J095726.82 +031400.9	09:57:26.82, +03:14:00.94	0.4046	2×10^4	8.5×10^{43}	> 6	$(8 \pm 2) \times 10^6$ [d] $< (1.6 \pm 0.4) \times 10^7$ [k]	Chornock et al. (2014)
PTF-09axc	2009	SDSS J145313.07 +221432.2	14:53:13.08, +22:14:32.27	0.1146	$\gtrsim 1.2 \times 10^4$	1.9×10^{43}	> 10	$2.69^{+0.66}_{-0.64} \times 10^6$ [d]	Arcavi et al. (2014)

(Continue to the next page)

(Continue from the previous page)

Name	Disc. year	Host name	Host RA(J2000), DEC(J2000)	z	$T_{\rm peak}$ (K)	$L_{\rm peak}$ (erg s^{-1})	Variab. factor	$M_{\rm BH}$ ($M_\odot$)	References
PTF-09djl	2009	SDSS J163355.97 +301416.6	16:33:55.97, +30:14:16.65	0.184	$\gtrsim 2.6 \times 10^4$	1.2×10^{44}	> 10	$3.57^{+9.97}_{-2.96} \times 10^6$ [d]	Arcavi et al. (2014)
PTF-09ge	2009	SDSS J145703.17 +493640.9	14:57:03.18, +49:36:40.97	0.064	$\gtrsim 2.2 \times 10^4$	5.7×10^{43}	> 10	$5.65^{+3.02}_{-0.98} \times 10^6$ [d]	Arcavi et al. (2014)
RBS 1032	1990	SDSS J114726.69 +494257.8	11:47:26.80, +49:42:59.00	0.026	$> 8 \times 10^5$	10^{43}	> 200[d]	5×10^4 [b] $\lesssim 10^{6.4}$ [a]	Ghosh et al. (2006) Maksym et al. (2014a)
RX J1242-11A	1992	RX J1242.6 -1119A	12:42:36.90, -11:19:35.00	0.05	7×10^5	8.8×10^{43}	> 200[d]	7×10^5 [e] 2×10^8 [a]	Komossa & Greiner (1999) Gezari et al. (2003) Gezari et al. (2004) Halpern et al. (2004) Komossa et al. (2004)
RX J1420+53	1990	RX J1420.4	14:20:24.37,	0.147	4.4×10^5	10^{44}	> 150	7×10^5 [b]	Greiner et al. (2000)

(Continue to the next page)

(Continue from the previous page)

Name	Disc. year	Host name	Host RA(J2000), DEC(J2000)	z	$T_{\rm peak}$ (K)	$L_{\rm peak}$ (erg $\rm s^{-1}$)	Variab. factor	$M_{\rm BH}$ ($\rm M_\odot$)	References
		+5334	+53:34:11.72						
RX J1624+75	1990	RX J1624.9 +7554	16:24:56.66, +75:54:56.09	0.0636	1.2×10^6	1.6×10^{44}	> 6000[d]	10^6 [e]	Grupe et al. (1999) Gezari et al. (2003) Gezari et al. (2004) Halpern et al. (2004)
SDSS J1311	2004	SDSS J131122.15 -012345.6	13:11:22.15, -01:23:45.61	0.18	1.4×10^6	5×10^{42}	> 30[r] > 9[d]	$10^{6.46\pm0.38}$ [a]	Maksym et al. (2010) Bower et al. (2013)
TDE1	2006	SDSS J234201.40 +010629.2	23:42:01.41, +01:06:29.30	0.136	2.4×10^4	5.4×10^{42}	> 6	$(6-20) \times 10^{6\pm0.3}$ [a]	van Velzen et al. (2011)
TDE2	2007	SDSS J232348.61 -010810.3	23:23:48.62, -01:08:10.34	0.2515	1.8×10^4	4.1×10^{43}	> 6	$(2-10) \times 10^{7\pm0.3}$ [a]	van Velzen et al. (2011)
WINGS	1999	WINGS	13:48:49.88,	0.062	$< 1.2 \times 10^6$	$> 2 \times 10^{42}$	> 50[d]	$10^5 - 10^6$ [a,d]	Maksym et al. (2013)

(Continue to the next page)

(Continue from the previous page)

Name	Disc. year	Host name	Host RA(J2000), DEC(J2000)	z	$T_{\rm peak}$ (K)	$L_{\rm peak}$ (erg $\rm s^{-1}$)	Variab. factor	$M_{\rm BH}$ ($\rm M_{\odot}$)	References
(A1795)		J134849.88 +263557.5	+26:35:57.50					7×10^5 [c] 1.3×10^4 [e] 1.5×10^5 [e]	Donato et al. (2014) Maksym et al. (2014b)
XMMSL1 J0630-60									(see chapter 3)

(Continue to the next page)

(Continue from the previous page)

Name	Disc. year	Host name	Host RA(J2000), DEC(J2000)	z	$T_{\rm peak}$ (K)	$L_{\rm peak}$ (erg $\rm s^{-1}$)	Variab. factor	$M_{\rm BH}$ ($\rm M_\odot$)	References

Table 2.1: The Gold Sample of tidal disruption candidates. Table columns report the name associated with the event, the year of discovery, the name of the host galaxy (* marks active galaxies), the host RA, DEC and z, the peak temperature of the event, the peak luminosity of the event, the variability factor in luminosity (r means in the rise phase, d in the decay phase), the central BH mass and the references for the event. Letters next to $M_{\rm BH}$ point out the method adopted in its evaluation:

a - relation with the galaxy bulge luminosity

b - inference from the inner accretion disc radius; estimate from spectral fitting

c - relation with σ_*

d - relation with the galaxy bulge stellar mass

e - inference from Eddington arguments

f - inference from imposing that the X-ray emission comes from outside the radius of innermost stable circular orbit

g - inference from the TDE model discussed in Guillochon et al. (2014)

h - inference from the tidal disruption flare start time and the time of stellar disruption

i - inference from the model discussed in Lodato et al. (2009)

j - relation with the galaxy magnitude

k - relation with the galaxy total stellar mass

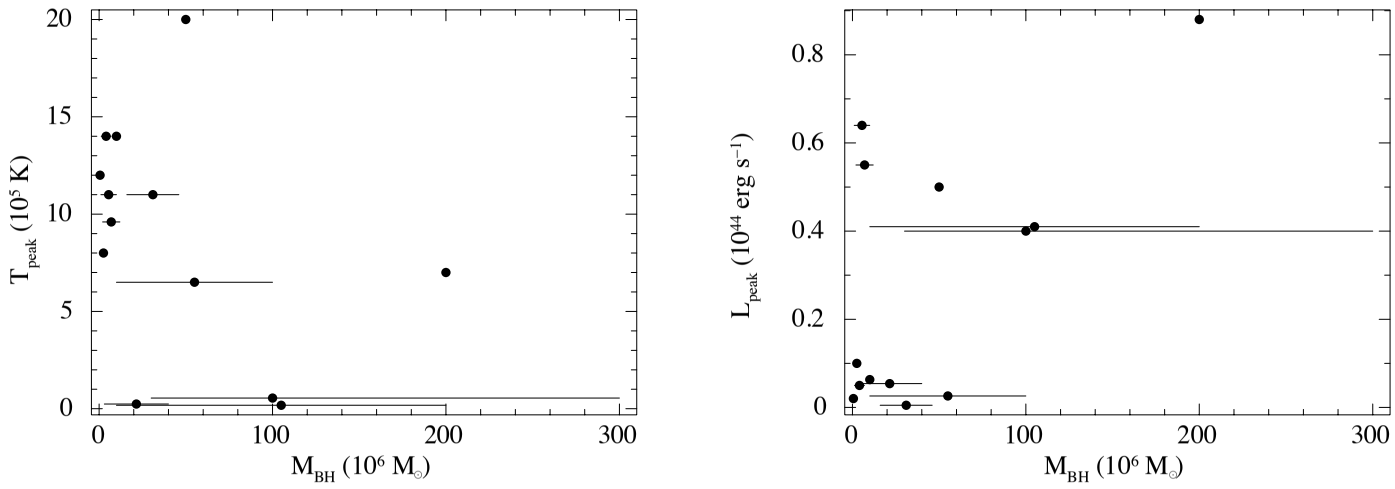

Figure 2.1: Plot of $T_{\rm peak}$ vs. $M_{\rm BH}$ (left panel) and $L_{\rm peak}$ vs. $M_{\rm BH}$ (right panel) for 13 tidal disruption candidates belonging to the Gold Sample (see Table 2.1). Method 'a' in Table 2.1 adopted in the evaluation of $M_{\rm BH}$ was selected for consistency in the results, in order to have a fairly large sample to investigate. No relation can be found between the represented properties.

Chapter 3

XMMSL1J063045.9-603110:

a tidal disruption event fallen into the back burner

from *Mainetti, D., Campana, S. & Colpi, M., 2016, A&A, 592, A41*

Few years ago, tidal disruption candidates started to be reported in dwarf galaxies (Ghosh et al. 2006; Maksym et al. 2013; 2014a; 2014b; Donato et al. 2014), suggesting that an intermediate-mass BH (IMBH; $10^2\mathrm{M}_\odot \lesssim M_{\mathrm{BH}} \lesssim 10^6\mathrm{M}_\odot$) is located in their nuclei. The formation process of IMBHs is still an open question (e.g. Madau & Rees 2001; Miller & Hamilton 2002; Portegies Zwart & McMillan 2002; Begelman et al. 2006; Latif et al. 2013), but confirming their existence, detecting them, and obtaining a mass estimate are extremely important, as they could fill in the current gap in mass distribution between stellar-mass BHs and MBHs (Merloni & Heinz 2013) and also explain the origin of MBHs through mergers of small galaxies hosting IMBHs (e.g. Volonteri 2010). Tidal disruptions in dwarf galaxies are an opportunity for achieving all this.

In this chapter I discuss XMMSL1J063045.9-603110, a recently discovered bright soft X-ray source whose X-ray activity might be attributable to a tidal

disruption. I briefly summarise what is known about XMMSL1J063045.9-603110 in section 3.1. Then, I discuss the possible tidal disruption nature of the source in an extremely small galaxy, or even in a globular cluster, reducing (section 3.2) and exploring X-ray data from spectral analysis (section 3.3) to flux variability (section 3.4) and also investigate the activity of XMMSL1J063045.9-603110 at lower energies (section 3.5) and evaluate the probably host absolute magnitude (section 3.6). Results are summarised in section 3.7.

3.1 XMMSL1J063045.9-603110

On December 1, 2011, the new point-like source XMMSL1J063045.9-603110 (hereafter XMMSL1J063045) was detected to be bright in the X-ray sky probed by the *XMM-Newton* Slew Survey (Saxton et al. 2008), at RA(J2000)=06:30:45.9, DEC(J2000)=-60:31:10 ($8''$ error circle, 1σ confidence level). The source was soft, with essentially no emission above 2 keV. Fitting the Slew X-ray spectrum, Read et al. (2011a) estimated an absorption of $N_{\rm H} = 0.11 \times 10^{22}{\rm cm}^{-2}$ ($\sim 2.1 N_{\rm H_{Gal}}$), a black body temperature of $T_{\rm bb} = 85$ eV, and an absorbed 0.2-2 keV EPIC-PN flux of 4.0×10^{-11} erg s^{-1} cm^{-2}, starting from a count rate of 32.6 ct s^{-1}. When the same spectral model is assumed, the upper limits obtained from two previous *XMM-Newton* slews over this position, which are < 0.52 ct s^{-1} (14/08/2002) and < 1.76 ct s^{-1} (18/11/2008), give absorbed 0.2-2 keV EPIC-PN fluxes of $< 6.4 \times 10^{-13}$ erg s^{-1} cm^{-2} and $< 2.2 \times 10^{-12}$ erg s^{-1} cm^{-2}. These are factors of more than 63 and 18 below the bright Slew detection, respectively. This flux gap, together with the non-detection of previous lower energy counterparts (Figure 3.1, left panel), led Read et al. to suggest that XMMSL1J063045 might be a new nova.

On December 18, 2011, Kann et al. (2011) identified an object at RA(J2000)=

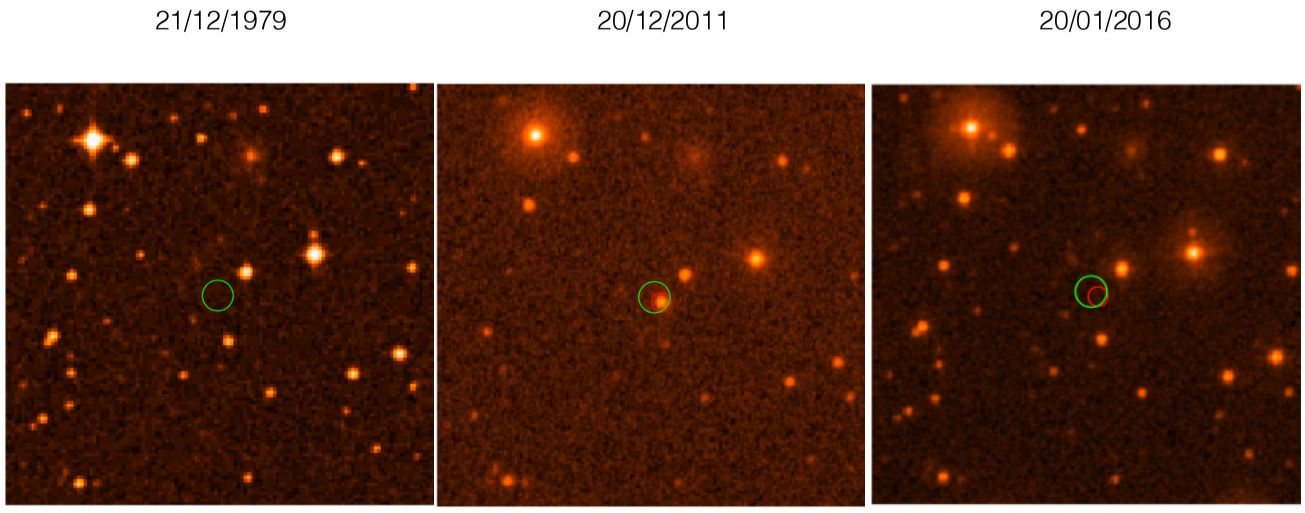

Figure 3.1: Left panel: Image from the DSS catalogue before the XMMSL1J063045 detection in X-rays. No counterparts are visible within the XMMSL1J063045 Slew error circle (green circle). Central panel: *Swift* UVOT *uvw1* filtered image immediately subsequent to XMMSL1J063045 detected X-ray ignition. A possible counterpart appears within the XMMSL1J063045 Slew error circle (green) and within $5''$ from the source UVOT position (red circle). Right panel: *Swift* UVOT *uvvv* filtered image, obtained about four years after the *uvw1* filtered observation. No counterparts are visible either within the XMMSL1J063045 Slew error circle (green circle) or within $5''$ from the source UVOT position (red circle). The images are $3.4' \times 3.4'$, north is up, east is left.

Table 3.1: XMMSL1J063045 counterpart AB magnitudes measured by Kann et al. (2011) from GROND observations.

Filter	*g'*	*r'*	*i'*	*z'*	*J*	*H*	*K*
m	18.4 ± 0.1	19.5 ± 0.1	19.6 ± 0.1	20.1 ± 0.1	20.3 ± 0.2	20.9 ± 0.4	> 20.0

06:30:45.45, DEC(J2000)=-60:31:12.8 with an error of $\pm 0.3''$, which is fully within the XMMSL1J063045 Slew error circle, based on simultaneous filtered observations of the XMMSL1J063045 field with the optical telescope GROND. The authors suggested it might be the counterpart of XMMSL1J063045. Table 3.1 summarises the AB magnitudes they measured with different filters. The faint brightness (the Galactic reddening at this position is only $E(B-V) = 0.07$; Schlegel et al. 1998), coupled with the very blue *g'-r'* colour evaluated by Kann et al., is atypical for a nova, which discards the classification suggested by Read et al. (2011a) and favours an accretion disc hypothesis. Fitting the source spectrum with a -2 power law, Kann et al. found a deviation in the *g'* band (4000-5400 Å), which they interpreted as due to a strong HeII emission ($\lambda_{\rm HeII} = 4685$ Å).

On December 20, 2011, the *Swift* satellite also revealed a soft X-ray source coincident with the object detected with GROND. To be specific, the *Swift*/UVOT *uvw1* (2000-3300 Å) source position is RA(J2000)=06:30:45.42, DEC(J2000)=-60:31:12.54 ($0.44''$ error circle, 90% confidence level). From fitting the XRT spectrum with $N_{\rm H} \equiv N_{\rm H_{Gal}} = 5.11 \times 10^{20} {\rm cm}^{-2}$, Read et al. (2011b) found a black body temperature of $T_{\rm bb} = 48 \pm 5$ eV and an absorbed 0.2-2 keV flux of $3.4^{+0.8}_{-1.2} \times 10^{-12}$ erg s^{-1} cm^{-2}, which is a factor of about 12 below the *XMM-Newton* Slew bright flux.

Despite the peculiar features of this source (soft X-ray thermal spectrum, black

Table 3.2: Log of all the XMMSL1J063045 X-ray observations. Pointed observations in italics have not previously been reported in the literature. The last *Swift* XRT observation in bold italics was required to check the current state of the source. *XMM-Newton* Slew (SL) count rates (0.2-2 keV) were adopted from Read et al. (2011a), *Swift* count rates (0.3-2 keV) from the online catalogue at the webpage http://www.swift.ac.uk/1SXPS/1SXPS%20J063045.2-603110, except for the last observation, whose upper limit on the count rate was evaluated using the XIMAGE task sosta. The *XMM-Newton* pointed observed count rate (0.2-2 keV) was extracted from the corresponding source spectrum. The 0.2-2 keV unabsorbed fluxes are estimated as reported in section 3.4.

Instrument	Obs. ID	Start time dd/mm/yy	Start time MJD	Exp. time s	Source count rate ct s^{-1}	0.2-2 keV Unabs. flux erg s^{-1} cm^{-2}
XMM-Newton (SL) EPIC-PN		14/08/2002	52500		< 0.52	$< (2.8 \pm 0.3) \times 10^{-12}$
XMM-Newton (SL) EPIC-PN		18/11/2008	54788		< 1.76	$< (9.5 \pm 0.9) \times 10^{-12}$
XMM-Newton (SL) EPIC-PN		01/12/2011	55896		32.6	$(1.7 \pm 0.2) \times 10^{-10}$
Swift XRT	00032225001	20/12/2011	55915	2.9×10^3	$(6.4 \pm 0.5) \times 10^{-2}$	$(1.2 \pm 0.2) \times 10^{-11}$
XMM-Newton EPIC-PN	*0679381201*	*22/12/2011*	*55917*	6.5×10^3	1.94 ± 0.02	$(8.7 \pm 0.9) \times 10^{-12}$
Swift XRT	*00032225002*	*06/01/2012*	*55932*	*471*	$2.5^{+0.9}_{-0.7} \times 10^{-2}$	$(4.6^{+1.9}_{-1.5}) \times 10^{-12}$
Swift XRT	*00032225003*	*11/01/2012*	*55937*	*579*	$1.6^{+0.7}_{-0.5} \times 10^{-2}$	$(2.9^{+1.4}_{-1.0}) \times 10^{-12}$
Swift XRT	*00032225004*	*12/01/2012*	*55938*	2.1×10^3	$8.0^{+2.4}_{-2.0} \times 10^{-3}$	$(1.5^{+0.5}_{-0.4}) \times 10^{-12}$
Swift XRT	***00032225005***	***20/01/2016***	***55917***	$\boldsymbol{4.3 \times 10^3}$	$\boldsymbol{< 2.4 \times 10^{-3}}$	$\boldsymbol{< (4.4^{+0.8}_{-0.7}) \times 10^{-13}}$

body temperature decrease, high and rapid X-ray flux decay, accretion-disc-like optical-UV spectrum), nothing else can be found in the literature.

Table 3.2 lists the whole of the XMMSL1J063045 X-ray observations, also including four observations that were not previously reported in the literature (in italics) and another that was specifically required to check the current state of the source (in bold italics). In the following sections I present the X-ray data analysis and discuss the possible nature of the source.

3.2 X-ray data reduction

3.2.1 *XMM-Newton Slew survey*

XMMSL observations were carried out with all the three imaging EPIC cameras (PN, MOS1, and MOS2) onboard *XMM-Newton*, but the high Slew speed and the slow readout time of MOS1 and MOS2 (Turner et al. 2001) prevent MOS data from being analysed. Therefore Read et al. (2011a) analysed only EPIC-PN data (Strüder et al. 2001) of XMMSL1J063045. XMMSL data are not available for public analysis, and for this reason I rely on the work done by Read et al. (section 3.1).

3.2.2 *Swift*

The composite XRT spectrum of XMMSL1J063045, obtained by grouping the four *Swift* XRT observations close in time listed in Table 3.2, can be directly downloaded from the online *Swift* source catalogue (Evans et al. 2014).[1] No emission above 2 keV is observed. Hence, the source count rates reported in Table 3.2 for each XRT observation can be approximately associated with the 0.3-2

[1] http://www.swift.ac.uk/1SXPS/spec.php?sourceID=1SXPS_J063045.2-603110

keV energy band. Spectral data were binned with the `grppha` tool of `HEASoft` (v.6.17) to a minimum of one photon per channel of energy, given the low number of photons, and Cash-statistics were adopted when fitting the data.

The last XRT observation reported in bold italics in Table 3.2 was reprocessed using `xrtpipeline` (v.0.13.2), and its corresponding upper limit on the source count rate was evaluated using the `XIMAGE` (v.4.5.1) task `sosta`.

3.2.3 *XMM-Newton*

The *XMM-Newton* pointed observation of XMMSL1J063045 (Table 3.2) was carried out with all the three *XMM-Newton* EPIC cameras using the thin filter. Data were reprocessed using `SAS` (v.13.5.0). They were filtered for periods of high background flaring activity, setting the maximum threshold on the source light curve count rates at 0.4 (0.35) ct s^{-1} for the PN (MOS) camera. Data were also filtered with the FLAG==0 option, and only events with pattern ≤ 4 (≤ 12) were retained. For all the three cameras, the source plus background spectrum was extracted from a circular region of radius $40''$, centred on the source. These spectra were cleaned from the background, extracted from a circular region of radius $40''$ on the same CCD, free of sources and bad columns. `RMF` and `ARF` files were produced using the appropriate tasks. The obtained source spectra were binned to a minimum of 20 photons per channel of energy. Data were accumulated in the 0.2-2 keV (0.3-2 keV) energy band for the PN (MOS) camera.

3.3 X-ray spectral analysis

From the *XMM-Newton* pointed observation of XMMSL1J063045 reported in Table 3.2 three distinct soft X-ray spectra were obtained, one for each EPIC camera

(section 3.2.3).[2] They were fitted together with an absorbed (using `TBABS`) power law model from the package `XSPEC` (v.12.9.0), tying together all the column densities and all the photon indexes. The photon index is extremely high, with $\Gamma = 9.8 \pm 0.2$ (all errors are determined at the 90% confidence level), and the column density $N_{\rm H} = (17.41 \pm 0.31) \times 10^{20} {\rm cm}^{-2}$ significantly exceeds the Galactic value $N_{\rm H_{Gal}} = 5.11 \times 10^{20} {\rm cm}^{-2}$. The obtained χ^2-statistics value is 359.7 with 200 degrees of freedom (d.o.f.) and the corresponding null hypothesis probability (nhp) 10^{-11}. An absorbed bremsstrahlung model provides significantly better results: $\chi^2 = 248.7$ with 200 d.o.f. and a corresponding nhp of 1.1%. Even better results are obtained with an absorbed thermal accretion disc (`diskbb`) model, which also unifies the thermal nature of the XMMSL1J063045 X-ray emission, as identified by Read et al. (2011a), and the accretion disc appearance inferred by Kann et al. (2011) from the source optical emission (section 3.1). This model, with column densities $N_{\rm H}$ and `diskbb` temperatures T tied together, gives $N_{\rm H} = 7.79^{+0.55}_{-0.53} \times 10^{20} {\rm cm}^{-2}$, somewhat in excess of the Galactic value, and $T = 59 \pm 1$ eV, returning a χ^2-statistics value of 237.5 with 200 d.o.f. and a corresponding nhp of 3.7% (Figure 3.2).

Given the low number of photons that appear in the *Swift* X-ray observations of XMMSL1J063045, the composite XRT spectrum of the source was fitted again with the `diskbb` model, fixing the column density to $N_{\rm H} = 7.79 \times 10^{20} {\rm cm}^{-2}$. This fit gives $T = 58^{+6}_{-5}$ eV, returning a χ^2-statistics value of 20.86 with 37 d.o.f., assessed using the Churazov-weighted χ^2-statistics (Churazov et al. 1996) applied to the best fit with Cash-statistics.

[2] *XMM-Newton* RGS data were also inspected, but no emission or absorption lines were found.

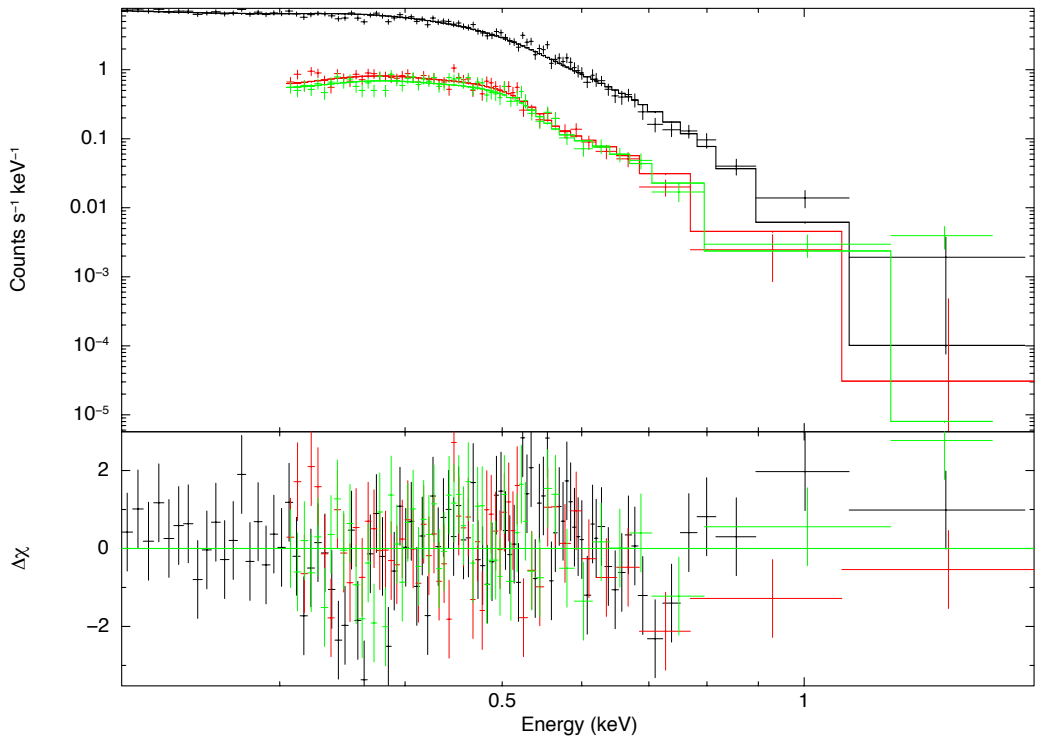

Figure 3.2: PN (black), MOS1 (red) and MOS2 (green) soft X-ray spectra obtained from the *XMM-Newton* pointed observation of XMMSL1J063045 reported in Table 3.2, fitted with an absorbed thermal accretion disc model, in agreement with Read et al. (2011a) and Kann et al. (2011; section 3.1). Residuals in terms of $\Delta\chi$ are plotted in the lower panel with corresponding colours and are well distributed throughout the concerned energy band.

3.4 X-ray flux variability

At this point, the XMMSL1J063045 (soft) X-ray emission was modelled. To do this, the count rates associated with the source X-ray observations were converted into unabsorbed fluxes (Table 3.2).

From the XMMSL observations, the 0.2-2 keV absorbed fluxes that result from the analysis of Read et al. (2011a; section 3.1) were considered. The conversion factor aimed at obtaining the corresponding 0.2-2 keV unabsorbed fluxes can be easily estimated based on the Read et al. best spectral fit of the more recent XMMSL data, setting $N_{\rm H} = 0$. By applying this correction factor to all the three XMMSL observations, the 0.2-2 keV unabsorbed fluxes reported in Table 3.2 were obtained. The assumed relative uncertainty on fluxes for XMMSL observations is 10%.

The 0.2-2 keV unabsorbed fluxes associated with *Swift* XRT count rates were computed by means of the conversion factor $(1.83^{+0.31}_{-0.27}) \times 10^{-10}$ erg $\rm s^{-1}$ $\rm cm^{-2}$ (ct $\rm s^{-1})^{-1}$ extracted from the unabsorbed thermal accretion disc spectral model applied to the composite XRT spectrum. In particular, the conversion factor obtained by summing four XRT observations was applied to each XRT observation, assuming the same spectral model also for the last observation in Table 3.2. Uncertainties on the unabsorbed fluxes result from error propagation. The same method was adopted to compute the 0.2-2 keV (EPIC-PN) unabsorbed flux corresponding to the source *XMM-Newton* pointed observation and its uncertainty. A relative systematic uncertainty of 10%, as for XMMSL fluxes, was also considered for all observations according to error propagation, thus justifying the comparison of data carried out with different satellites.

Figure 3.3 shows the XMMSL1J063045 X-ray flux light curve without the

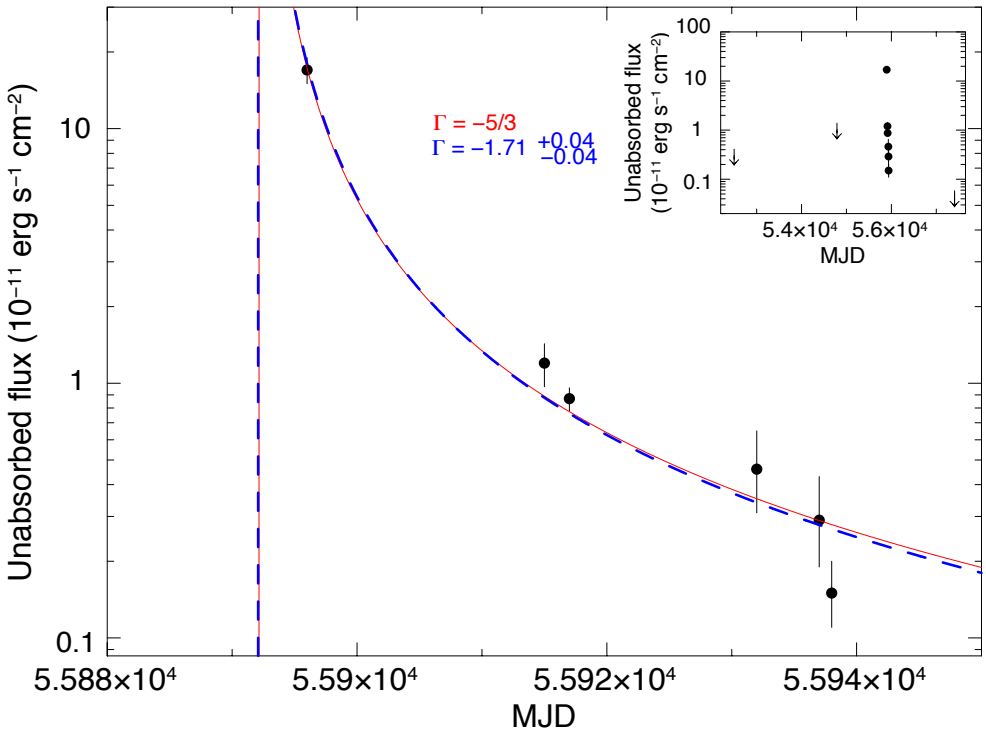

Figure 3.3: XMMSL1J063045 X-ray flux light curve fitted with a $-5/3$ power law (red solid line; $\chi^2_{\rm red} = 2.5$, $\rm nhp = 4.2\%$), as for tidal disruption events, and with a free power law (blue dashed line; $\chi^2_{\rm red} = 3.2$, $\rm nhp = 2.2\%$), which gives a decay index of -1.71 ± 0.04, fully in agreement with $-5/3$. The right top panel also includes the upper limits on flux.

XMMSL and XRT upper limits. The right top panel shows the light curve with these limits. The unabsorbed fluxes were fitted with a $(t_{\rm MJD} - t_0)^{-5/3}$ power law, typical of a tidal disruption event (section 1.4), with t_0 being a characteristic parameter (red solid line). The obtained χ^2 is 9.9 with 4 d.o.f. ($\chi^2_{\rm red} = 2.5$) and the corresponding nhp is 4.2%. A fit with a free power law index (blue dashed line) gives $\chi^2 = 9.6$ with 3 d.o.f. ($\chi^2_{\rm red} = 3.2$) and a corresponding nhp of 2.2%. Moreover, the power law index is -1.71 ± 0.04, fully in agreement with $-5/3$. The XRT upper limit is lower than the last fitted flux value, which means that the source is still quiescent in the X-ray band today.

In addition to the XMMSL1J063045 X-ray light curve, a downward trend in the temperatures derived from spectral analysis was found. In particular, the XMMSL source spectrum analysed by Read et al. (section 3.1; 01/12/2011) was simulated using the `fakeit` option from the package `XSPEC` and grouped to a minimum of 20 photons per channel of energy. Fitting it with an absorbed thermal accretion disc model (`TBABS*diskbb` from `XSPEC`), instead of a black body (Read et al. 2011a), a `diskbb` temperature of 97 eV was obtained. The following *Swift* composite spectrum (Dec. 2011/Jan. 2012) and *XMM-Newton* pointed observation (22/12/2011) show `diskbb` lower temperatures of 58^{+6}_{-5} eV and 59 ± 1 eV, respectively.

The soft X-ray thermal accretion disc emission of the source together with its temperature decrease and its high and rapid $t^{-5/3}$ flux decay (a factor of about 115 in only a month and a half) are all evidence of the probable tidal disruption nature of XMMSL1J063045.

Table 3.3: XMMSL1J063045 counterpart AB magnitudes assessed from *Swift* UVOT filtered observations carried out after the source ignition in X-rays. No corrections for Galactic extinction are applied.

Start time dd/mm/yy	20/12/2011	06/01/2012	11/01/2012	12/01/2012	20/01/2016
Filter	*uvw1*	*uvuu*	*uvw2*	*uvm2*	*uvvv*
m	18.77 ± 0.03	18.21 ± 0.04	19.17 ± 0.06	19.31 ± 0.05	> 20.07

3.5 *Swift* UVOT data

A further comment on XMMSL1J063045 concerns its activity at lower energies. The left panel of Figure 3.1 shows no lower energy counterparts of the source before it lights up in X-rays. *Swift* XRT observations reported in Table 3.2, subsequent to the source X-ray ignition, are all coupled with *Swift* UVOT observations, each one carried out using only one filter (*uvw1*, *uvuu*, *uvw2*, *uvm2*, and *uvvv*). The central panel of Figure 3.1 shows the XMMSL1J063045 *uvw1* filtered field and the lighting up of a probably lower energy counterpart of the source, immediately after its X-ray activity. The right panel of Figure 3.1 shows no lower energy counterparts of the source in its *uvvv* filtered field, about four years after the source detection in X-rays. Table 3.3 also collects the source counterpart AB magnitudes associated with the five differently filtered UVOT observations, assessed with the `uvotsource` tool of `HEASoft` without correcting for Galactic extinction. This clearly is a soft X-ray/ optical-UV transient.

3.6 XMMSL1J063045 host galaxy

The main factor in stellar tidal disruptions is the destroyer BH, whose mass $M_{\rm BH}$ can be approximately related to the source luminosity distance d through

$$M_{\rm BH} \sim \frac{4\pi d^2 F_{\rm peak}}{1.3 \times 10^{38} {\rm erg\ s^{-1}}} {\rm M_\odot}. \tag{3.1}$$

Here, $F_{\rm peak}$ is the unabsorbed peak bolometric flux associated with the tidal disruption event while $L_{\rm peak}$, the peak bolometric luminosity, is assumed to coincide with the BH Eddington luminosity $L_{\rm Edd} \sim 1.3 \times 10^{38} {\rm erg\ s^{-1}} (M_{\rm BH}/{\rm M_\odot})$. For XMMSL1J063045, $F_{\rm peak}$ can be inferred by fitting the simulated XMMSL spectrum (section 3.4) with the best spectral model of Read et al. (2011a) by setting $N_{\rm H} = 0$ and extrapolating data in the 0.01-10 keV energy band. The flux is 2.8×10^{-10} erg ${\rm s^{-1}\ cm^{-2}}$, so that

$$M_{\rm BH} \sim 2.5 \times 10^2 {\rm M_\odot} \Big(\frac{F_{\rm peak}}{2.8 \times 10^{-10} {\rm erg\ s^{-1}\ cm^{-2}}} \Big) \Big(\frac{d}{\rm Mpc} \Big)^2, \tag{3.2}$$

or

$$d \sim 0.06 {\rm Mpc} \Big(\frac{2.8 \times 10^{-10} {\rm erg\ s^{-1}\ cm^{-2}}}{F_{\rm peak}} \Big)^{1/2} \Big(\frac{M_{\rm BH}}{\rm M_\odot} \Big)^{1/2}. \tag{3.3}$$

For a BH of mass $10^6 {\rm M_\odot}$, Equation 3.3 gives $d \sim 60$ Mpc (redshift $z = 0.014$; $H_0 = 69.6$ km ${\rm s^{-1}\ Mpc^{-1}}$, $\Omega_{\rm m} = 0.286$), while imposing $M_{\rm BH} < 10^8 {\rm M_\odot}$, as for tidally disrupted solar-type stars (Equation 1.17), $d <$ 600 Mpc ($z < 0.13$). It has been here assumed that the peak bolometric luminosity of the source coincides with its Eddington limit. On one hand, I am aware that this limit can be exceeded by a factor of several, but on the other hand, it must be noted that the actual outburst peak is probably brighter than the value inferred from the bright Slew detection. Hence the Eddington limit represents an acceptable compromise between these two

competing instances.

The XMMSL1J063045 redshift and, consequently, luminosity distance (and $M_{\rm BH}$ from Equation 3.2) might be inferred from its host galaxy spectroscopy, provided that there is a host galaxy, which should be in the case of tidal disruptions. No signs of it can be found in the DSS image (Figure 3.1, left panel) or in the *Swift* UVOT *uvvv* filtered image (Figure 3.1, right panel). On January 9, 2016, a deep 300 s V-band ESO-NTT image of the field of XMMSL1J063045 was obtained. This was carried out with the EFOSC2 instrument. The observations were taken as part of the Public ESO Spectroscopic Survey of Transient Objects (PESSTO[3]), and details of data products and reductions can be found in Smartt et al. (2015). Calibrating it through the identification of four objects in the UVOT *uvvv* filtered image using the `uvotsource` tool of `HEASoft` and the `GAIA` software (v.4.4.1), an object of apparent V magnitude $m_V \sim 23.26 \pm 0.27$ was found at the UVOT position of XMMSL1J063045 (Figure 3.4, green circle). This probably is the XMMSL1J063045 (dim) host galaxy. Currently, the dimmest (and smallest) galaxy associated with a tidal disruption is WINGS J134849.88+263557.7 in Abell 1795 (Maksym et al. 2013; 2014b; Donato et al. 2014). It is a faint ($m_V = 22.46$) dwarf ($r \sim 300$ pc) galaxy lying at the same redshift of the cluster ($z = 0.062$; $M_V \sim -14.8$), possibly hosting an IMBH ($M_{\rm BH} = (2-5) \times 10^5 {\rm M}_\odot$). The problem for XMMSL1J063045 is that no spectra of its dim host galaxy are currently available in which absorption lines might be identified to evaluate z.

Using Equation 3.3 to estimate the source luminosity distance $d_{\rm pc}$ (in parsec) from a BH of mass $10^4 - 10^6 {\rm M}_\odot$ and considering the relation between the absolute

[3] www.pessto.org

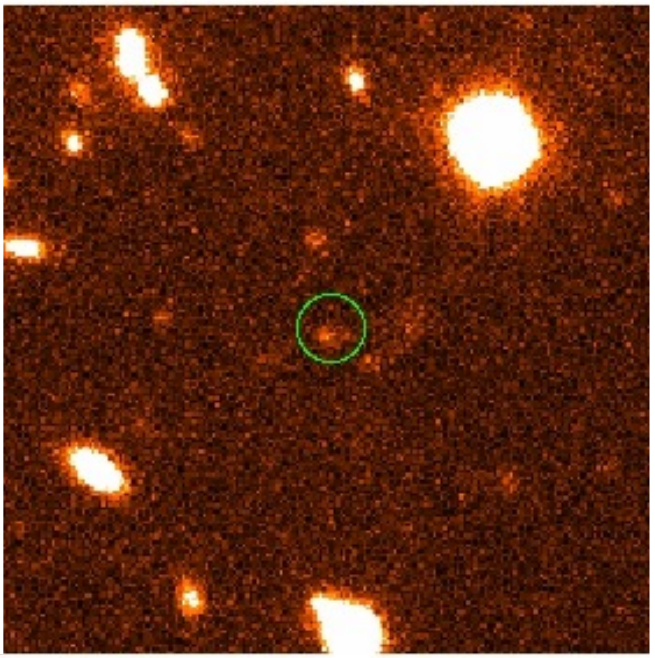

Figure 3.4: Zoom of a reduced 300 s ESO-NTT EFOSC2 recent image of the XMMSL1J063045 field in the *V* filter (09/01/2016, about four years after XMMSL1J063045 X-ray detection). The image is $0.9' \times 0.9'$, north is up, east is left. A dim extended source, possibly the XMMSL1J063045 host galaxy, is visible within $2.5''$ from XMMSL1J063045 UVOT position (green circle).

magnitude (M_V) and the apparent magnitude (m_V)

$$M_V = m_V + 5 - 5 \log d_{\rm pc}, \tag{3.4}$$

the dim host ends up with $M_V \sim -5.7 \div -10.7$. When $L_{\rm peak}$ is assumed to be ten times the Eddington luminosity (which is very high), M_V lies in the range $-8.2 \div -13.2$. This value is at the level of the faintest dwarf spheroidal galaxies in our Milky Way (Sculptor has $M_V = -10.7$) or of the brightest globular clusters (NGC 5139 has $M_V = -10.2$), opening the possibility of observing the first tidal disruption in a globular cluster and suggesting that IMBHs are present in the cores of at least some of them.

3.7 Summary and main conclusions

Up to now, a very limited number of tidal disruption candidates have been observationally identified in dwarf galaxies, which possibly host IMBHs at their centres (Ghosh et al. 2006; Maksym et al. 2013; 2014a; 2014b; Donato et al. 2014). The discovery of new tidal disruption candidates in dwarf galaxies thus might allow the determination of plausible destroyer IMBHs. This class of BHs is currently under study (e.g. Ptak & Griffiths 1999; Davis & Mushotzky 2004; Wolter et al. 2006; Greene & Ho 2007; Farrell et al. 2009; Irwin et al. 2010; Jonker et al. 2010; 2013; Krolik & Piran 2011) as the connecting bridge between stellar-mass BHs and MBHs and the raw material that makes up MBHs (e.g. Volonteri 2010).

On December 1, 2011, the new point-like source XMMSL1J063045 was detected to be bright in the soft X-rays, with an underlying thermal emission (Read et al. 2011a). An accretion-disc nature was suggested (Kann et al. 2011). After about twenty days, XMMSL1J063045 was also observed by the *Swift* satellite,

again producing a soft X-ray thermal emission, a factor of about 10 below its first detection (Read et al. 2011b). I reported here a comprehensive data analysis of all the available X-ray (Table 3.2) and lower energy data (section 3.5) of XMMSL1J063045. The source is suggested to be a tidal disruption event. It showed an accretion-disc-like thermal spectrum in the soft X-rays (Figure 3.2) together with a high and rapid flux decay (a factor of ~ 115 in only a month and a half) that is well modelled by a power law of index $-5/3$ (Figure 3.3). Moreover, the source also blazed up at lower energies (Figure 3.1), even if it slightly lags behind the X-ray flaring.

The hypothesis that XMMSL1J063045 is a Galactic nova (Galactic latitude $b = -26$) is rejected. The softness of the source X-ray spectrum would require such a nova to be in a super-soft state. To reach this state, the source would need to radiate at Eddington ($\sim 1.3 \times 10^{38}\mathrm{erg\ s^{-1}}$) and would have to lie at

$$d \sim \sqrt{\frac{L_{\mathrm{peak}}}{4\pi F_{\mathrm{peak}}}} \sim \sqrt{\frac{1.3 \times 10^{38}\mathrm{erg\ s^{-1}}}{4\pi\ 2.8 \times 10^{-10}\mathrm{erg\ s^{-1}\ cm^{-2}}}} \sim 62\mathrm{kpc}, \qquad (3.5)$$

which is a too large distance for it to be a Galactic nova. Furthermore, the source magnitude variation is about 5 mag, which is too small for a typical nova, and its quiescent magnitude (section 3.6) is too high for a typical super-soft nova (the dimmest one, GQ Mus, has a quiescent V magnitude of ~ 18; e.g. Warner 2002). The reported magnitudes are not enhanced by Galactic extinction, given that this is very low at the source position (Schlegel et al. 1998). Also, the idea that XMMSL1J063045 is an AGN is discarded, because it would have been detected in all the observations if that were the case (see also the discussion in Campana et al. 2015).

Based on the hypothesis that XMMSL1J063045 is a candidate tidal disruption

event, the low `diskbb` temperature that characterises the source ($T \sim 100$ eV $\sim 10^6$ K; section 3.4) would call for a $\sim 10^5 \mathrm{M}_\odot$ destroyer BH, assuming that it accretes at one ÷ ten times the Eddington rate and that the emission radius is at some $r_\mathrm{g} = GM_\mathrm{BH}/c^2$. It might be a tidal disruption event in a very dim dwarf galaxy or even in a very bright globular cluster ($M_V \sim -10$), which then could host a BH at their centre. Globular clusters typically do not wander alone in the cosmos, but are associated with a parent galaxy. Figure 3.4 shows that the field of XMMSL1J063045 is sparsely crowded, but there is something around it, possibly also a parent galaxy. Spectroscopic observations of XMMSL1J063045 host will provide a clearer answer.

Chapter 4

The fine line between total and partial tidal disruption events

from *Mainetti, D., Lupi, A., Campana, S., Colpi, M., Coughlin, E. R., Guillochon, J. & Ramirez-Ruiz, E., 2017, A&A, 600, A124*

As already said, a star located in the nuclear star cluster of a galaxy can be scattered closer to the central BH by dynamical mechanisms. Sometimes the BH tidal influence on the star is strong enough to completely disrupt it, but other times a stellar remnant succeeds in surviving the encounter. This depends on whether or not the star crosses a critical distance from the BH. Usually, such a critical distance is assumed to be the BH tidal radius $r_{\rm t}$ (Equation 1.1), meaning that a star approaching the central BH of a galaxy on an orbit with $r_{\rm p} < r_{\rm t}$ ($\beta > 1$, Equation 1.10) undergoes total tidal disruption, while if $r_{\rm p} > r_{\rm t}$ ($\beta < 1$) the star is only partially disrupted. The main problem with this assumption is that $r_{\rm t}$ defines where the BH tidal force overcomes the stellar self-gravity only at the stellar surface, and not everywhere within the star (e.g. Lacy et al. 1982). This is therefore about finding the distance from the BH where even the star's densest regions are ripped

apart.

In this chapter, I deal with the computation of such a distance, $r_{\rm d}$, through the definition of the critical disruption parameter

$$\beta_{\rm d} = \frac{r_{\rm t}}{r_{\rm d}} = \beta \frac{r_{\rm p}}{r_{\rm d}}, \tag{4.1}$$

where Equation 1.10 is used (Guillochon & Ramirez-Ruiz 2013; 2015a). A partial tidal disruption is obtained for $\beta < \beta_{\rm d}$, that is, for $r_{\rm p} > r_{\rm d}$, a total tidal disruption for $\beta \geq \beta_{\rm d}$, that is, for $r_{\rm p} \leq r_{\rm d}$. Guillochon & Ramirez-Ruiz (2013; 2015a; hereafter GRR) evaluated $\beta_{\rm d}$ for stellar polytropes of index $5/3$ and $4/3$ (which represent low- and high-mass stars, respectively) using a series of adaptive mesh refinement (AMR) grid-based hydrodynamical simulations of star-BH Newtonian parabolic tidal encounters. Here, instead, I present the results of simulations performed for the same purpose with the GADGET2 (traditional smoothed particle hydrodynamics (SPH); Springel 2005)[1] and GIZMO (modern SPH and mesh-free finite mass (MFM); Hopkins 2015)[2] codes. Since these techniques all have advantages but also limits, my coauthors and I were inclined to follow GRR in finding the critical disruption parameter $\beta_{\rm d}$ for certain stellar structures[3] using an MFM, a traditional SPH and a modern SPH code instead of an AMR grid-based code, with the goal of comparing results from different techniques.

The chapter is organised as follows. In section 4.1 I compare AMR grid-based codes to GIZMO MFM, traditional SPH and modern SPH techniques. In section 4.2

[1] http://wwwmpa.mpa-garching.mpg.de/gadget/

[2] http://www.tapir.caltech.edu/∼phopkins/Site/GIZMO.html

[3] When a more realistic stellar equation of state is used (e.g. Rosswog et al. 2009, but only for white dwarfs), the value of $\beta_{\rm d}$ may change slightly.

I discuss our method and describe the evaluation of the stellar mass loss ΔM in our simulated encounters. I show the curves of mass loss obtained for all codes as a function of β and polytropic index, comparing them and the corresponding $\beta_{\rm d}$ with GRR. Section 5.5 summarises the results.

4.1 Grid-based vs. SPH and GIZMO MFM codes

Fluid hydrodynamics and interactions in astrophysics are generally treated using two different classes of numerical methods: Eulerian grid-based (e.g. Laney 1998; Leveque 1998) and Lagrangian SPH (e.g. Monaghan 1992; Price 2005; 2012; Cossins 2010). Basically, grid-based methods divide a domain into stationary cells traversed over time by the investigated fluid and evaluate the evolution of the fluid properties at a fixed position as the fluid passes. It's like sitting on a river bank and watching different water elements pass a fixed location over time. In particular, AMR grid-based techniques (e.g. Berger & Oliger 1984; Berger & Colella 1989) adapt the cell number and size according to the properties of different fluid regions, thus increasing the resolution where needed (for example in correspondence of high-density regions) and reducing computational efforts and memory employment where lower resolution is sufficient. In contrast, SPH methods are Lagrangian by construction and model a fluid as a set of fluid elements, or particles, each followed with its own set of evolving fluid properties (it's like sitting in a boat and drifting down a river). In practice, the density of each particle is calculated by considering a defined number of neighbours, within its so-called smoothing length, and weighting their contribution according to a smoothing kernel function (e.g. Price 2005), and particle velocities and entropies or internal energies are evolved according to a pressure-entropy or energy formalism (modern SPH) or a density-entropy or energy

formalism (traditional SPH). Essentially, modern SPH techniques evaluate the pressure and the local density of each particle by considering the neighbours within the particle smoothing length and use pressure to define the equations of motion (Hopkins 2013). Traditional SPH techniques, instead, directly estimate the pressure of each particle from its local density and use local density to define the equations of motion. In SPH methods the particle density mirrors the density of different regions of the fluid.

Grid-based and SPH techniques both have advantages, but also limits. At sufficiently high velocities, grid-based methods are non-invariant under Galilean transformations, which means that different reference frames are associated with different levels of numerical diffusion among adjacent cells and simulation results may depend on the choice of the reference system (e.g. Wadsley et al. 2008). Moreover, grid-based methods violate angular momentum conservation because a fluid moving across grid cells produces artificial diffusion; this diffusion can lead to unphysical forces, which couple with the fixed structure of the grid to tie the fluid motion on specific directions (e.g. Peery & Imlay 1988; Hahn et al. 2010). Finally, in grid-based methods hydrodynamics and gravity descriptions are mismatched, in the sense that hydrodynamics is evaluated by integrating quantities over each cell, while gravity comes from a continuum but is associated to the centre of each cell. This can produce spurious instabilities (e.g. Truelove et al. 1997).

SPH methods first need an artificial viscosity term added to the particle equation of motion in order to resolve shocks (Balsara 1989; Cullen & Dehnen 2010). Second, because of how particle pressure is defined, traditional SPH codes are associated with a spurious surface tension between fluid regions of highly different densities, which limits their mixing (e.g. Agertz et al. 2007). Great effort has been

made to improve SPH methods, leading to the so-called modern SPHs (Hopkins 2013). The smoothed definition of pressures together with densities, the more sophisticated viscosity switches, the higher order smoothing kernels (quintic spline instead of cubic spline; see below) and the inclusion of artificial heat conduction allowed solving these problems, at least partially. However, the higher order kernels typically lead to excessive diffusion. Despite all these improvements, some intrinsic limits of this technique still remain, such as the ideal infinite number of neighbours required to capture small-amplitude instabilities.

Recently, a completely new Lagrangian method that aims at simultaneously capturing the advantages of both SPH and grid-based techniques has been implemented in the public code GIZMO (Hopkins 2015). In GIZMO, the whole volume is discretised among a discrete set of tracers (particles) through a partition scheme based on a smoothing kernel. However, unlike SPH codes, the particles do not sample fluid elements, but only represent the centre of unstructured cells that are free to move with the fluid, like in moving mesh codes (Springel 2010). Hydrodynamics is then solved like in grid-based codes, enabling this code to perfectly resolve shocks without the addition of an artificial viscosity. The density associated with each particle/cell is obtained by dividing the mass of the cell for its effective volume. Despite the great advantages of the new method implemented in the code, its limitations are still not clear. In this work, the mesh-free finite mass method of GIZMO is used, where the particle/cell mass is preserved, making the code perfectly Lagrangian. For this method, the cubic spline kernel with a desired number of neighbours equal to 32 is used for the partition.

4.2 SPH and GIZMO MFM simulations and stellar mass losses

Stars are modelled as polytropes of index $5/3$ (low-mass stars) or $4/3$ (high-mass stars), with masses and radii of $1\mathrm{M}_\odot$ and $1\mathrm{R}_\odot$, each sampled with $N_{\mathrm{part}} \sim 10^5$ particles. This was done by placing the particles through a close sphere packing and then stretching their radial positions to reach the required polytropic density profile, thus limiting the statistical noise associated with a random placement of the particles. N_{part} sets the gravitational softening length of each particle in the codes to $\epsilon \sim 0.1 R_*/(N_{\mathrm{part}})^{1/3} \sim 0.002\mathrm{R}_\odot$, preventing particle overlapping in evaluating gravitational interactions. Gravitational interactions between particles in GADGET2 and GIZMO codes are computed through a hierarchical oct-tree algorithm (e.g. Springel 2005), which significantly reduces the number of interactions needed to be computed. Test runs at higher resolution were also tried, where stars were modelled with $\sim 10^6$ particles, but no significant differences in the stellar mass loss ΔM were found with respect to simulations with lower resolution. Stars were evolved in isolation for several dynamical times in order to ensure their stability. The right panel of Figure 4.1 shows the relaxed stellar density profile, that is, the local density of the particles $\rho(r)$ (in $\mathrm{M}_\odot/\mathrm{R}_\odot^3$) versus their radial distance from the stellar centre of mass r (in $\mathrm{R}_\odot$), for each simulation technique for the two polytropic indexes ($\gamma = 4/3$ and $\gamma = 5/3$ from the highest to the lowest central density), compared to the numerical solutions from the Lane-Emden equation (left panel). The kernel function that drives the evaluation of each particle local density (e.g. Price 2005) and the volume partition (Hopkins 2015) was chosen to be a cubic (in GADGET2 and GIZMO MFM) or quintic (in GIZMO modern SPH) spline, and

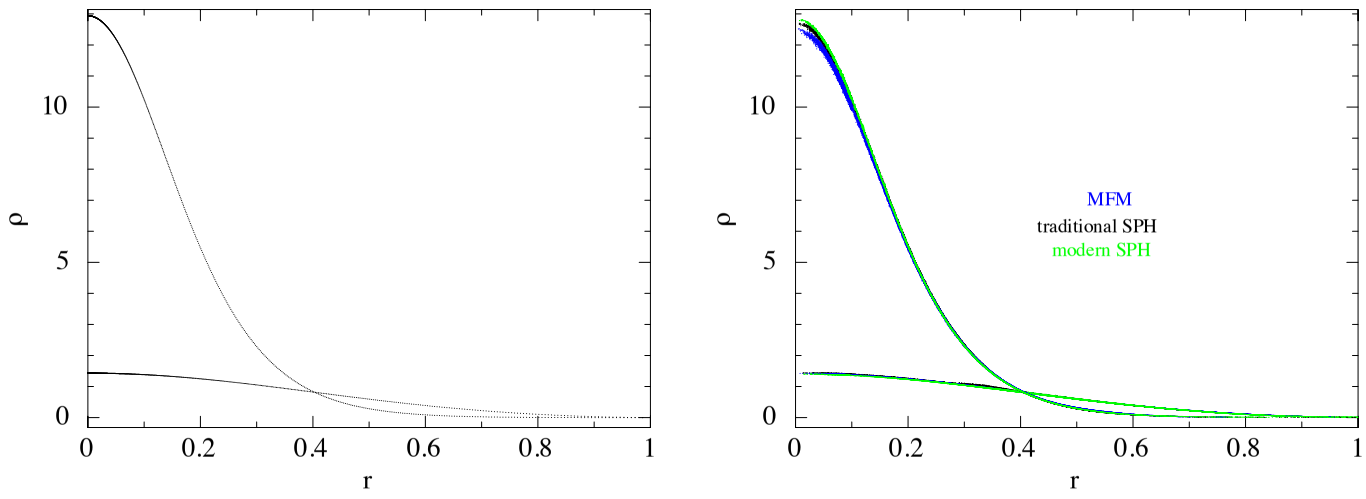

Figure 4.1: Left panel: Numerical solutions for the $\gamma = 4/3, 5/3$ polytropic radial density profile from the Lane-Emden equation. Right panel: Plot of the relaxed radial stellar density profile for each simulation technique for both polytropic indexes ($\gamma = 4/3, 5/3$ from the highest to the lowest central density). Units are $\mathrm{M}_\odot/\mathrm{R}_\odot^3$ for ρ and $\mathrm{R}_\odot$ for r.

the number of neighbours of each particle and domain point within its smoothing length/kernel size was fixed to 32 and 128, respectively (Monaghan & Lattanzio 1985; Hongbin & Xin 2005; Dehnen & Aly 2012). Gravitational forces were computed through the Springel relative criterion (Springel 2005) instead of the standard Barnes-Hut criterion (Barnes & Hut 1986), because the Springel criterion shows better accuracy at the same computational cost. Since the relative criterion is based on the particle acceleration, which is not available at the beginning of each simulation, the Barnes-Hut criterion is adopted at the first time step to estimate an acceleration value, and then the iteration is repeated using the Springel criterion in order to remain consistent with the subsequent iterations. In the simulations, quite a large opening angle value in the oct-tree algorithm was used (0.7), but the accuracy parameter for the relative criterion was set to 0.0005, which is very small compared to the suggested standard value (0.0025). Test runs were performed setting the opening angle to 0.1 and increasing the accuracy parameter to 0.0025, but no differences were found in the stellar density and temperature profiles and in ΔM. The BH force was implemented through a Newtonian analytical potential, with $M_{\rm BH} = 10^6 {\rm M}_\odot$, and in each of the traditional SPH, modern SPH and GIZMO MFM simulations a star was placed on a parabolic orbit with a given $r_{\rm p}$, that is, β, around the BH. The star was initially placed at a distance five times greater than $r_{\rm t}$ to avoid spurious tidal distortions (larger initial distances were also tested, but no significant differences were found in the outcomes). Stellar rotation is not expected to significantly affect the results in the range of β considered here (Stone et al. 2013). Figures 4.2 and 4.3 show snapshots from traditional SPH simulations recorded shortly after pericentre passage. The lower limit of the range where $\beta_{\rm d}$ lies (yellow) allows the core recollapse to occur for both polytropic indexes (Guillochon

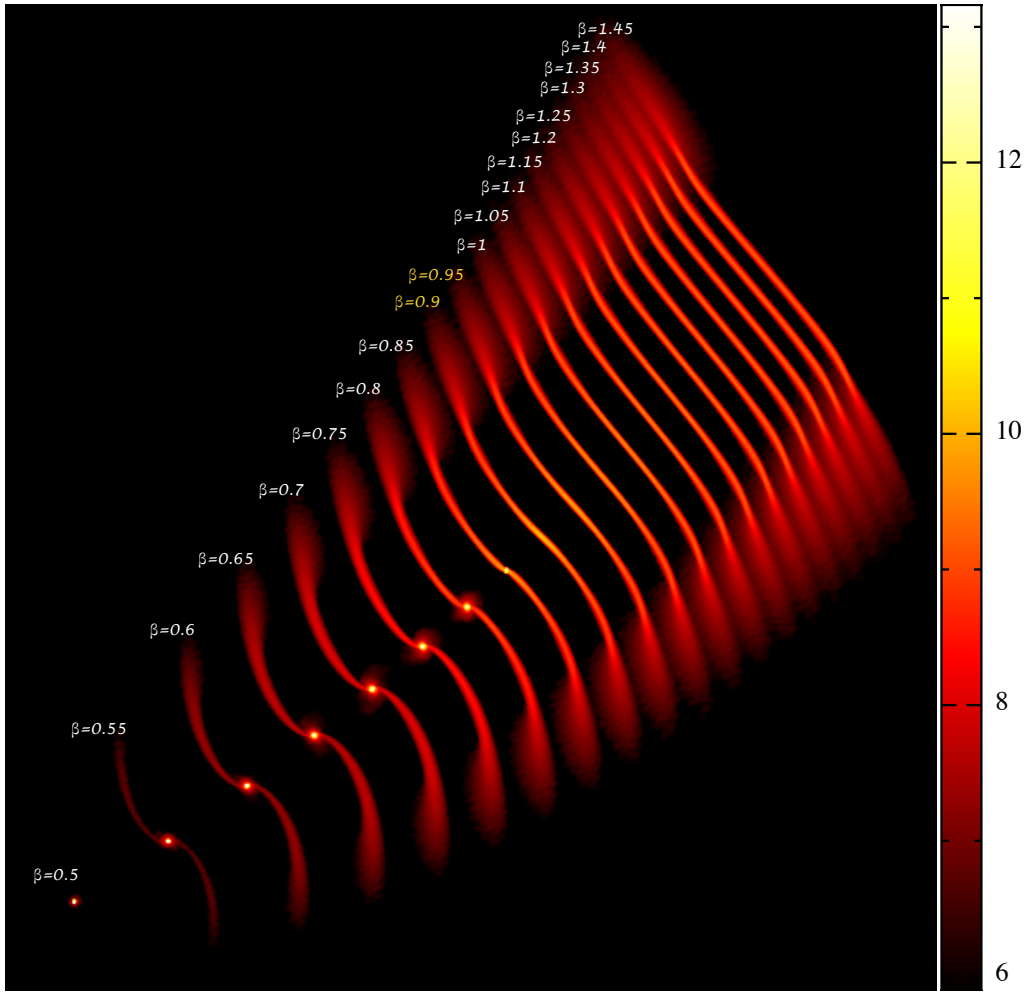

Figure 4.2: Snapshots of the SPH particle density (in logarithmic scale) at $t \sim 8.5 \times 10^4$s after pericentre passage for GADGET2 simulations, in the case of a star with polytropic index $5/3$. White and black correspond to the highest and lowest densities, respectively. Each snapshot is labelled with the corresponding value of β, with the range where the critical disruption parameter $\beta_{\rm d}$ lies highlighted in yellow.

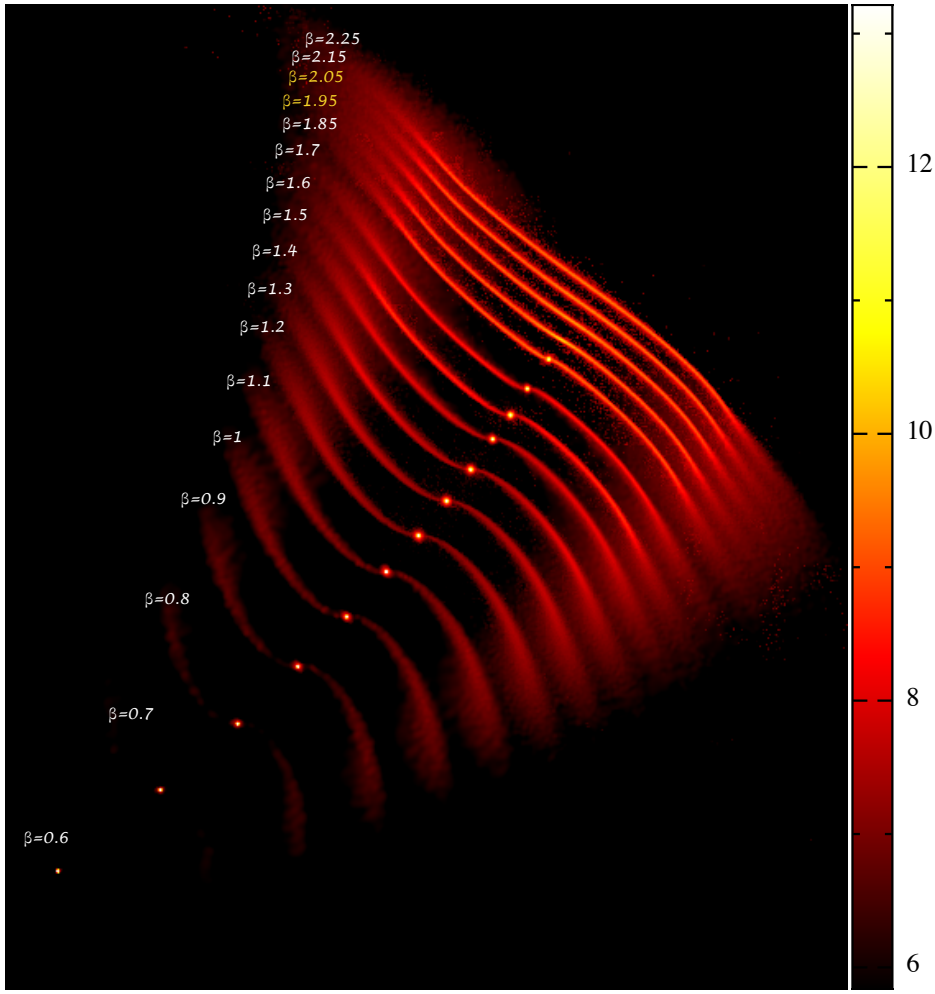

Figure 4.3: Same as Figure 4.2 for a polytropic star of index $4/3$.

& Ramirez-Ruiz 2013; 2015a). Modern SPH and GIZMO MFM simulations gave almost the same results.

The first goal here is to assess the stellar mass loss ΔM in each GADGET2 and GIZMO simulation. I recall that $\Delta M = M_*$ corresponds to total disruption. I describe the method adopted to evaluate ΔM from each of the simulated star-BH tidal encounters, following GRR. In a specific simulation at a specific time, the position and velocity components of the stellar centre of mass around the BH, $x_{\rm CM}$, $y_{\rm CM}$, $z_{\rm CM}$, $v_{\rm x_{CM}}$, $v_{\rm y_{CM}}$ and $v_{\rm z_{CM}}$, are defined through an iterative approach. As a first step, they are chosen to coincide with the position and velocity components of the particle with the highest local density, $x_{\rm peak}$, $y_{\rm peak}$, $z_{\rm peak}$, $v_{\rm x_{peak}}$, $v_{\rm y_{peak}}$, $v_{\rm z_{peak}}$. The specific binding energy to the star of the ith particle then reads

$$\epsilon_{*_i} = \frac{1}{2}\Big[(v_{\rm x_i} - v_{\rm x_{peak}})^2 + (v_{\rm y_i} - v_{\rm y_{peak}})^2 + (v_{\rm z_i} - v_{\rm z_{peak}})^2\Big] + \phi_{*_i}, \qquad (4.2)$$

where $v_{\rm x_i}$, $v_{\rm y_i}$ and $v_{\rm z_i}$ are the velocity components of the ith particle and ϕ_{*_i} the stellar gravitational potential acting on the ith particle (directly computed by the simulation code). By considering only particles with $\epsilon_{*_i} < 0$, the position and velocity components of the star centre of mass are re-defined and Equation 5.13 is re-evaluated by setting them in place of the components labelled with the subscript "peak". The process is re-iterated until the convergency of $v_{\rm CM}$ to a constant value to lower than $10^{-5}{\rm R}_\odot{\rm yr}^{-1}$. Particles with $\epsilon_{*_i} > 0$ are unbound from the star. The stellar mass loss at the considered time can be obtained by multiplying the mass of a single particle, $m = M_*/N_{\rm part}$, by the number of particles bound to the star, $N_{\rm bound}$, and subtracting the result from M_*. ΔM is obtained at $t \sim 10^6{\rm s}$, (~ 650 stellar dynamical times) after the disruption.

Figures 4.4 and 4.5 show the stellar mass loss in units of $\Delta M/M_*$ as a function

of β for polytropes of index $5/3$ and $4/3$, respectively, inferred from simulations with GIZMO MFM (blue points), GADGET2 (black points) and GIZMO modern SPH (green points), and the same obtained from the GRR simulations (red points). The

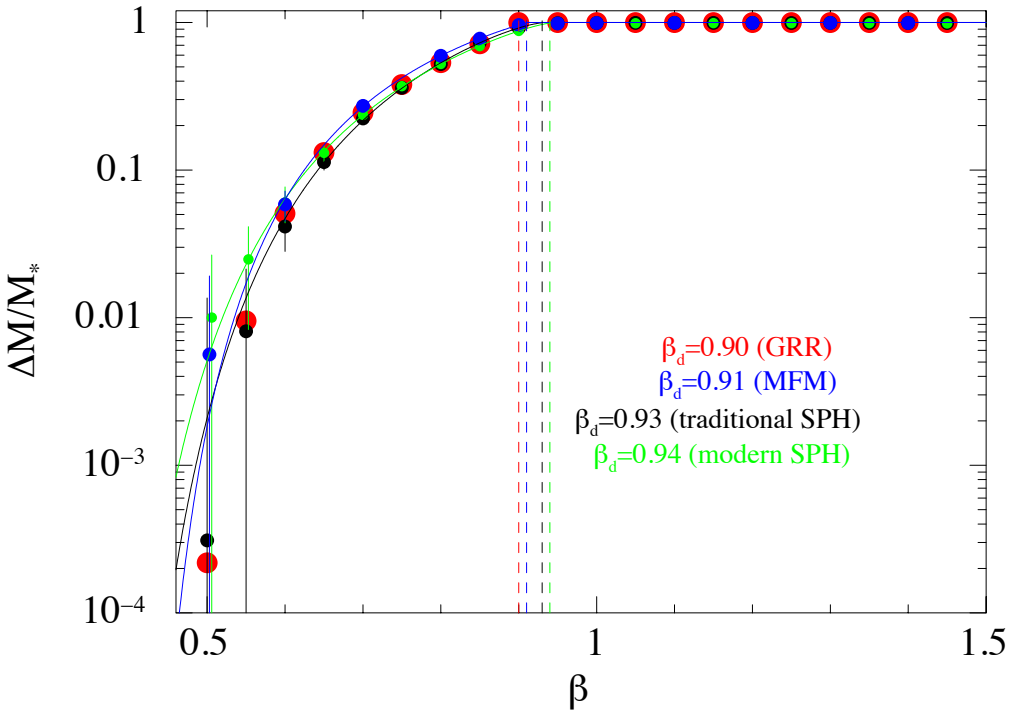

Figure 4.4: Stellar mass loss (in units of $\Delta M/M_*$) as a function of β for a star with polytropic index $5/3$. ΔM is evaluated at $t \sim 10^6$s after the disruption. Blue, black, green and red points are associated with GIZMO MFM, GADGET2, GIZMO modern SPH and GRR simulations, respectively. Uncertainties on $\Delta M/M_*$ from SPH and GIZMO MFM simulations were inferred as reported in the main text. Points at low values of β have been slightly horizontally displaced to give a better view of the error bars. The value of the critical disruption parameter $\beta_{\rm d}$ (dashed lines) slightly depends on the adopted simulation method.

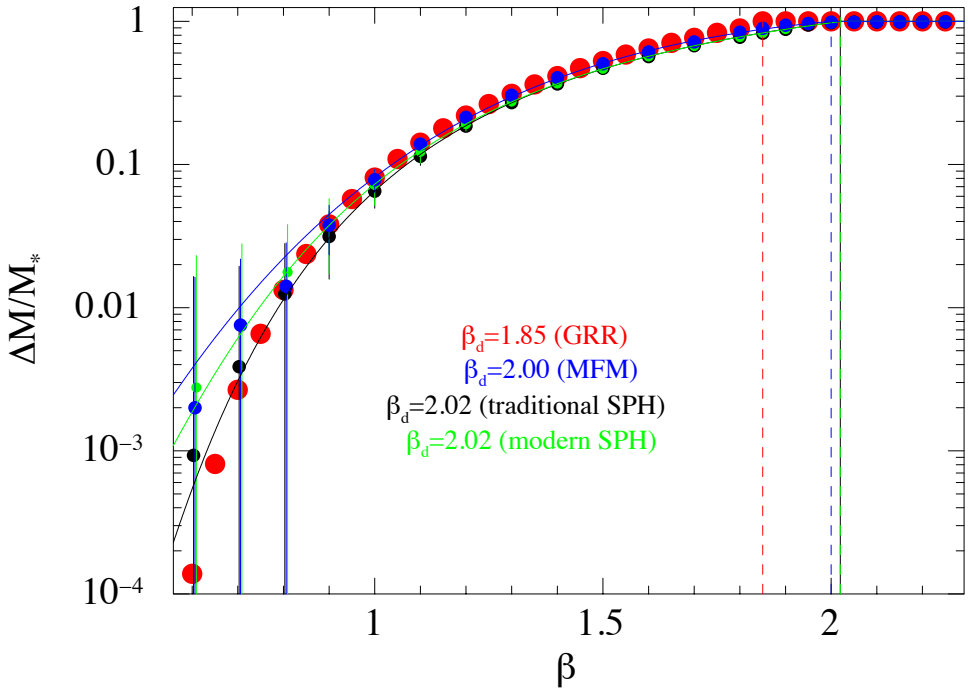

Figure 4.5: Same as Figure 4.4 for a polytropic star of index $4/3$. The values of β_d obtained from the here discussed simulations visibly differ from those of GRR.

uncertainty on $\Delta M/M_*$ as inferred from GADGET2 and GIZMO simulations was estimated to be

$$\sigma_{\frac{\Delta M}{M_*}} = \sqrt{\sigma^2_{\mathrm{Poisson}} + \sigma^2_{\epsilon_{*_i}} + \sigma^2_{\mathrm{AD}}} = \sqrt{\left(\frac{\sqrt{N_{\mathrm{bound}}}}{N_{\mathrm{part}}}\right)^2 + 0.01^2 + \sigma^2_{\mathrm{AD}}}, \tag{4.3}$$

where σ_{AD} is the average deviation from 1 of $\Delta M/M_*$ for total disruptions in each of the point sets and $\sigma_{\epsilon_{*_i}} = 0.01$, as the values of $|\epsilon_{*_i}|$ for about 10^3 particles of 10^5 are lower than 0.01 times the average value $\overline{|E_*|}$, that is, it is not possible to determine exactly whether these 10^3 particles are bound to or unbound from the

Table 4.1: Fitting coefficients of Equation 4.4 and $\beta_{\rm d}$ for each of the point sets in Figures 4.4 and 4.5.

Simulations	Polytropic index	*A*	*B*	*C*	*D*	*E*	$\beta_{\rm d}$
GRR	5/3	3.1647	-6.3777	3.1797	-3.4137	2.4616	0.90
GIZMO MFM	5/3	5.4722	-11.764	6.3204	-3.8172	2.8919	0.91
GADGET2	5/3	8.9696	-19.111	10.180	-4.2964	3.3231	0.93
GIZMO modern SPH	5/3	8.7074	-18.358	9.6760	-4.5340	3.5914	0.94
GRR	4/3	12.996	-31.149	12.865	-5.3232	6.4262	1.85
GIZMO MFM	4/3	-13.964	11.217	-2.1168	0.3930	0.5475	2.00
GADGET2	4/3	-15.378	-5.2385	6.3635	-1.5122	5.7378	2.02
GIZMO modern SPH	4/3	-10.394	-0.2160	2.6421	-0.8804	2.9215	2.02

star. Each GADGET2 and GIZMO point set was fitted with a function introduced in GRR

$$f(\beta) = \exp\left[\frac{A + B\beta + C\beta^2}{1 + D\beta + E\beta^2}\right], \qquad \beta < \beta_{\rm d}$$
$$f(\beta) = 1, \qquad \beta \geq \beta_{\rm d}. \tag{4.4}$$

The values of the coefficients $A \div E$ and of $\beta_{\rm d}$ are given in Table 4.1. It is worth noting that for the $5/3$ polytropic index the curves of stellar mass loss associated with the four simulation codes differ very slightly in the value of the critical disruption parameter $\beta_{\rm d}$ (dashed lines in Figure 4.4). Specifically, $\beta_{\rm d}$ is reached first in the GRR simulations ($\beta_{\rm d} = 0.90$), followed by the GIZMO MFM ($\beta_{\rm d} = 0.91$), GADGET2 ($\beta_{\rm d} = 0.93$) and GIZMO modern SPH ($\beta_{\rm d} = 0.94$) simulations (Table 4.2). This is expected because of the greater degree of excessive diffusion that characterises grid-based techniques compared to modern and traditional SPH techniques and the surface tension conversely involved in SPH methods (section 4.1). For the $4/3$ polytropic index, instead, there is disagreement between GADGET2 and GIZMO simulations and GRR simulations (dashed lines in Figure 4.5). $\beta_{\rm d}$ is

Table 4.2: $\beta_{\rm d}$ value as a function of polytropic index and adopted simulation method.

Simulation method	Polytropic index	$\beta_{\rm d}$
AMR grid-based	5/3	0.90
MFM	5/3	0.91
Traditional SPH	5/3	0.93
Modern SPH	5/3	0.94
AMR grid-based	4/3	1.85
MFM	4/3	2.00
Traditional SPH	4/3	2.02
Modern SPH	4/3	2.02

reached clearly first in the simulations of GRR ($\beta_{\rm d} = 1.85$), followed by very similar values of the GIZMO MFM ($\beta_{\rm d} = 2.00$), GADGET2 ($\beta_{\rm d} = 2.02$) and GIZMO modern SPH ($\beta_{\rm d} = 2.02$) simulations (Table 4.2). The hypothesis is that the lower value of $\beta_{\rm d}$ obtained by GRR is the result of resolving the stellar core of the $\gamma = 4/3$ polytrope not far enough.

In support of this hypothesis, my coauthors and I tested the dependence of $\beta_{\rm d}$ on the resolution of our simulations by performing some low-resolution ($\sim 10^3$ particles) GADGET2 simulations for the two polytropic indexes (black points in Figure 4.6). Figure 4.6 shows that for a $\gamma = 5/3$ polytrope (left-hand panel) the change in resolution has negligible effects on $\beta_{\rm d}$. On the other hand, for $\gamma = 4/3$ polytropes (right-hand panel) a strong dependence of $\beta_{\rm d}$ on resolution is evident below a resolution threshold because the configuration of the star is less stable.

Also, the dependence of $\beta_{\rm d}$ on different values of $M_{\rm BH}$ was determined by performing additional low-resolution ($\sim 10^3$ particles) GADGET2 simulations with a $\gamma = 5/3$ polytrope of mass $1{\rm M}_\odot$ and BHs of masses $10^5{\rm M}_\odot$ and $10^7{\rm M}_\odot$. Figure 4.7 clearly shows that $\beta_{\rm d}$ does not depend sensitively on $M_{\rm BH}$. I recall that flares and

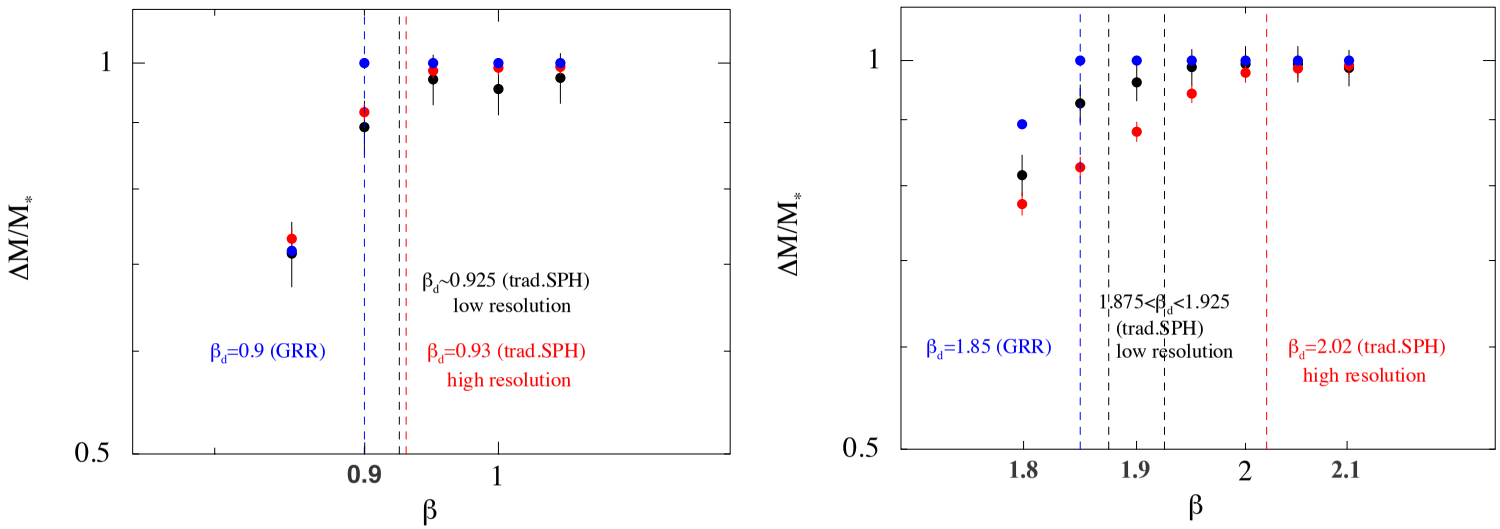

Figure 4.6: Comparison of mass losses as a function of β near $\beta_{\rm d}$ between the GRR simulations (blue points), high- ($\sim 10^5$ particles; red points) and low-resolution ($\sim 10^3$ particles; black points) GADGET2 simulations, for $\gamma = 5/3$ (left panel) and $\gamma = 4/3$ (right panel) polytropes. For a $\gamma = 4/3$ polytrope, the value of $\beta_{\rm d}$ clearly depends on the adopted resolution below a resolution threshold. For a $\gamma = 5/3$ polytrope, the value of $\beta_{\rm d}$ differs very slightly among the three simulations.

accretion temperatures, instead, depend on $M_{\rm BH}$ (e.g. Guillochon & Ramirez-Ruiz

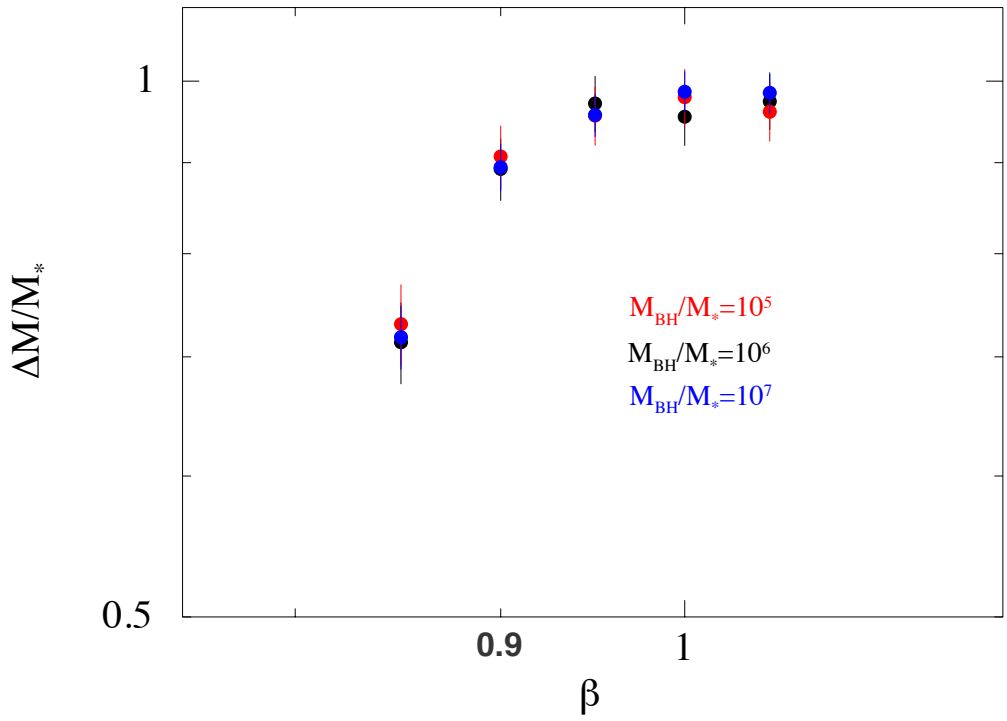

Figure 4.7: Comparison of mass losses as a function of β near $\beta_{\rm d}$ for a $\gamma = 5/3$ polytrope of mass $1{\rm M}_\odot$ approaching BHs with three different masses: $10^5{\rm M}_\odot$ (red points), $10^6{\rm M}_\odot$ (black points), $10^7{\rm M}_\odot$ (blue points). The value of $\beta_{\rm d}$ clearly does not depend on $M_{\rm BH}$.

2013; 2015a).

For completeness, I also show in Figure 4.8 how the polytropic index of the stellar remnant, which results from partial disruptions on parabolic orbits, is not preserved, but decreases with increasing β for both $\gamma = 5/3$ polytropes (left panel) and $\gamma = 4/3$ polytropes (right panel).

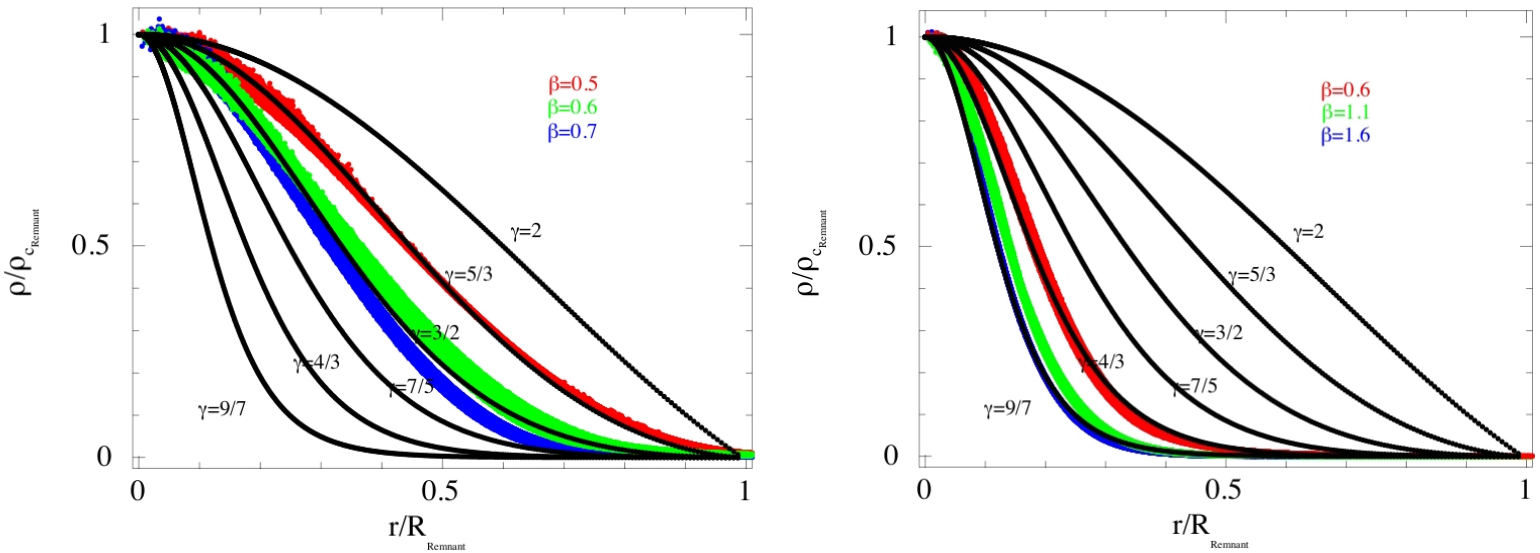

Figure 4.8: Changes in the value of the polytropic index of the stellar remnant resulting from partial disruptions for selected initial values of its β. Densities and radii are normalised to the central density and the radius of the remnant. Black curves represent solutions to the Lane-Emden equation for different values of γ; red, green, and blue points are from some of our simulations that left a remnant, for three different values of β. Left panel: $\gamma = 5/3$ polytrope. Right panel: $\gamma = 4/3$ polytrope.

4.3 Summary and main conclusions

Tidal disruption events provide a unique way to probe otherwise quiescent or low-luminous BHs at the centres of galaxies. When approaching the central BH of a galaxy, a star may be totally or partially disrupted by the BH tidal field, depositing material onto the compact object and lighting it up through a bright accretion flare (e.g. Rees 1988; Phinney 1989; Evans & Kochanek 1989). Such a tidal accretion flare is expected to be shaped by the structure of the disrupted star (e.g. Lodato et al. 2009) and the morphology of the star-BH encounter (e.g. Guillochon & Ramirez-Ruiz 2013; 2015a).

The hydrodynamical simulations of Guillochon & Ramirez-Ruiz of star-BH close encounters probably represent the most complete theoretical investigation of the properties of tidal disruption events (Guillochon & Ramirez-Ruiz 2013; 2015a). In each simulation, the star ($M_* = 1\mathrm{M}_\odot$, $R_* = 1\mathrm{R}_\odot$) is modelled as a polytrope of index $5/3$ or $4/3$ and evolved on a parabolic orbit with a specific pericentre around the BH ($M_{\mathrm{BH}} = 10^6\mathrm{M}_\odot$) using an AMR grid-based code. The assumption of parabolic orbit, together with the kick naturally imparted by the disruption itself (e.g. Manukian et al. 2013), prevents simulated partially disrupted stars from encountering the BH a multitude of times. The resulting stellar mass loss defines the morphology of the simulated encounter, that is, it defines whether the disruption is total or partial, thus shaping the ensuing accretion flare. Here the approach of Guillochon & Ramirez-Ruiz is followed, but adopting two SPH simulation codes (GADGET2, traditional SPH; Springel 2005; GIZMO, modern SPH; Hopkins 2015) and GIZMO in MFM mode (Hopkins 2015) instead of a grid-based method, as all these simulation techniques have their advantages, but also limits (section 4.1). The

main goal is to determine for each polytropic index whether the demarcation line between total and partial tidal disruption events, the critical disruption parameter $\beta_{\rm d}$ (Equation 4.1), is the same for different simulation techniques.

Figures 4.4 and 4.5 clearly show that for a $\gamma = 5/3$ polytrope the curves of stellar mass loss inferred from AMR grid-based simulations (red points) and from GIZMO MFM (blue points), traditional SPH (black points) and modern SPH (green points) simulations differ only slightly in the value of $\beta_{\rm d}$ (dashed lines), reflecting the limits of different codes (section 4.1), while for a $\gamma = 4/3$ polytrope there is disagreement between GADGET2 and GIZMO simulations and GRR simulations (Table 4.2), which is most likely due to the adopted resolutions; this interpretation is consistent with the resolution tests performed with GADGET2 simulations (Figure 4.6). However, even with equal resolution, the SPH approach should be superior to a grid-based approach at resolving the dynamics of the core of, especially, a $\gamma = 4/3$ polytrope, given that the resolution naturally follows density in equal-mass-particle approaches. As a consequence, my coauthors and I found $\beta_{\rm d} = 0.92 \pm 0.02$ (2.01 ± 0.01) for a $\gamma = 5/3$ ($4/3$) polytrope.

The $\gamma = 4/3$ profile is probably only appropriate for a zero-age main-sequence sun because the central density of our Sun is about twice greater than the $\gamma = 4/3$ polytrope at an age of 5 Gyr. For a real star, even greater resolution would therefore be needed in a grid-based approach in order to properly estimate the location of full versus partial disruption. Moreover, real stars are generally not well modelled by a single polytropic index, especially as they evolve (MacLeod et al. 2012). Giant stars consist of a tenuous envelope and a dense core, which prevents envelope mass loss, thus likely moving the value of $\beta_{\rm d}$ even ahead. A similar core-envelope structure and behaviour also characterise giant planets when they are disrupted by their host

star (Liu et al. 2013). Tidal disruption events could also refer to disruptions by stellar objects (Guillochon et al. 2011; Perets et al. 2016). However, the value of $\beta_{\rm d}$ for the latter encounters still remains to be investigated.

Chapter 5

Camelids in the sky: dromedary or camel?

Single- or double-peaked flares from double tidal disruptions

from *Mainetti, D., Lupi, A., Campana, S. & Colpi, M., 2016, MNRAS, 457, 2516*

Mainly, in the context of tidal disruption events, encounters involving a single star and a nuclear BH have been discussed. Such events are typically associated to single-peaked accretion flares, powered by the accretion onto the compact object of stellar debris resulting from the disruption. Stars in the nuclear star cluster of a galaxy, however, could also belong to hard stellar binaries, thus implying the need to also study close encounters between binaries and nuclear BHs which can lead to the tidal disruption of both the binary members. Indeed, Mandel & Levin (2015) first discussed this topic, suggesting that in a binary-BH encounter under certain conditions both binary components may undergo tidal disruption in sequence immediately after the tidal binary break-up. A double-peaked accretion flare is expected to occur, signature of such a peculiar event.

In this chapter, I present the results of a series of SPH simulations performed using the GADGET2 code (Springel 2005; already discussed in the previous chapter)

to study the physics of double tidal disruptions and to characterise the expected light curves. As a first exploratory study, parabolic encounters of stellar binaries with galactic central BHs in the Newtonian regime were considered, in order to explore which are the most favourable conditions for the occurrence of double-peaked flares. In particular, the following questions are addressed. Are all simulated encounters leading to double-peaked light curves or are there cases of single-peaked light curves? How different outcomes can be disentangled? How prominent are the double peaks?

The chapter is organised as follows. In section 5.1 I resume the conditions required for double tidal disruptions and the associated space of binary parameters (Mandel & Levin 2015). Section 5.2 deals with the initialisation of low-resolution SPH simulations of binary-BH encounters with different $r_{\rm p}$ values of the centre of mass of the binaries around the BH. Not all encounters can lead to double tidal disruptions, and in section 5.3 I introduce a classification of the obtained outcomes. In section 5.4 I show the results of a selected sample of high-resolution simulations and the light curves directly inferred from them. Section 5.5 sums up results and main conclusions.

5.1 Basics for double tidal disruptions

I am here interested in identifying the set conditions for the sequential tidal disruption of binary stars around galactic central BHs, following Mandel & Levin (2015).

Tidal break-up of a binary on a parabolic orbit around a BH occurs if the binary centre of mass around the BH enters a sphere of radius $r_{\rm tb}$ (Equation 1.16), being $a_{\rm bin}$ and $M_{\rm bin}$ the binary semi-major axis and total mass (e.g. Miller et al. 2005; Sesana et al. 2009). It can be noticed that binary break-up comes before single-star

tidal disruptions, given that $r_{\rm tb} > r_{\rm t}$ (Equations 1.16 and 1.1). Tidal break-up occurs when the specific angular momentum (in modulus) of the binary centre of mass at pericentre becomes less than

$$j_{\rm tb} \sim \sqrt{GM_{\rm BH}a_{\rm bin}\Big(\frac{M_{\rm BH}}{M_{\rm bin}}\Big)^{1/3}}. \tag{5.1}$$

A binary which satisfies this condition is broken up after one pericentre passage, over a time scale $P \sim 2\pi r^{3/2}/\sqrt{GM_{\rm BH}}$, corresponding to the orbital period of a binary on a circular orbit at the same distance from the BH.

Both stars of a binary can undergo a sequential tidal disruption immediately after the tidal binary break-up only if the specific angular momentum of the binary centre of mass around the BH at the closest approach, defined as $j_{\rm p} \sim \sqrt{GM_{\rm BH}r_{\rm p}}$, instantly changes from being greater than $j_{\rm tb}$ to becoming less than $j_{\rm t}$, where

$$j_{\rm t} \sim \sqrt{GM_{\rm BH}R_{*}\Big(\frac{M_{\rm BH}}{M_{*}}\Big)^{1/3}}. \tag{5.2}$$

In this way, the binary enters intact the region of single-star tidal disruptions. This occurs if the binary experiences a large enough deflection Δj, at least of the order of $j_{\rm tb}$, over a time scale P. Interactions with surrounding stars and/or massive perturbers can promote such a change (e.g. Perets et al. 2007; Alexander 2012). I consider empty the portion of the so-called loss-cone, in phase space, corresponding to binaries that break up before entering the region of single-star tidal disruptions, and full the portion of the loss-cone corresponding to binaries which can enter intact the region of single-star tidal disruptions (Merritt 2013).

In order to evaluate the distribution of the binary parameters associated with double disruptions, it is useful to determine $r_{\rm cr}$, defined as the distance of the binary from the BH before experiencing Δj, separating the two regimes. Considering

two-body relaxation over a time scale $t_{\rm r}$ (Equation 1.12) as the main mechanism which drives changes in angular momentum,

$$\Delta j \sim \Big(\frac{P}{t_{\rm r}}\Big)^{1/2} j_{\rm c}, \tag{5.3}$$

where $j_{\rm c} \sim \sqrt{GM_{\rm BH}r}$ (Merritt 2013; see also section 1.1). Thus, the critical condition $\Delta j \sim j_{\rm tb}$ enables to infer $r_{\rm cr}$. If the binary is orbiting inside a singular isothermal sphere density profile $\rho(r) = \sigma^2/(2\pi G r^2)$, where σ is the one-dimensional stellar velocity dispersion (Ferrarese & Ford 2005), $r_{\rm cr}$ reads

$$\begin{aligned} r_{\rm cr} &\sim \Big(\frac{0.34\sigma M_{\rm BH}^{5/6} a_{\rm bin}}{\sqrt{G}M_*^{4/3}\ln\Lambda}\Big)^2 \sim r_{\rm cr_*}\Big(\frac{a_{\rm bin}}{R_*}\Big)^2 \\ &\sim 10^7 {\rm R}_\odot \Big(\frac{\sigma}{70{\rm km/s}}\Big)^2 \Big(\frac{M_{\rm BH}}{10^6{\rm M}_\odot}\Big)^{5/3} \Big(\frac{a_{\rm bin}}{10{\rm R}_\odot}\Big)^2 \Big(\frac{1{\rm M}_\odot}{M_*}\Big)^{8/3} \Big(\frac{15}{\ln\Lambda}\Big)^2, \end{aligned} \tag{5.4}$$

where I renamed $r_{\rm cr}$ from Equation 1.14 (single-star tidal disruptions) as $r_{\rm cr_*}$. It is worth noting that $r_{\rm cr}$ is comparable to the radius of gravitational influence for a BH of mass $10^6{\rm M}_\odot$ (Equation 1.15).

A binary carries internal degrees of freedom, and in particular the relative velocity of the two binary components, $\sqrt{GM_{\rm bin}/a_{\rm bin}}$, is clearly smaller than the orbital velocity of the binary centre of mass relative to the BH, $\sqrt{GM_{\rm BH}/r}$. The velocity of the two stars relative to the centre of mass of the stellar binary gives then a small contribution to the specific angular momentum of each binary star relative to the BH at $r_{\rm tb}$ that approximately is

$$\delta j \sim \sqrt{GM_{\rm bin}a_{\rm bin}}\Big(\frac{M_{\rm BH}}{M_{\rm bin}}\Big)^{1/3}. \tag{5.5}$$

Sequential disruptions are expected to be favoured when δj is very small. Indeed, the smaller δj is, the more each binary component has an orbit around the BH

similar to the one of the binary centre of mass, i.e. a similar pericentre passage. Thus,

$$\frac{\delta j}{j_{\rm t}} \sim \sqrt{\frac{a_{\rm bin}}{R_*}}\Big(\frac{M_*}{M_{\rm BH}}\Big)^{1/3} \ll 1, \tag{5.6}$$

where $M_{\rm bin}$ is approximated to M_*. For $M_* = 1{\rm M}_\odot$, $R_* = 1{\rm R}_\odot$, $M_{\rm BH} = 10^6{\rm M}_\odot$, $a_{\rm bin} \ll 10^4{\rm R}_\odot$. Hence, the second condition for double tidal disruptions, which joins the condition on Δj, is the involvement of close binaries. Furthermore, very close binaries are required in order to avoid their evaporation due to interactions with field stars before tidal binary break-up (Merritt 2013).

In the full loss-cone regime, the parameter space of binaries that can undergo double tidal disruptions can be inferred from the rate of binary entrance in the region of stellar tidal disruptions per unit of r and $a_{\rm bin}$ as found in Mandel & Levin (2015):

$$\frac{{\rm d}^3N(a_{\rm bin}, r)}{{\rm d}r\,{\rm d}a_{\rm bin}\,{\rm d}t} \sim \Big(\frac{j_{\rm t}}{j_{\rm tb}}\Big)^2\,\frac{4\pi r^2\rho(r)\xi(a_{\rm bin})}{M_*P}, \tag{5.7}$$

where $(j_{\rm t}/j_{\rm tb})^2$ is the probability for a binary to enter directly the single tidal disruption region (Merritt 2013) and $\xi(a_{\rm bin}) = [\ln(a_{\rm max}/a_{\rm min})]^{-1}a_{\rm bin}^{-1}$ is the distribution function for $a_{\rm bin}$ given in Öpik (1924), with $a_{\rm max}$ and $a_{\rm min}$ being the maximum and the minimum semi-major axes of stellar binaries in a generic galactic field. Integration of Equation 5.7 over r, between $r_{\rm cr}$ and $+\infty$, allows the evaluation of the number of binaries that may undergo sequential tidal disruption of their components per unit of time and unit of $a_{\rm bin}$. The resulting integral scales as

$$\frac{{\rm d}^2N(a_{\rm bin})}{{\rm d}a_{\rm bin}\,{\rm d}t} \propto \Big[\ln\Big(\frac{a_{\rm max}}{a_{\rm min}}\Big)\Big]^{-1}R_*a_{\rm bin}^{-3}. \tag{5.8}$$

From Kepler's law, $a_{\rm bin}$ can be connected with the internal orbital period of the stellar binaries $P_{\rm bin}$ to infer the number of events per unit of time and unit of $P_{\rm bin}$.

The resulting rate is

$$\frac{\mathrm{d}^2 N(P_{\rm bin})}{\mathrm{d}P_{\rm bin}\,\mathrm{d}t} \propto \left[\ln\left(\frac{a_{\rm max}}{a_{\rm min}}\right)\right]^{-1} R_* P_{\rm bin}^{-7/3}. \tag{5.9}$$

This scaling was adopted to extract the initial conditions of the SPH simulations.

Thus, in the case of solar-mass stars (i.e. $R_* = 1\mathrm{R}_\odot$), the contribution of double tidal disruptions to all tidal disruptions could be approximately estimated by integrating Equation 5.8 over all $a_{\rm bin}$ and dividing it by the corresponding integral obtained after integration over r of Equation 5.7, with R_* in place of $a_{\rm bin}$ and $r_{\rm cr_*}$ in place of $r_{\rm cr}$. This ratio scales as $[\ln(a_{\rm max}/a_{\rm min})]^{-1}(1/a_{\rm min}^2 - 1/a_{\rm max}^2)$, which gives $\sim 10\%$ also assuming $a_{\rm max} = 10^4\mathrm{R}_\odot$ and $a_{\rm min} = 1\mathrm{R}_\odot$, together with considering that the multiplicity of stars is single:double fifty-fifty for 100 solar-type stars, disregarding uncertainties in the number of very close binaries.

The definition of the parameter space of binaries that may be double tidally disrupted is fundamental to sensibly define the initial conditions of a small number of representative low-resolution simulations aimed at checking different outcomes from different initial parameters, and particularly from different pericentre radii of the binary centre of mass.

5.2 General parameter definition for low-resolution SPH simulations

The simulations in this chapter were performed using the TreeSPH code GADGET2 (Springel 2005). In SPH codes, a star is represented by a set of gas particles. Each particle is characterised by a spatial distance, the smoothing length, over which its properties are 'smoothed' by its kernel function, i.e. evaluated by summing the properties of particles in the range of the kernel according to the kernel itself (Price

2005). In particular, in GADGET2 the smoothing length of each particle is defined so that its kernel volume contains a constant mass, and is allowed to vary with time, thus adapting to the local conditions. The kernel adopted here is the one used most commonly and is based on cubic splines (e.g. Monaghan & Lattanzio 1985). On the other hand, gravitational interactions between particles are computed through a hierarchical oct-tree algorithm, which significantly reduces the number of pair interactions needed to be computed. The definition of a gravitational softening length $\epsilon \sim 0.1 R_*/(N_{\rm part})^{1/3}$, where $N_{\rm part}$ is the total number of particles, prevents particle overlapping. GADGET2 enables the following of the temporal evolution of single particle properties and the inference from them of tidal disruption light curves (section 5.4.2).

Fourteen low-resolution simulations of parabolic encounters between equal-mass binaries and BHs (LE runs) were run to test the nature of the outcomes for different initial conditions, varying binary parameters, $M_{\rm BH}$ and $r_{\rm p}$. The stellar binaries were first evolved in isolation for several dynamical times to ensure their stability. The BH force was implemented in the code analytically, as a Newtonian potential, and particles falling below the innermost stable circular orbit radius $R_{\rm ISCO}$ were excised from simulations. Equal solar-mass stars were considered, modelled as polytropes of index $5/3$ and each sampled with 10^3 particles. Some correspondent high-resolution simulations are presented in section 5.4.2. The initial binary internal orbital periods $P_{\rm bin}$ and semi-major axes $a_{\rm bin}$ were extracted according to the distributions described in section 5.1. Based on the work of Duquennoy & Mayor (1991), binaries with 0.1 d ($a_{\rm bin} \sim 1{\rm R}_\odot$) < $P_{\rm bin}$ < 10 d ($a_{\rm bin} \sim 10{\rm R}_\odot$) were considered to be circular, binaries with 10 d $\leq P_{\rm bin} \leq$ 1000 d ($a_{\rm bin} \sim 500{\rm R}_\odot$) to have internal eccentricities distributed according to a Gaussian of mean 0.3 and

standard deviation 0.15 and binaries with 1000 d < $P_{\rm bin}$ < 1000 yr ($a_{\rm bin} \sim 10^4 {\rm R}_\odot$) to have internal eccentricities which follow a thermal distribution $p(e_{\rm bin}) \sim 2e_{\rm bin}$. In order to avoid immediate collisions between the binary components, the initial percentre radius of the internal binaries (i.e. $a_{\rm bin}(1-e_{\rm bin})$) was set greater than twice the sum of the stellar radii, which are

$$R_* = \left(\frac{M_*}{{\rm M}_\odot}\right)^k {\rm R}_\odot, \tag{5.10}$$

with $k = 0.8$ for $M_* < 1{\rm M}_\odot$ and $k = 0.6$ for $M_* > 1{\rm M}_\odot$, according to Kippenhahn & Weigert (1994), $R_* = 1{\rm R}_\odot$ for $M_* = 1{\rm M}_\odot$. Binaries were then placed on parabolic orbits around the BH at an initial distance ten times greater than the tidal binary break-up radius $r_{\rm tb}$, thus preventing initial tidal distortions from the BH. BHs of masses 10^5 and $10^6{\rm M}_\odot$were considered. The nominal pericentre distances $r_{\rm p}$ were generated between 1 and $800{\rm R}_\odot$. Stars were placed on Keplerian orbits and their positions and velocities relative to their binary centre of mass and to the BH were assigned accordingly. The initial internal binary plane was set, arbitrarily, perpendicular to the orbital plane around the BH. The results of these simulations are shown in section 5.3.

5.3 Outcomes of low-resolution SPH simulations

Tables 5.1 and 5.2 summarise the results of low-resolution simulations as a function of $M_{\rm BH}$, $a_{\rm bin}$ and $r_{\rm p}$. Several outcomes from binary-BH encounters are possible, including the results of these simulations:

(i) PD-TDE: partial double tidal disruptions,

Table 5.1: Outcomes of low-resolution SPH simulations of parabolic binary-BH encounters ($M_* = 1\mathrm{M}_\odot$, $R_* = 1\mathrm{R}_\odot$) as a function of $a_{\rm bin}$ and $r_{\rm p}$. Here $M_{\rm BH} = 10^6\mathrm{M}_\odot$, $r_{\rm t} = 100.0\mathrm{R}_\odot$, $r_{\rm tb}(a_{\rm bin} = 4.9\mathrm{R}_\odot) = 390.0\mathrm{R}_\odot$, $r_{\rm tb}(a_{\rm bin} = 9.8\mathrm{R}_\odot) = 780.0\mathrm{R}_\odot$. TD-TDE stands for total double tidal disruptions, ATD-TDE for almost total double tidal disruptions (i.e. more than $\sim 70\%$ of stellar mass lost), PD-TDE for partial double tidal disruptions, MG for merger, BBK for binary break-up without stellar disruptions.

$a_{\rm bin}\backslash r_{\rm p}$ ($\mathrm{R}_\odot$)	50.0	100.0	142.6	200.0	420.0	780.0
4.9	LE1: TD-TDE	LE2: ATD-TDE	LE3: PD-TDE	LE4: PD-TDE	LE5: MG	
9.8		LE9: ATD-TDE		LE10: PD-TDE		LE11: BBK

Table 5.2: Same as Table 5.1, with $M_{\rm BH} = 10^5\mathrm{M}_\odot$, $r_{\rm t} = 50.0\mathrm{R}_\odot$, $r_{\rm tb}(a_{\rm bin} = 4.9\mathrm{R}_\odot) = 180.0\mathrm{R}_\odot$, $r_{\rm tb}(a_{\rm bin} = 9.8\mathrm{R}_\odot) = 360.0\mathrm{R}_\odot$. PD-TDE stands for partial double tidal disruptions, MG for merger, BBK for binary break-up without stellar disruptions, UN for undisturbed binary.

$a_{\rm bin}\backslash r_{\rm p}$ ($\mathrm{R}_\odot$)	50.0	100.0	142.6	200.0	420.0	780.0
4.9		LE6: PD-TDE		LE7: MG	LE8: UN	
9.8		LE12: PD-TDE		LE13: BBK		LE14: UN

(ii) ATD-TDE: almost total double tidal disruptions, i.e. more than $\sim 70\%$ of stellar mass is lost,

(iii) P&T-TDE: single partial plus single total tidal disruption,

(iv) TD-TDE: total double tidal disruptions,

(v) MG: merger of the binary components,

(vi) BBK: tidal binary break-up without stellar tidal disruptions,

(vii) UN: undisturbed binary.

The intensity of the disruptions, i.e. the morphology of the resulting objects, was estimated from simulation results based on the tidal deformation, the extent of stellar mass loss and possible orbital changes of the binary stars with pericentre passage. After closest approach, the orbital evolution of the binary stars around the BH was computed using an N-body Hermite code (e.g. Hut & Makino 1995; the code can be freely downloaded from https://www.ids.ias.edu/$\sim$piet/act/comp/algorithms/starter/), knowing the current position and velocity of the centre of mass of each binary component from SPH simulations (see section 5.4.2 for the recipe used to infer the position and velocity of the centre of mass). The use of the Hermite code enables the overcoming of the high computational time required by SPH simulations to track the dynamics of stars when the bulk of the hydrodynamical processes have subsided.

This section also contains an inventory of representative orbits according to the classification highlighted above. Tables 5.3 and 5.4, respectively, refer to the simulations described in Tables 5.1 and 5.2. There, the orbital evolution of the binary components around the BH is shown, for each simulation, in the (x, y) and

Table 5.3: Same as Table 5.1, also with the orbital evolution of the binary components around the BH for each simulation, projected in the (x, y) and (y, z) planes. Evolutions start at (0,0), (0,0). Figures are in $\mathrm{R}_\odot$. The initial orbits of the binary centre of mass, inferred from the BH position (black dots) and the pericentre radius r_p, are traced in blue. Red and green curves represent the orbital evolution of the binary components as respectively inferred from SPH and N-body simulations.

$\mathrm{a_{bin}} \backslash \mathrm{r_p}$ $(\mathrm{R}_\odot)$	50.0	100.0	142.6
4.9	LE1:TD-TDE	LE2:ATD-TDE	LE3: PD-TDE
	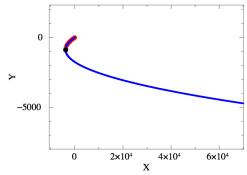	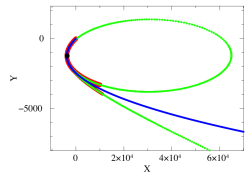	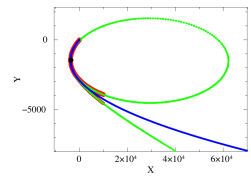
	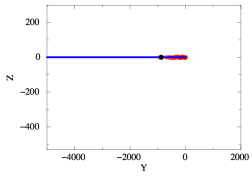	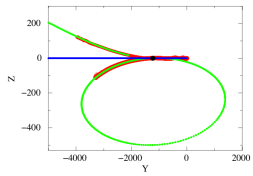	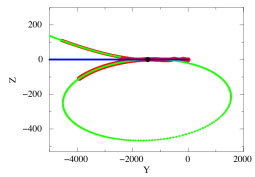
9.8		LE9: ATD-TDE	
		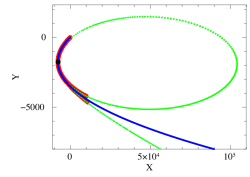	
		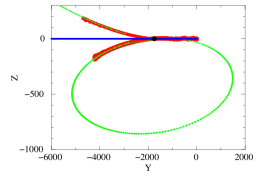	

$a_{bin}\backslash r_p$ ($R_\odot$)	200.0	420.0	780.0
4.9	LE4: PD-TDE	LE5:MG	
	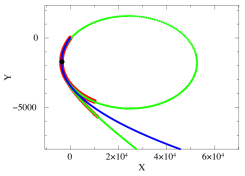	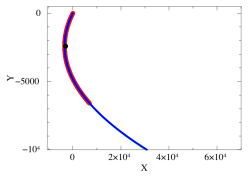	
	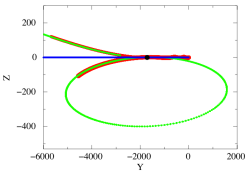	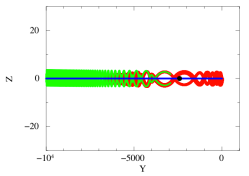	
9.8	LE10: PD-TDE		LE11: BBK
	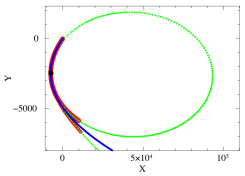		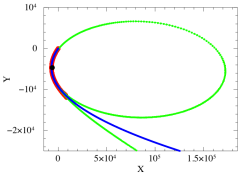
	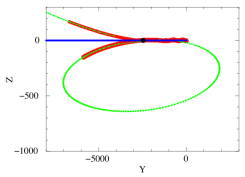		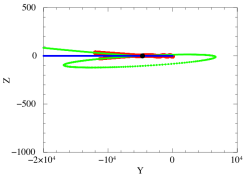

Table 5.4: Same as Table 5.3, though following Table 5.2.

$a_{bin} \backslash r_p$ ($R_\odot$)	50.0	100.0	142.6
4.9	LE6: PD-TDE		
	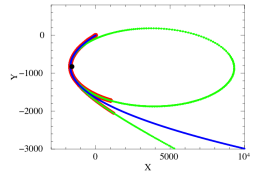		
	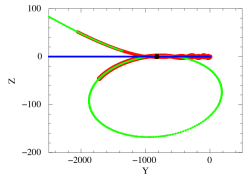		
9.8	LE12: PD-TDE		
	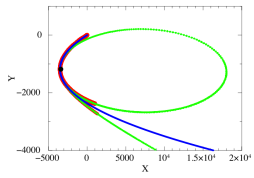		
	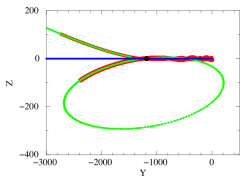		

$a_{bin} \backslash r_p$ ($R_\odot$)	200.0	420.0	780.0
4.9	LE7: MG	LE8: UN	
	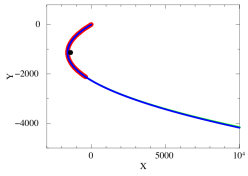	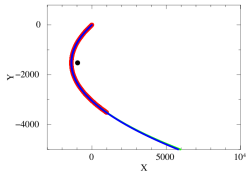	
	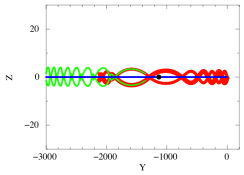	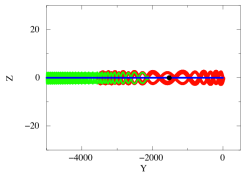	
9.8	LE13: BBK		LE14: UN
	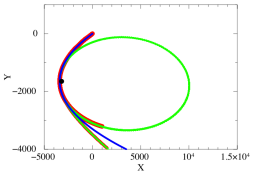		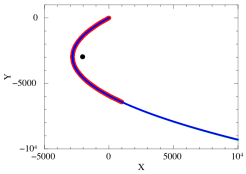
	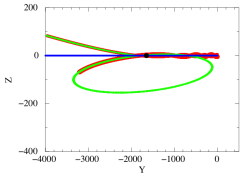		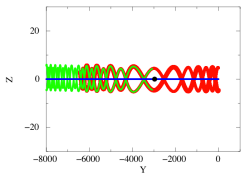

(y, z) planes, starting from (0, 0), (0, 0). Units are in $\mathrm{R}_\odot$. Blue curves represent the initial parabolic orbits of the binary centre of mass around the BH, each inferred from the position of the BH and the pericentre radius r_p. Red curves trace the orbital evolution of the binary components as inferred from SPH simulations, while green curves trace the orbital evolution of the stars as computed using the Hermite code. Black dots indicate the position of the BH. Mergers (MGs; LE5, LE7) are found when the two binary components progressively reduce their relative separation starting from just before the pericentre passage around the BH, without being tidally separated. The MG product, which is represented by stars at a fixed minimum distance in simulations performed using the Hermite code, follows an orbit which overlaps the initial parabolic one of the binary centre of mass. In the UN case (LE8, LE14), the binary keeps its internal and external orbits unchanged, even after pericentre passage. Double disruptions (D-TDEs; LE1, LE2, LE3, LE4, LE6, LE9, LE10, LE12) are preceded by tidal binary separation, which can also occur without stellar disruptions (BBK; LE11, LE13). Binary break-up leads one star to get bound to the BH and the other to remain unbound. In the case of BBK or partial disruptions, the latter may leave the system at a high velocity, becoming an hypervelocity star (Hills 1988; Antonini et al. 2011).

5.4 High-resolution SPH simulations

5.4.1 A glimpse to simulated double tidal disruptions

The low-resolution simulations described in sections 5.2 and 5.3 served as guide for the selection of three higher-resolution SPH simulations, with an increased number of particles per star equal to 10^5. A number of particles per star of 10^6 would require too much computational time. Indeed, the computational cost in

Table 5.5: Same as Table 5.1 for high-resolution simulations involving equal-mass binaries.

$a_{\rm bin}\backslash r_{\rm p}$ ($\rm R_\odot$)	50.0	100.0	142.6
4.9	HEp50: TD-TDE	HEp100: ATD-TDE	HEp143: PD-TDE

GADGET2 scales as $N_{\rm part}\log N_{\rm part}$, which is a factor of 12 higher in the case of $N_{\rm part}=10^6$ with respect to $N_{\rm part}=10^5$.

The goal here is to infer directly from simulations the light curves associated with double tidal disruptions of different intensities. For this reason, the initial conditions for an almost total, a partial and a total double disruption event were set, following simulations LE2 and LE3 for the not fully disruptive events and simulation LE1 in order to obtain a total double disruption. Table 5.5 summarises the outcomes which came out from these three high-resolution simulations (HE runs) as a function of $a_{\rm bin}$ and $r_{\rm p}$. These results are the same as expected from the corresponding low-resolution simulations (Table 5.1). Furthermore, Figure 5.1 (upper panels) points out that the orbits of the binary stars follow the same evolution in corresponding low- (red curves) and high-resolution (green curves) SPH simulations after pericentre passage, assuring numerical convergence.

Figure 5.2 shows representative snapshots of the SPH particle distribution, projected in the (x, y) plane and in fractions of pericentre time, depicting the dynamics of simulations HEp50 (left column), HEp100 (central column) and HEp143 (right column). Panels are in $\rm R_\odot$. In each simulation, black particles originally shape the star which will get bound to the BH after binary separation,

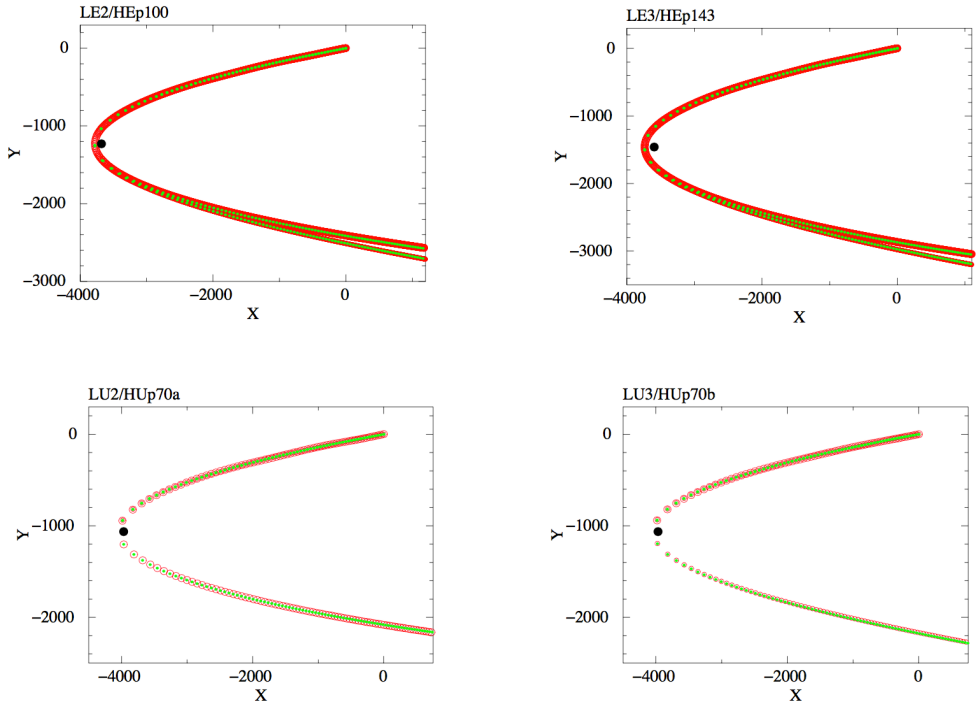

Figure 5.1: Orbital evolution of the binary stars, starting from (0,0) in the (x, y) plane, as inferred from the corresponding low- (red curves) and high-resolution (green curves) SPH simulations for LE2/HEp100 and LE3/HEp143 (upper panels) and LU2/HUp70a and LU3/HUp70b (bottom panels). Simulations LE1/HEp50 and LU1/HUp42 are not considered given that both the binary stars were totally disrupted when approaching the BH. Black dots indicate the position of the BH. Units are in $\mathrm{R}_{\odot}$.

whereas red particles initially belong to the one which will unbind. The remnant of the binary components after disruption is clearly visible in the almost total (HEp100) and partial double (HEp143) tidal disruption cases. Forward in time, the distribution of the particles which leave the stars once tidally disrupted visibly spreads, and particles originally associated with the two different stars tend to mix, preventing their by-eye distinction. For this reason, snapshots of the SPH particle distribution are introduced in place of snapshots of the SPH particle density, which are shown for the first time in Figure 5.3 (in log scale), projected in the (x, y) plane, only at $0.0004\mathrm{yr}$ ($\sim 0.15\mathrm{d}$) after pericentre passage for the simulated total double (HEp50) and partial double (HEp143) tidal disruption. Again, the remnant of the binary components is clearly visible in the partially disruptive encounter.

The selection of the stellar debris associated with a specific star was possible thanks to a detailed analysis of the snapshots. This enabled the extraction of the light curves associated with each single-star disruption and then the inference of the composite light curves associated with double disruptions. I discuss this in the following section.

5.4.2 Double tidal disruption light curves: the case of equal-mass binaries

The basic (simplifying) assumption when inferring the light curves associated with tidal disruptions is that the accretion rate onto the BH has close correspondence to the rate of stellar debris returning to pericentre after disruption. Indeed, if the viscous time (e.g. Ulmer 1999; Li et al. 2002) driving the fallback of stellar debris onto the BH is negligible compared to the returning time at pericentre of the most bound material since the time of stellar disruption (which is generally the case in

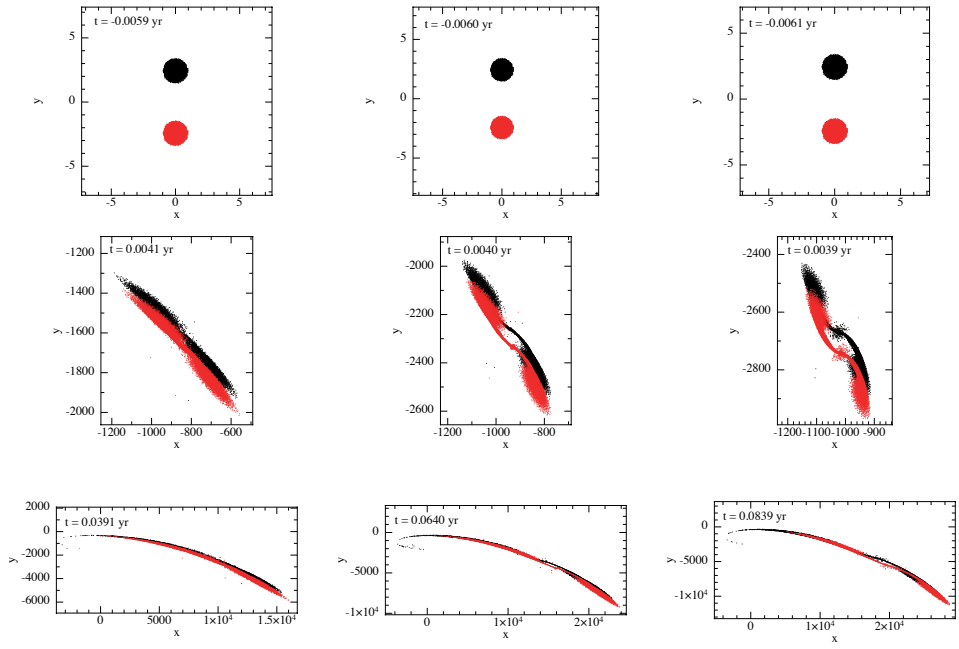

Figure 5.2: Representative high-resolution snapshots of the SPH particle distribution, respectively, in simulations HEp50 (left column), HEp100 (central column) and HEp143 (right column), projected in the (x, y) plane. Positional units are in $\mathrm{R}_{\odot}$ and times are in fractions of pericentre time. Black particles originally belong to the star which will get bound to the BH after tidal binary break-up and red particles depict its companion. The BH is at position (x, y) = (-3779.62,-875.17) (simulation HEp50), (x, y) = (-3679.62,-1229.57) (simulation HEp100), (x, y) = (-3594.48, -1459.84) (simulation HEp143). The survived binary components are clearly visible in the almost total (HEp100) and partial (HEp143) tidal disruption cases, whereas stars are fully disrupted after pericentre passage in the total tidal disruption case (HEp50).

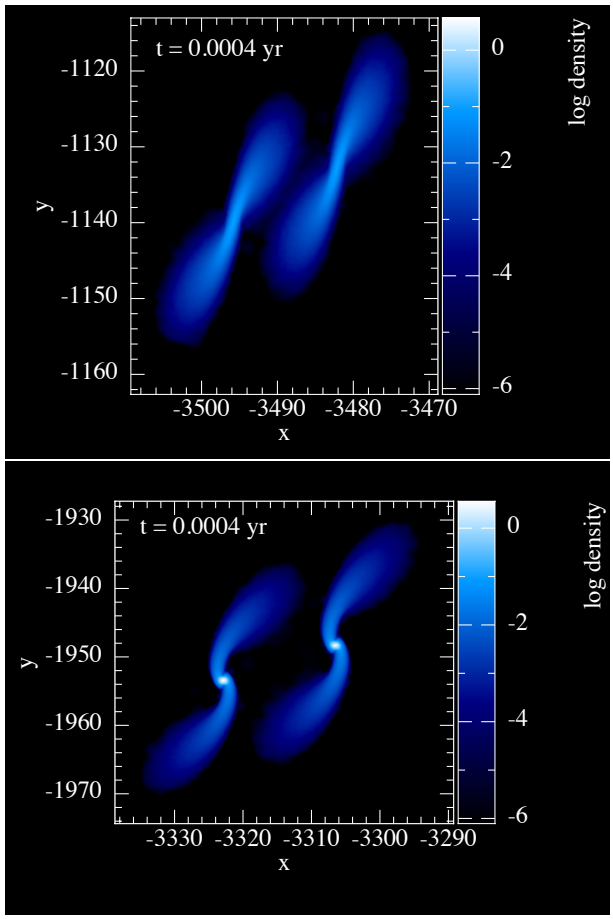

Figure 5.3: Snapshots of the SPH particle density (in log scale) for the simulated total double (HEp50; upper panel) and partial double (HEp143; bottom panel) tidal disruption at $t = 0.0004\mathrm{yr}$ ($\sim 0.15\mathrm{d}$) after pericentre passage, projected in the (x, y) plane. The remnant binary components are clearly visible in the partial double disruption case.

these simulations), and the stellar debris circularise quickly, then the rate of debris returning at pericentre

$$\dot{M}(t) = \frac{\left(2\pi G M_{\rm BH}\right)^{2/3}}{3} \frac{dM}{d\epsilon} t^{-5/3}, \tag{5.11}$$

(Equation 1.20) coincides to first approximation to the rate of accretion onto the BH. Inferring $\dot{M}(t)$ is thus equivalent of computing the accretion luminosity $L(t)$ associated to a tidal disruption event

$$L(t) = \eta \dot{M}(t) c^2, \tag{5.12}$$

assuming an appropriate efficiency η.

In Equation 5.11, $dM/d\epsilon$ is the distribution of the stellar debris per unit energy as a function of ϵ, the specific binding energy relative to the BH. Generally, such a distribution is neither flat nor constant in time (e.g. Lodato et al. 2009; Guillochon & Ramirez-Ruiz 2013; 2015a), allowing $\dot{M}(t)$ to deviate from the classically assumed $t^{-5/3}$ trend, inferred from Equation 5.11 when taking a uniform distribution in ϵ (e.g. Rees 1988; Phinney 1989).

Here, $dM/d\epsilon$ was computed as a function of time for each binary component directly from simulations, following the recipe from Guillochon & Ramirez-Ruiz (2013; 2015a). The position and velocity of the centre of mass of each star around the BH were computed through an iterative approach. The initial reference point was the particle with the highest local density. Particles within $2\mathrm{R}_\odot$ from it (a bit more than R_*) were considered to be still bound to the star and their total mass was denoted as $M_{\rm B}$. The specific binding energy of the ith particle relative to the star

was calculated as

$$\epsilon_{*_i} = \frac{1}{2}|\mathbf{v}_i - \mathbf{v}_{\rm peak}|^2 - \frac{GM_{\rm B}}{|\mathbf{r}_i - \mathbf{r}_{\rm peak}|}, \tag{5.13}$$

where $\mathbf{v}_i - \mathbf{v}_{\rm peak}$ and $\mathbf{r}_i - \mathbf{r}_{\rm peak}$ are the velocity and position of the ith particle relative to the reference particle. Velocity and position of the temporary centre of mass were determined through the standard formulae by considering only particles with $\epsilon_{*_i} < 0$. Equation 5.13 was then re-evaluated with the new velocity and position of the centre of mass in place of $\mathbf{v}_{\rm peak}$ and $\mathbf{r}_{\rm peak}$. This process was re-iterated until the convergency of the velocity of the centre of mass to a constant value, to less than $10^{-5}{\rm R}_\odot{\rm yr}^{-1}$. Particles with $\epsilon_{*_i} > 0$, i.e. unbound from the star, were then selected in the aim at evaluating their specific binding energy relative to the BH

$$\epsilon_i = \frac{1}{2}|\mathbf{v}_i|^2 - \frac{GM_{\rm BH}}{|\mathbf{r}_i - \mathbf{r}_{\rm BH}|}, \tag{5.14}$$

where $\mathbf{v}_i$ and $\mathbf{r}_i - \mathbf{r}_{\rm BH}$ are the velocity and position of the ith particle relative to the BH. Particles with $\epsilon_i > 0$ are unbound from the BH, whereas particles with $\epsilon_i < 0$ form the stream of debris bound to the BH. Data were then binned in ϵ, i.e. the specific binding energies $\epsilon_i < 0$ were grouped in bins and the correspondent particles fill this histogram. $dM/d\epsilon$ as a function of ϵ (i.e. time) was obtained dividing the total mass of particles in each bin by the bin amplitude.

The time t in Equation 5.11 is the time since disruption, which is coincident with the first pericentre passage for the purposes here. Thus, only material with orbital periods $P = 2\pi GM_{\rm BH}/(2\epsilon)^{3/2}$ around the BH less than t contributes to the accretion till that time.

To build the composite light curves, the light curve for each star was computed by interpolating the data coming from different snapshots and then the results of interpolations were summed, point to point. Green and blue curves in Figure 5.4

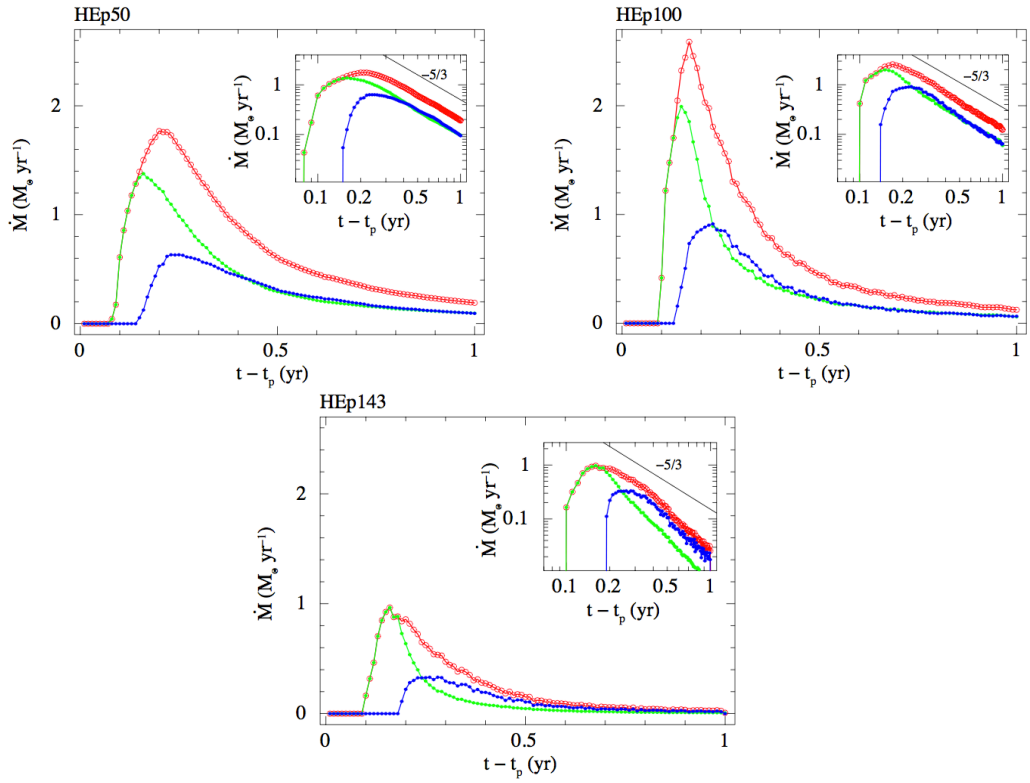

Figure 5.4: Light curves ($\dot{M}$ vs time; see Equation 5.12 to convert accretion rates into luminosities) inferred from high-resolution simulations of parabolic equal-mass binary-BH encounters, depicting a fully disruptive encounter (simulation HEp50), an almost total double disruption (simulation HEp100) and a partial double tidal disruption (simulation HEp143). Green and blue curves are associated with the disruption of the binary components, red curves reproduce the point-wise sum of the green and blue curves. On the right top corners, the same plots are shown in logarithmic scale. A knee in the red curve is somehow visible in simulation HEp143, expecially in the logarithmic plot, and it decays more steeply than the classically assumed power law of index $-5/3$.

are associated with the disruption of the single binary components while red curves represent the point-wise sum of the green and blue curves. Panels on the right top corners show logarithmic plots.

The light curves associated with tidal disruptions are described by characteristic parameters, which can be assessed directly from the light curves and also analytically, in order to check the reliability of the recipe here followed. The first characteristic parameter is $t_{\rm min}$, the returning time at pericentre of the most bound stellar debris since disruption. For a star on a parabolic orbit around a BH it can be evaluated as

$$\tilde{t}_{\rm min} = \frac{\pi}{\sqrt{2}} \frac{G M_{\rm BH}}{\epsilon^{3/2}} \sim \frac{\pi}{\sqrt{2}} \frac{1}{\sqrt{G}} \frac{M_{\rm BH}^{1/2}}{M_*} R_*^{3/2}, \tag{5.15}$$

where ϵ is the specific energy spread caused by the disruption (Equation 1.18), given that the orbital energy associated with a parabolic orbit is zero. Here in the simulations, the binary centre of mass was set on a parabolic orbit around the BH but the binary components were a bit out of it. Moreover, after the tidal binary separation they followed new orbits: an ellipse for the bound star, an hyperbola for the unbound star. Thus the returning time associated with each binary component is not simply $\tilde{t}_{\rm min}$, as it requires knowledge of the new orbits of the separated stars. Hereafter, I denote with subscript 1 (2) the bound (unbound) binary component.

For the bound star, the returning time can be evaluated as

$$t_{\rm min_1} = \frac{\pi}{\sqrt{2}} \frac{G M_{\rm BH}}{\epsilon^{3/2}} \sim \tilde{t}_{\rm min} \Big(\frac{M_*}{M_{\rm BH}} \Big)^{1/2} \times \\ \times \frac{1}{(\beta_1 (1-e_1))^{3/2}} \Big(\frac{1}{2} + \frac{\big(M_*/M_{\rm BH}\big)^{1/3}}{\beta_1 (1-e_1)} \Big)^{-3/2}, \tag{5.16}$$

where e_1 is the eccentricity of its new orbit (computed through the Hermite code), β_1 the impact parameter of its centre of mass and $\epsilon \sim \epsilon_{\rm orb} + \Delta\epsilon$, with

$\epsilon_{\rm orb} \sim GM_{\rm BH}\beta_1(1-e_1)/(2r_{\rm t}) \neq 0$. This time was also inferred from simulations, considering as "mostly bound" the first returned particles after disruption associated with the bound star. As minimum of significance, 10 particles out of the set of particles, associated with the bound star, bound to the BH were assumed. If the impact parameters of both the binary components, β_1 and β_2, are close to unity, the two estimates of $t_{\rm min_1}$ are in good agreement. In this case, the returning time for the unbound star, $t_{\rm min_2}$, was inferred directly from simulations. On the contrary, the more β_1 and β_2 depart from unity, the worse the agreement is. In this case, a correction factor between the two estimates of $t_{\rm min_1}$ was introduced and used to correct $t_{\rm min_2}$ as inferred from simulations. $\tilde{t}_{\rm min}$, $t_{\rm min_1}$ and $t_{\rm min_2}$ are reported in Table 5.6 for the three high-resolution simulations.

Corrections for the new orbits of the separated stars also involve the second characteristic parameter of tidal disruption light curves, $t_{\rm peak}$, that is the rise time between the time of stellar disruption and the time at which the accretion rate peaks. If the two binary components were on parabolic orbits corresponding to the initial one of their binary centre of mass, the rise time for each star would be denoted as $\tilde{t}_{\rm peak}$ (1,2) and could be evaluated following Guillochon & Ramirez-Ruiz (2013; 2015a). Corrected values come out to be

$$t_{\rm peak} \sim \tilde{t}_{\rm peak}\frac{t_{\rm min}}{\tilde{t}_{\rm min}}, \tag{5.17}$$

assuming that $t_{\rm min}$ and $t_{\rm peak}$ change proportionally. Table 5.6 collects $\tilde{t}_{\rm peak}$ (1,2) and $t_{\rm peak}$ (1,2) for the three high-resolution simulations.

The last characteristic parameter of tidal disruption light curves is the peak of accretion rate, $\dot{M}_{\rm peak}$. According to MacLeod et al. (2013), this parameter is linked to the mass of the debris which binds to the BH $M_{\rm bound_{BH}}$ and to the rise time $t_{\rm peak}$

Table 5.6: Characteristic parameters of the light curves inferred from the high-resolution simulations of equal-mass binary-BH encounters, as analytically estimated. Simulations HEp50, HEp100 and HEp143 respectively correspond to the ones in Figure 5.4. $t_{\rm min}$ is the returning time at pericentre of the most bound stellar debris since disruption, $t_{\rm peak}$ the rise time from stellar disruption to accretion rate peak, $\dot{M}_{\rm peak}$. Tilded values were evaluated setting the binary components on parabolic orbits correspondent to the initial one of the binary centre of mass, untilded values consider the effective orbits of the binary stars. The 1 (2) subscript denote the BH bound (unbound) star. $\Delta t_{\rm peak}$ and $\Delta\dot{M}_{\rm peak}$ are the differences in rise times and accretion rate peaks between the two "humps" expected in the composite light curves associated with double tidal disruptions, actually visible only in the partially disruptive encounter (simulation HEp143; Figure 5.4).

	HEp50: TD-TDE	HEp100: ATD-TDE	HEp143: PD-TDE
$\tilde{t}_{\rm min}({\rm yr})$	0.1126	0.1126	0.1126
$t_{\rm min_1}({\rm yr})$	0.0987	0.0963	0.0946
$t_{\rm min_2}({\rm yr})$	0.1777	0.1681	0.1873
$\tilde{t}_{\rm peak_1}({\rm yr})$	0.1807	0.1618	0.1738
$t_{\rm peak_1}({\rm yr})$	0.1585	0.1384	0.1460
$\tilde{t}_{\rm peak_2}({\rm yr})$	0.1779	0.1617	0.1751
$t_{\rm peak_2}({\rm yr})$	0.2809	0.2415	0.2915
$\tilde{\dot{M}}_{\rm peak_1}({\rm M_\odot yr^{-1}})$	1.254	1.672	0.595
$\dot{M}_{\rm peak_1}({\rm M_\odot yr^{-1}})$	1.566	2.088	0.743
$\tilde{\dot{M}}_{\rm peak_2}({\rm M_\odot yr^{-1}})$	1.266	1.563	0.519
$\dot{M}_{\rm peak_2}({\rm M_\odot yr^{-1}})$	0.792	0.978	0.325
$\Delta t_{\rm peak}({\rm d})$	/	/	50
$\Delta\dot{M}_{\rm peak}({\rm M_\odot d^{-1}})$	/	/	10^{-3}

through the relation

$$\dot{M}_{\rm peak} \sim \frac{2}{3}\frac{M_{\rm bound_{BH}}}{t_{\rm peak}}. \tag{5.18}$$

Values for stars on parabolic orbits, $\tilde{\dot{M}}_{\rm peak}$ (1,2), can be evaluated considering $M_{\rm bound_{BH}}$ to be half the mass lost from each star (e.g. Rees 1988) and $t_{\rm peak} \equiv \tilde{t}_{\rm peak}$. Corrected values require $M_{\rm bound_{BH}}$ as inferred from simulations and $t_{\rm peak}$ from Equation 5.17. Given that standard assumptions work for $\beta \sim 1$, $\tilde{\dot{M}}_{\rm peak}$ (1,2) and $\dot{M}_{\rm peak}$ (1,2) were estimated as just mentioned for simulation HEp100 (see section 5.4.1), and then they were converted in the corresponding values for the other two simulations, based on the dependence of $\dot{M}_{\rm peak}$ from the impact parameter β reported in Guillochon & Ramirez-Ruiz (2013; 2015a). Indeed, the only difference among simulations is the value of the pericentre radius, i.e. β [1]. However, it must be recalled that the relation between $\dot{M}_{\rm peak}$ and β works for parabolic orbits. Consequently, some differences between the values assessed from the inferred light curves (Figure 5.4) and the analytical estimates are to be expected. Values of $\tilde{\dot{M}}_{\rm peak}$ (1,2) and $\dot{M}_{\rm peak}$ for the three simulations are reported in Table 5.6. Good agreement was found between light curve parameters inferred from Figure 5.4 and analytical evaluations, motivating the recipe followed in the aim to derive tidal disruption light curves.

As previously said in this section, the composite light curves associated with double tidal disruptions were obtained by summing the light curves associated with the disruption of the single binary components. Given that the binary components have different returning and rising times, one should expect to observe a double peak in their composite light curve. In Table 5.6, where possible, the values of $\Delta t_{\rm peak}$

[1] In case of unequal-mass binaries, also the dependence of $\dot{M}_{\rm peak}$ from M_* and R_* needed to be considered.

and $\Delta\dot{M}_{\rm peak}$ as inferred from Figure 5.4 are collected, which are the differences in rise times and accretion rate peaks between the two "humps" in the composite light curves. From Table 5.6 and Figure 5.4, it can be seen that only in simulation HEp143, which corresponds to a grazing encounter, the composite light curve shows not exactly a double peak, as predicted, but anyway a knee. In this case, the single-star light curves are distinguishable enough to be both glimpsed in the composite light curve. As shown in hydrodynamical simulations of single tidal disruptions of Guillochon & Ramirez-Ruiz (2013; 2015a), grazing encounters give rise to steep light curves (i.e. steeper than $-5/3$) immediately after the peak and, in the context of double disruptions, this favours the visibility of the knee in the composite light curves. Therefore, in case of double tidal disruptions of equal-mass binaries only grazing encounters can produce a knee in the composite light curve.

5.4.3 Double tidal disruption light curves: the case of unequal-mass binaries

What happens in case of deeper encounters if the binary components have unequal masses? Using the same procedure described in section 5.4.2, three high-resolution SPH simulations of unequal-mass binaries on parabolic orbits around a BH ($M_{\rm BH} = 10^6{\rm M}_\odot$) were carried on and analysed (HU runs). Table 5.7 collects the outcomes of these simulations as a function of $a_{\rm bin}$ and $r_{\rm p}$. Also the correspondent low-resolution SPH simulations (LU runs) were performed, respectively denoted as LU1, LU2 and LU3, finding out the same outcomes and the same orbital evolution of the binary components (Figure 5.1, bottom panels).

In particular, simulations LU1/HUp42 consider: $M_1 = 0.4{\rm M}_\odot$, $r_{\rm t_1} \sim 65.2{\rm R}_\odot$, $M_2 = 0.27{\rm M}_\odot$, $r_{\rm t_2} = 54.3{\rm R}_\odot$, simulations LU2/HUp70a: $M_1 = 0.5{\rm M}_\odot$, $r_{\rm t_1} \sim$

Table 5.7: Same as Table 5.1 for high-resolution simulations involving unequal-mass binaries.

$a_{\rm bin}\backslash r_{\rm p}$ ($\rm R_\odot$)	42.0	70.0
4.9	HUp42: TD-TDE	HUp70a: P&T-TDE HUp70b: P&T-TDE

$72.4\rm R_\odot$, $M_2 = 1\rm M_\odot$, $r_{\rm t_2} = 100.0\rm R_\odot$, simulations LU3/HUp70b: $M_1 = 1.\rm M_\odot$, $r_{\rm t_1} \sim 100.\rm R_\odot$, $M_2 = 0.5\rm M_\odot$, $r_{\rm t_2} = 72.4\rm R_\odot$. The initial conditions of simulations LU1/HUp42 are those considered in Mandel & Levin (2015). With simulations HUp70a and HUp70b, the dependence of the visibility of a double peak on the mass difference between the binary components and on the mass of the captured star, whether it is the less or the more massive of the two, was explored. Indeed, simulations HUp70a and HUp70b only differ in that they are out of phase by $180°$. In the high-resolution regime, stars denoted as 1, which remained bound to the BH after binary separation, were modelled respectively with 4×10^4, 10^5 and 2×10^5 particles, stars 2, which unbound from the BH, with 2.7×10^4, 2×10^5 and 10^5 particles. Figure 5.5 shows a zoom in the SPH particle density (in log scale), projected in the (x, y) plane, at $t = 0.0034\rm yr$ ($\sim 1.2\rm d$) after pericentre passage for simulations HUp70a and HUp70b. The remnant less massive star is clearly visible in both the simulations.

Table 5.8 collects the characteristic parameters of the light curves inferred from simulations HUp42, HUp70a and HUp70b, respectively, as analytically estimated following section 5.4.2. Figure 5.6 shows single-star and composite light curves inferred from simulations HUp42, HUp70a and HUp70b following the recipe

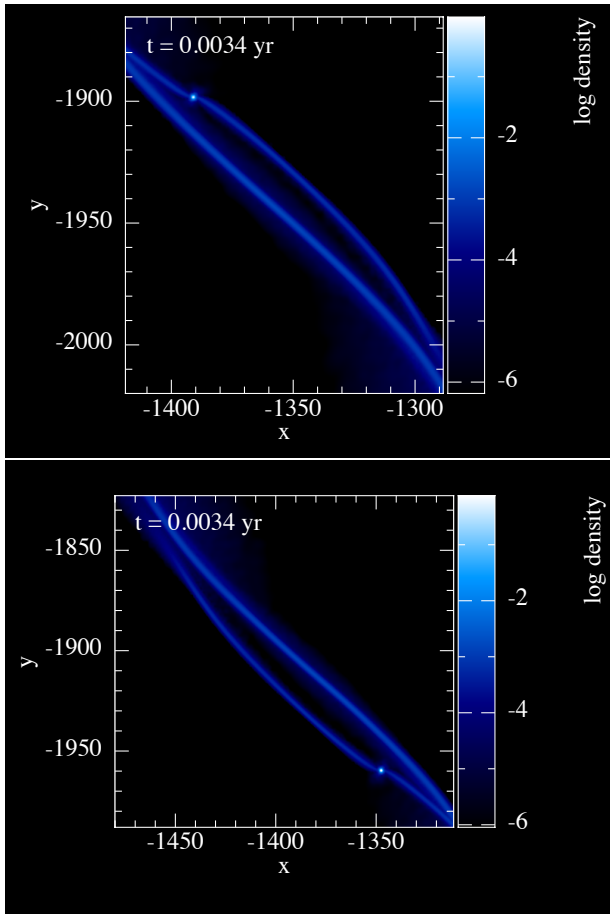

Figure 5.5: Zoom in the SPH particle density (in log scale) for simulations HUp70a (upper panel) and HUp70b (bottom panel), projected in the (x, y) plane, at $t = 0.0034\mathrm{yr}$ ($\sim 1.2\mathrm{d}$) after pericentre passage. The remnant less massive star is clearly visible in both the simulations.

Table 5.8: Same as Table 5.6 for simulations HUp42, HUp70a and HUp70b.

	HUp42: TD-TDE	HUp70a: P&T-TDE	HUp70b: P&T-TDE
$\tilde{t}_{\mathrm{min}_1}(\mathrm{yr})$	0.0937	0.0980	0.1126
$t_{\mathrm{min}_1}(\mathrm{yr})$	0.0845	0.0760	0.1019
$\tilde{t}_{\mathrm{min}_2}(\mathrm{yr})$	0.0866	0.1126	0.0980
$t_{\mathrm{min}_2}(\mathrm{yr})$	0.1224	0.1355	0.1802
$\tilde{t}_{\mathrm{peak}_1}(\mathrm{yr})$	0.1433	0.1417	0.1696
$t_{\mathrm{peak}_1}(\mathrm{yr})$	0.1293	0.1099	0.1536
$\tilde{t}_{\mathrm{peak}_2}(\mathrm{yr})$	0.1272	0.1682	0.1408
$t_{\mathrm{peak}_2}(\mathrm{yr})$	0.1797	0.2025	0.2589
$\tilde{\dot{M}}_{\mathrm{peak}_1}(\mathrm{M}_\odot\mathrm{yr}^{-1})$	0.738	0.987	1.622
$\dot{M}_{\mathrm{peak}_1}(\mathrm{M}_\odot\mathrm{yr}^{-1})$	0.922	1.431	2.025
$\tilde{\dot{M}}_{\mathrm{peak}_2}(\mathrm{M}_\odot\mathrm{yr}^{-1})$	0.574	1.579	0.952
$\dot{M}_{\mathrm{peak}_2}(\mathrm{M}_\odot\mathrm{yr}^{-1})$	0.360	0.988	0.442
$\Delta t_{\mathrm{peak}}(\mathrm{d})$	/	25	/
$\Delta\dot{M}_{\mathrm{peak}}(\mathrm{M}_\odot\mathrm{d}^{-1})$	/	1.5×10^{-3}	/

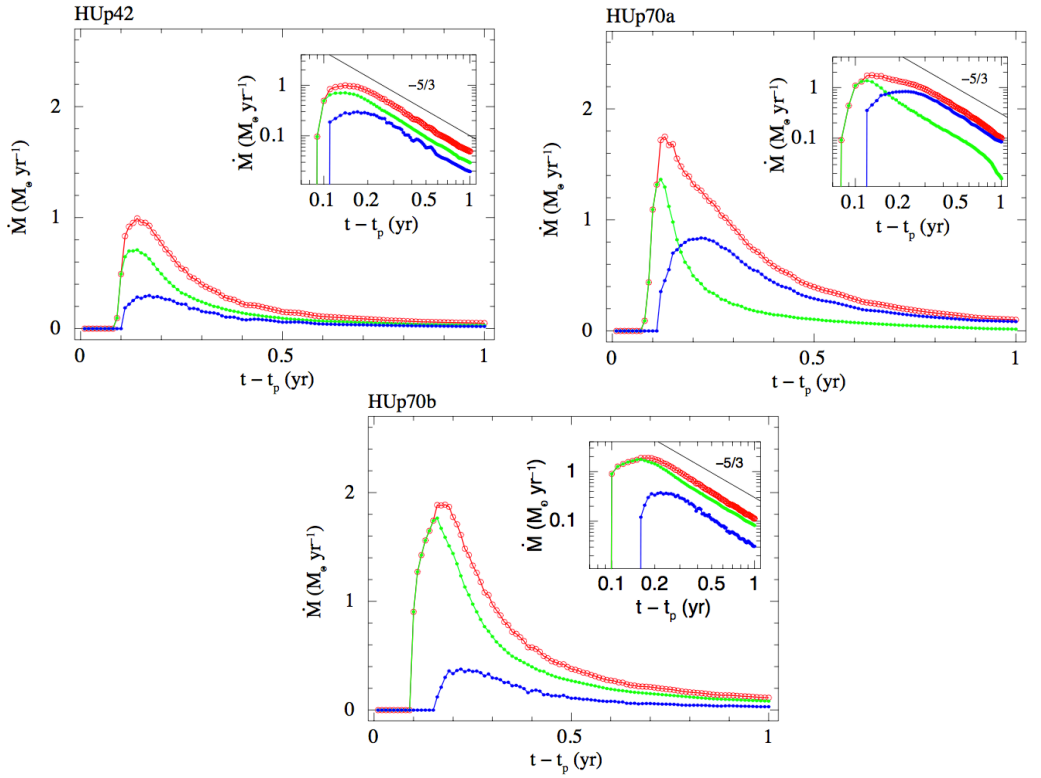

Figure 5.6: Light curves ($\dot{M}$ vs time; see Equation 5.12) inferred from the high-resolution simulations HUp42, HUp70a and HUp70b. Green and blue curves are associated with single-star disruptions, the composite light curves are the red ones. On the right top corners the same plots are shown in logarithmic scale. A knee in the composite light curve is visible in simulation HUp70a.

described in section 5.4.2. Not exactly a double peak, but a knee in the composite light curve is observed when the mass difference between the two stars is increased and when the star which gets bound to the BH is the less massive of the two (simulation HUp70a). This is because a low-mass star is less compact than a higher-mass star (the compactness parameter is $\propto M_*/R_*$), and this leads to an increased difference between the narrow peak of the low-mass star light curve and the broader peak of the higher-mass star light curve.

5.5 Summary and main conclusions

A stellar tidal disruption occurs when a star passes close enough to the central BH of a galaxy to experience the BH tidal field. The star can be fully or partially torn apart, according to the distance of closest approach (Guillochon & Ramirez-Ruiz 2013). The stellar debris which accrete onto the BH power a long-lasting single flare (e.g. Rees 1988; Phinney 1989) or even periodic flares, if the star, partially disrupted, keeps on orbiting around the BH (MacLeod et al. 2013). Such events contribute to detect otherwise quiescent BHs of masses complementary to that probed in bright AGN and QSO surveys (e.g. Vestergaard & Osmer 2009).

Given the high number of field stars in binary systems (e.g. Duquennoy & Mayor 1991; Fischer & Marcy 1992), encounters with a galactic central BH can involve stellar binaries instead of single stars. Despite the high central densities and velocity dispersions in galactic nuclei surely reduce the number of binaries, hard binaries survive. Both the members of these binaries, under certain conditions, when approaching the central BH can experience total or partial tidal disruption immediately after the tidal binary break-up. From an encounter of this kind, a double-peaked flare is expected to blaze up (Mandel & Levin 2015). Generally, after binary break-up one star leaves the system while the other binds to the BH (e.g. Antonini et al. 2011). In the case of partial double disruptions, the bound star can be thus repeatedly disrupted, lighting up periodic ($\sim 1 \div 10$ yr) single-peaked flares. Hence, this channel could be one of the most likely mechanisms that allow stars to become bound to central galactic BHs and undergo periodic tidal disruptions, as suggested for IC3599 (Campana et al. 2015). Periodicity increases the chance of observing and modelling tidal disruption flares, and it could be predicted if a

double peak were detected. This is rare but not impossible, given that double tidal disruptions should contribute up to about the 10% of all tidal disruptions.

This is the first work that explores the process of double tidal disruption through hydrodynamical simulations, in the aim at detailing the dynamics of the binary-BH interaction (Figures 5.2, 5.3 and 5.5) and the shape of the outcoming light curve. Based on the results of a set of fourteen low-resolution SPH simulations of parabolic equal-mass binary-BH encounters, the initial conditions of three high-resolution SPH simulations were set in order to explore double tidal disruptions of different intensities. For twin stars of equal masses, a knee, rather than a double peak, in the composite light curve is observed only in the case of grazing double tidal disruptions. Otherwise, flares without knees can be observed, indistinguishably from single-star tidal disruptions (Figure 5.4).

Also, the case of unequal-mass binaries experiencing double tidal disruptions was explored, running three additional high-resolution simulations. The most favourable conditions for the visibility of a knee in the composite light curves occur when the difference in mass between the binary components is increased and the star fated to bind to the BH is lighter than the star fated to leave the system (Figure 5.6). Indeed, the knee becomes more and more defined when the difference in the peak width between the two single-star light curves increases. The less massive star, which is less compact, generates a light curve that is rising and declining on a shorter time scale. Varying the binary semi-major axis, internal eccentricity and internal orbital plane inclination with respect to the orbital plane of the binary centre of mass around the BH affects less the shape of the double tidal disruption light curves. These parameters mainly act on the single-star impact parameters, but even if these ones are different to the maximum degree, they cannot be so much

different, otherwise double tidal disruptions are inhibited.

Starting from the light curve which shows a knee in the case of unequal-mass binaries (Figure 5.6), I estimated analytically how much the light curve would change when changing the BH mass, $M_{\rm BH}$. I considered the interval between $10^5 {\rm M}_\odot$ and $10^8 {\rm M}_\odot$ and followed the dependence on $M_{\rm BH}$ of single times and peak accretion rates as reported by Guillochon & Ramirez-Ruiz (2013; 2015a). I found that $\Delta t_{\rm peak}$ tends to increase whereas $\Delta \dot{M}_{\rm peak}$ tends to decrease increasing $M_{\rm BH}$ to the point that intermediate values of $M_{\rm BH}$ (i.e. $10^6 - 10^7 {\rm M}_\odot$) are more favourable to the observation of the knee in the composite light curve.

It is worth noting that relativistic effects should also be taken into account in future studies on double tidal disruptions, especially in the case of deep encounters, given that they could cause deviations of the debris evolution from the one assumed here.

Chapter 6

The strange case of PS16dtm:

an outsider among tidal disruptions

paper writing in progress...

Chapter 5 introduced and dealt with the so-called double tidal disruptions, i.e. close encounters between stellar binaries and nuclear BHs which lead to the sequential tidal disruption of both the binary components immediately after their tidal separation. The peculiar signature of such events is a double-"humped" accretion flare, which however is not always clearly visible: indeed, the flare that lights up from a double tidal disruption is often totally indistinguishable from the single-peaked flares associated with single-star tidal disruptions. Up to now, no candidate double tidal disruptions have ever been identified, partly because, as just said, their associated flares are often identical to single-star tidal disruption flares, and partly because they are quite rare events (about the 10% of all tidal disruptions; see chapter 5).

During the last months of my PhD, I read about PS16dtm (Blanchard et al. 2017), a bright transient located at the centre of a narrow-line Seyfert 1 galaxy, which was classified as a single-star tidal disruption event. The anomaly in such a

classification were the two "humps" clearly visible in the bolometric light curve of the transient, which induced me to consider the hypothesis of PS16dtm as a double tidal disruption event. Section 6.1 of this chapter describes the transient main features and its tidal disruption nature. The likely identification of PS16dtm as a double tidal disruption event is presented in sections 6.2 and 6.3. Specifically, this interpretation was investigated through high-resolution hydrodynamical simulations. Before PS16dtm, the bright, double-"humped" transient ASASSN-15lh caught my attention (e.g. Margutti et al. 2017; see also chapter 2). Even if classified as a possible single-star tidal disruption event, it showed two prominent "humps" in its bolometric light curve, more prominent than PS16dtm. I carried out an explorative search in order to model this bolometric light curve. I explored with high-resolution hydrodynamical simulations of double tidal disruptions different binary masses, orbital separations and BH masses but no data set was found that could even remotely shape this curve. The detection and recognition of double tidal disruption flares should open the way for the prediction, follow-up and modelling of subsequent periodic single-star tidal disruptions, involving the binary component which binds to the BH after the tidal binary break-up (e.g. Antonini et al. 2011). This and other main conclusions are inspected in section 6.4.

6.1 The current interpretation of PS16dtm

The host galaxy of the nuclear transient PS16dtm, SDSS J015804.75-005221.8 ($z = 0.0804$), was classified as a narrow-line Seyfert 1 (NLS1) galaxy (e.g. Osterbrock & Pogge 1985), based on a pre-outburst spectrum dominated by multi-component Balmer emission lines and on its radio-to-X-ray and optical-to-X-ray luminosity ratios (e.g. Terashima & Wilson 2003; Grupe et al. 2004). It was detected in the

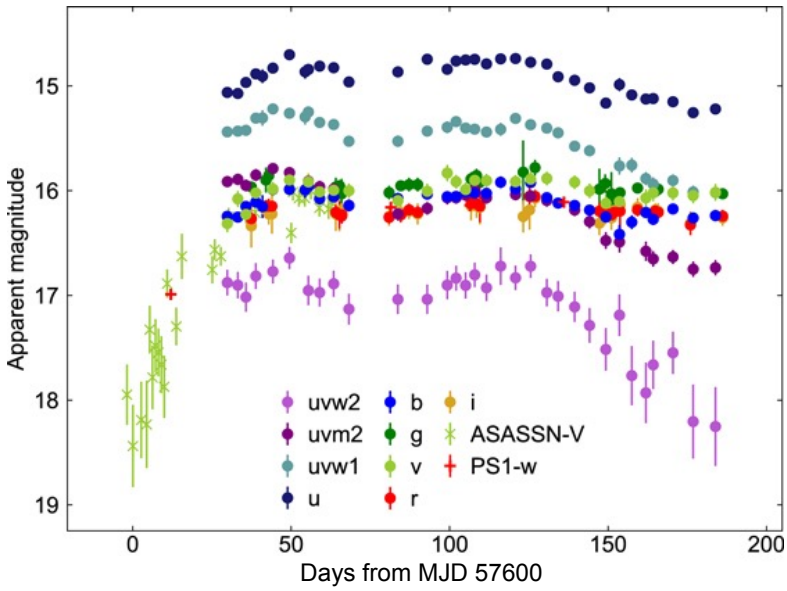

Figure 6.1: Host-subtracted UV/optical light curves of PS16dtm (corrected for Galactic extinction) as reported in Blanchard et al. (2017).

X-rays with $L_{\rm X} \sim 0.01 L_{\rm Edd}$ for a BH of $10^6 {\rm M}_\odot$ (Blanchard et al. 2017). The host historical optical light curve showed only mild variability until August, 2016, when a significant brightening (RA(J2000)=01:58:04.74, DEC(J2000)=-00:52:21.7) was discovered independently by the Pan-STARRS Survey for Transients (PSST), the Catalina Real-time Transient Survey (CRTS), and the All-Sky Automated Survey for Supernovae (ASAS-SN; e.g. Smith et al. 2016; Dong et al. 2016a). Indeed, follow-up UV/optical observations revealed a rise over ~ 50 days, a successive small decline over ~ 30 days and then a new rise with evidence for only another modest decline (Figure 6.1). On the contrary, during such brightenings the X-ray emission dropped by a factor of ~ 10: no X-ray emission associable to PS16dtm was detected, or rather, during its UV/optical lighting up, the X-ray emission previously coming from the host galaxy dropped considerably. The bolometric

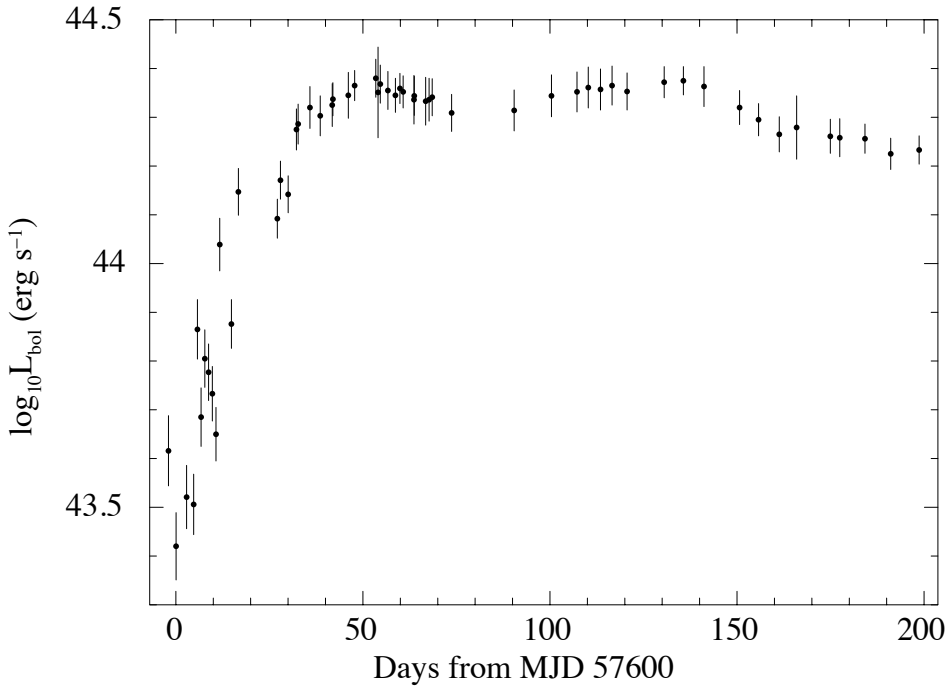

Figure 6.2: Bolometric light curve of PS16dtm as appeared in Blanchard et al. (2017). It lights up to something above 10^{44} erg s^{-1} on ~ 50 days and then it shows only a small decline and new rise before starting to drop slowly.

emission of the transient event thus came out to peak at ~ 50 days with $\sim 2.2 \times 10^{44}$ erg s^{-1}, that is, around the Eddington luminosity for a BH of $10^6 M_\odot$ and about 100 times larger than the pre-outburst luminosity of the host galaxy. This emission then remained roughly constant for ~ 100 days, showing only a small dimming and rebrightening, before starting to slowly drop (Blanchard et al. 2017; Figure 6.2). As far as concerning the spectra of the transient, it was revealed a dominance of multi-component Balmer lines and strong FeII lines, resembling the spectra of NLS1 galaxies (Blanchard et al. 2017).

Based on the even little-evolving spectral properties of PS16dtm, together with

its unusual light curve and its almost-constant high temperature ($\sim 1.7 \times 10^4$ K) during all the "plateau" phase (Figure 6.2), Blanchard et al. (2017) ruled out a supernova interpretation for the transient. Conversely, the resemblance of PS16dtm spectra to those of NLS1 galaxies, the similarity of the PS16dtm bolometric luminosity peak to the Eddington luminosity of the massive BH at the centre of its host galaxy, and the coincidence of the transient event with the nucleus of its host galaxy suggest PS16dtm to be related to the central BH, although AGN activity can not justify some source properties (e.g. its high and rapid brightening, the drop in X-ray emission).

The interpretation of PS16dtm as a stellar tidal disruption event, as reported in Blanchard et al. (2017), seems to be the best in explaining its features: the location coinciding with the centre of the host galaxy, the high ($L_{\mathrm{bol}_{\mathrm{peak}}} \sim L_{\mathrm{Edd}}$, $M_{\mathrm{BH}} = 10^6 \mathrm{M}_\odot$) and rapid lighting, the little evolution over time of the spectra (the spectral lines associated with the stellar tidal disruption could be blended with the host galaxy features), and also the drop in the X-ray emission, given that the produced stellar debris can obscure the X-ray-emitting region of the pre-existing disc in the active host galaxy while powering the UV/optical emission. However, the two (even if mild) "humps" appearing in the bolometric light curve of the transient (Figure 6.2) are not straightforward to be interpreted based on the theory of single-star tidal disruptions, and the work here presented starts up exactly from here.

6.2 One hump for one star, one star for each hump

The first thing that jumped to my eye when I read about PS16dtm (Blanchard et al. 2017) was the similarity between its bolometric light curve and the curves expected

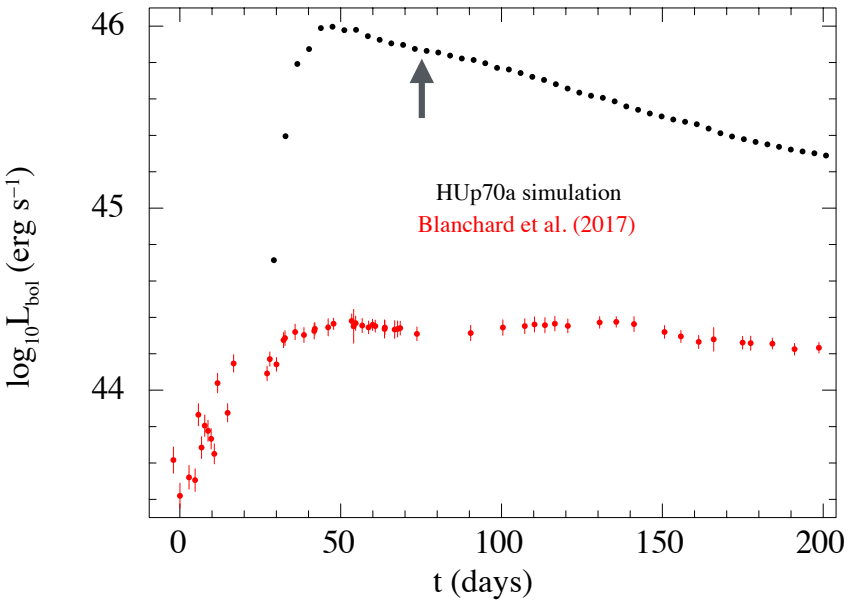

Figure 6.3: Comparison between the composite light curve inferred from simulation HUp70a in chapter 5 ($\eta = 0.1$) and the bolometric light curve of PS16dtm (Blanchard et al. 2017). t is the time since disruption (i.e. roughly the time since pericentre passage) for simulation HUp70a and the time since MJD 57600 for PS16dtm.

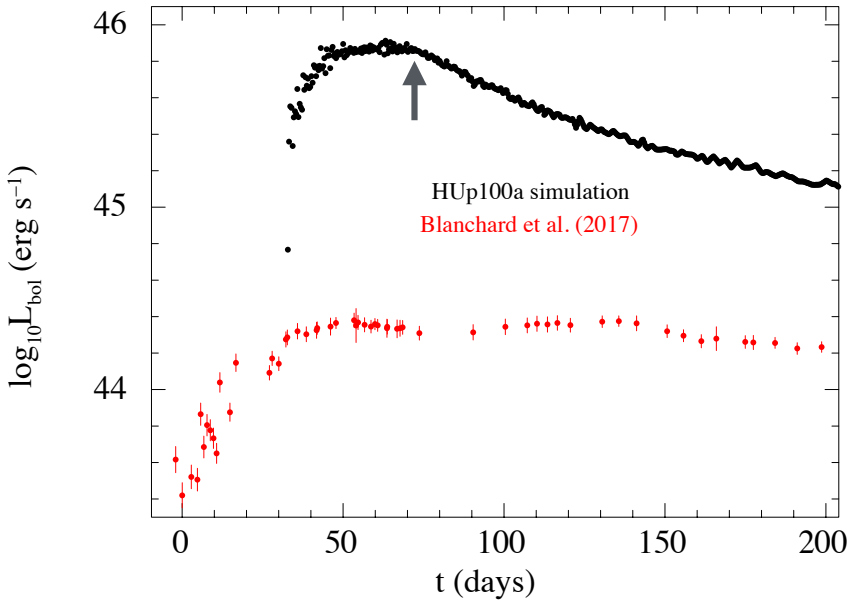

Figure 6.4: Same as Figure 6.3 with simulation HUp100a ($r_{\rm p} \sim 100 {\rm R}_{\odot}$) instead of simulation HUp70a ($r_{\rm p} \sim 70 {\rm R}_{\odot}$).

for double tidal disruptions, as described in the previous chapter. Let's start from the composite curve inferred from simulation HUp70a (Figure 5.6; chapter 5). Such a simulation reproduced a close ($r_{\rm p} \sim 70 {\rm R}_{\odot}$) parabolic encounter between an unequal-mass circular binary ($0.5 {\rm M}_{\odot}$ and $1 {\rm M}_{\odot}$; $a_{\rm bin} \sim 5 {\rm R}_{\odot}$) and a massive BH ($10^6 {\rm M}_{\odot}$) in the Newtonian regime, which led to the sequential tidal disruption of both the binary components immediately after the tidal binary break-up. The least massive star ended up to get bound to the BH, while the solar-mass star was placed on an hyperbolic orbit. The composite curve of the rate of stellar debris returning to pericentre, assumed to coincide for simplicity with the rate of material accreting onto the BH, shows a sort of knee (Figure 6.3, grey arrow), which was analytically estimated to be more pronounced for a slightly more massive BH.

Figure 6.3 shows a direct comparison between the composite light curve inferred from this simulation (assuming a radiative efficiency $\eta = 0.1$ in Equation 5.12) and the bolometric light curve of PS16dtm (Figure 6.2). Apart from clear differences in peak luminosities, the curve associated with the simulation can not (even approximately) model PS16dtm bolometric light curve. The same analysis was performed also by changing the pericentre distance of the binary centre of mass from the BH in the simulation ($r_{\rm p} \sim 100 {\rm R}_{\odot}$; HUp100a), and similar conclusions can be drawn (Figure 6.4).

In the attempt to reproduce the bolometric light curve of PS16dtm through a double tidal disruption, a further simulation was performed using the GADGET2 code (Springel 2005; see sections 4.1, 4.2 and 5.2 for details on SPH simulations and GADGET2). The binary components were modelled as $\gamma = 5/3$ polytropes, of masses $0.5 {\rm M}_{\odot}$ and $1 {\rm M}_{\odot}$ and radii given by Equation 5.10, and sampled with respectively $\sim 5 \times 10^4$ and $\sim 10^5$ particles, disposed in accordance with the required density profile after being placed with a close sphere packing. The semi-major axis $a_{\rm bin}$ and the internal eccentricity $e_{\rm bin}$ of the binary were fixed at $5 {\rm R}_{\odot}$ and 0 (i.e. close and circular binary, as in simulations HUp70a and HUp100a), and the binary centre of mass was initially placed at five times $r_{\rm tb}$ (Equation 1.16) from the BH, in order to avoid spurious tidal distortions, on a parabolic orbit with $r_{\rm p} \sim 195 {\rm R}_{\odot}$. Such a value of $r_{\rm p}$ caused one star (the more massive one, which also became unbound from the BH) to be fully disrupted and the other (which bound to the BH) to be only partially disrupted. The internal orbital plane of the binary was arbitrarily set perpendicular to the orbital plane around the BH. A BH of $10^7 {\rm M}_{\odot}$ (instead of $10^6 {\rm M}_{\odot}$) was implemented through a Newtonian analytical potential, based on what previously said about the dependence from $M_{\rm BH}$ of the visibility of the knee in the

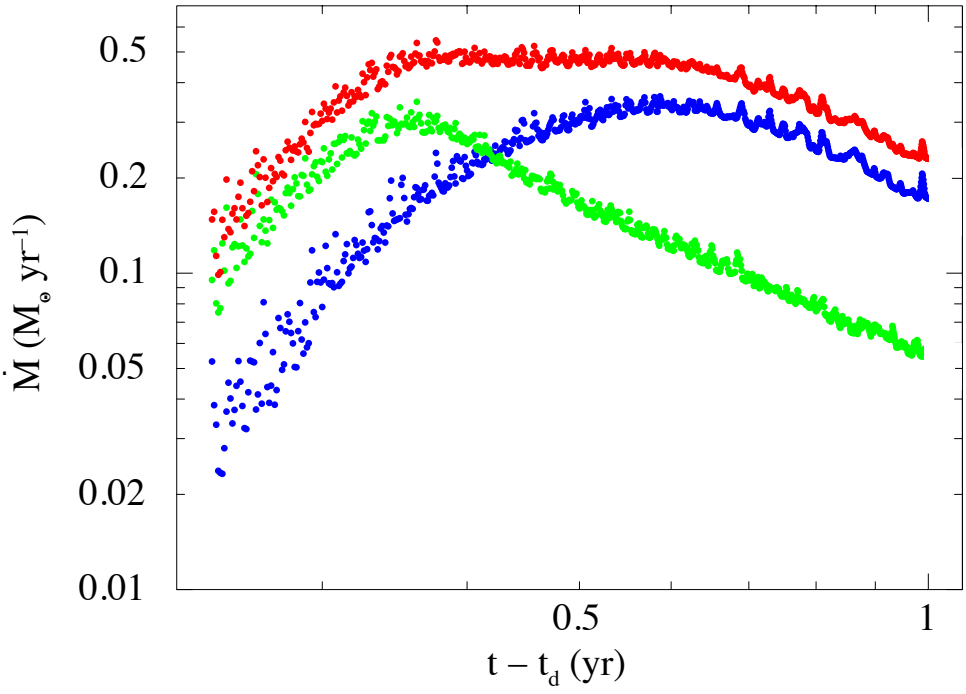

Figure 6.5: Single-star (green and blue curves) and composite (red curve) evolution near peak, in logarithmic scale, of the rate of stellar material returning to pericentre after tidal disruption, inferred from the last GADGET2 simulation described in the main text. $t - t_{\rm d}$ on the x-axis is the time since disruption (i.e. roughly pericentre passage).

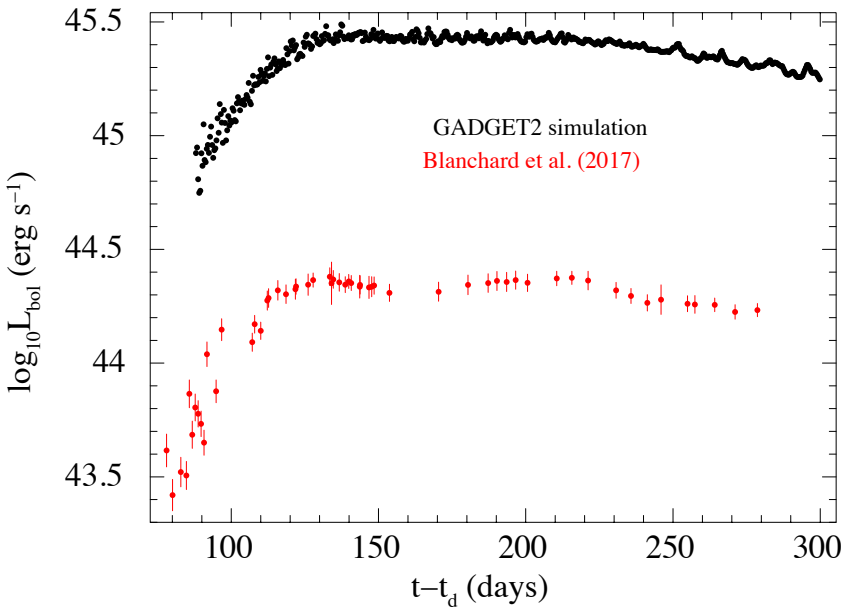

Figure 6.6: Same as Figure 6.3 with the last GADGET2 simulation described in the main text. The bolometric light curve of PS16dtm was rescaled to the time since disruption $t_{\rm d}$ of the simulation.

composite curve of a double tidal disruption event. The composite curve of the rate of stellar debris returning to pericentre (Figure 6.5, red curve) was built following the recipe described in section 5.4.2, but replacing the second term in Equation 5.13 with the stellar gravitational potential directly computed by the simulation code (even if it was demonstrated that this does not change significantly the results).

Figure 6.6 shows a comparison between the composite light curve inferred from this simulation with $\eta = 0.1$ (Equation 5.12) and the bolometric light curve of PS16dtm. The latter was rescaled to the time since disruption of the simulation. The peak luminosity inferred from the simulation results to be about two times the Eddington luminosity for a BH of $10^7 \mathrm{M}_\odot$. Forgetting for a moment the differences in the peak luminosities, the shape of the composite light curve inferred from the GADGET2 simulation resembles to a good approximation that of PS16dtm bolometric light curve. In order to match PS16dtm curve, a radiative efficiency of 0.008 would be needed (Figure 6.7).

Based on the whole of this, and in particular on the results summarised in Figure 6.7, I am increasingly convinced to interpret PS16dtm as the sequential tidal disruption of the two members of a stellar binary by a massive BH. In the next section I will discuss more in detail such an interpretation.

6.3 The first double tidal disruption candidate

So far, no transient has ever been classified as a double tidal disruption event, and PS16dtm could be the first member of this new class. Such an interpretation for PS16dtm justifies some of its features, which however could also be explained by a single-star tidal disruption event, such as the coincidence with the nucleus of its host galaxy, its high and rapid brightening, its high temperature. Moreover,

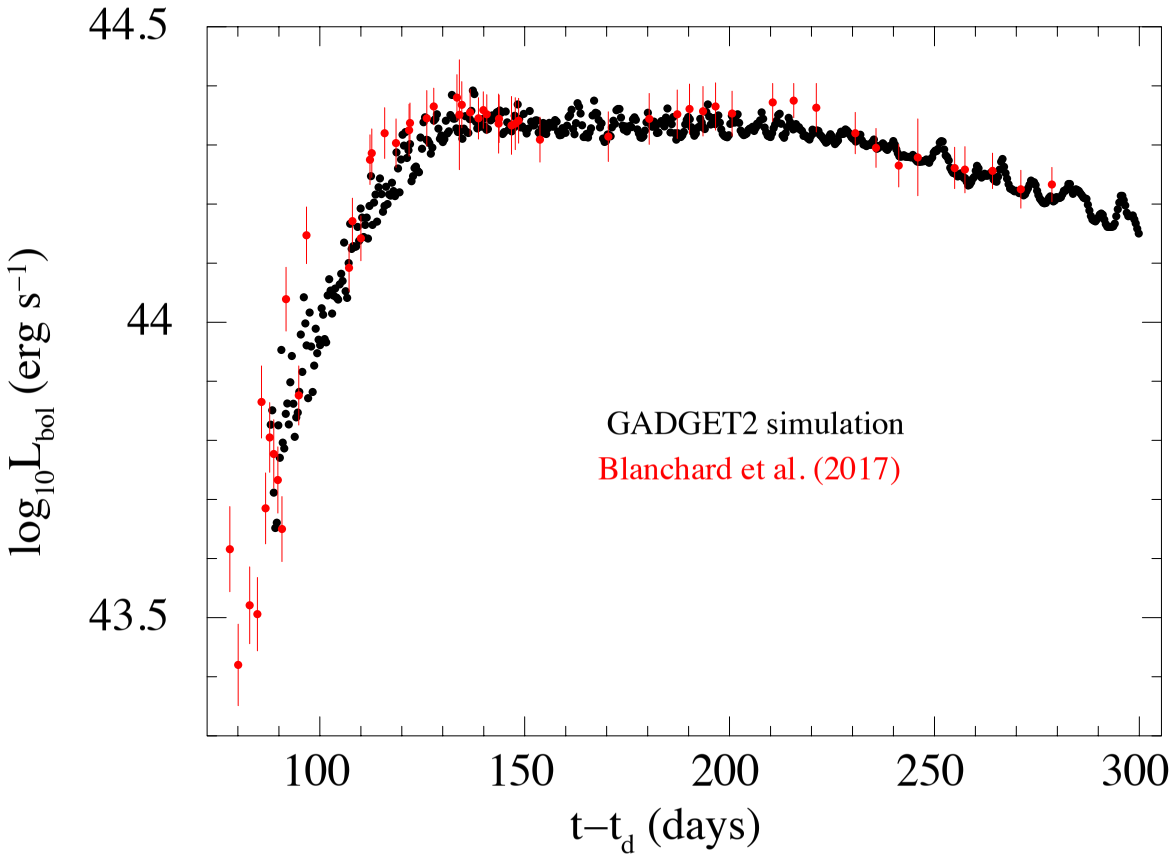

Figure 6.7: Same as Figure 6.6 with $\eta = 0.008$ in the inference of the composite light curve from the last GADGET2 simulation described in the main text.

the only slight temporal evolution of its NLS1-like spectrum and the drop in its X-ray emission are linkable to both a double or a single-star tidal disruption event occurring in an active galaxy. The great peculiarity of PS16dtm as a single-star tidal disruption event are the two "humps" that characterise its bolometric light curve (Figure 6.2), which seem to be more naturally associated with a double tidal disruption event (section 6.2).

The last GADGET2 simulation described in the previous section, whose inferred composite light curve came out to properly model the bolometric light curve of PS16dtm, involves a close and circular unequal-mass binary and a BH of $M_{\rm BH} = 10^7 {\rm M}_\odot$. The latter is something more massive than estimated for PS16dtm host galaxy (e.g. Blanchard et al. 2017), but both the estimates of BH masses from the spectra of their galaxies are rather approximate and the main goal of this work is not to find the true value of $M_{\rm BH}$ but only its order of magnitude. Furthermore, the composite light curve inferred from the simulation would stand for the accretion light curve associated with the binary-BH simulated encounter, given the recipe adopted in building it, but the accretion rate onto the BH may not match exactly the rate of stellar debris returning to pericentre, thus also influencing the resulting accretion luminosity. Also, the accretion disc emission typically lies in the UV/optical band (where PS16dtm was mainly detected) only after being reprocessed. But, if the disc were optically thin, geometrically thick and advection-dominated, its radiative efficiency could be very low and it could emit mainly at UV/optical wavelengths (e.g. Narayan 2004). This could explain, at least partially, the need of choosing a very low value of $\eta = 0.008$ (Figure 6.7).

6.4 Summary and main conclusions

A new category of tidal disruption events is catching on, involving close stellar binaries instead of single stars (e.g. Mandel & Levin 2015). Under certain conditions, when a binary approaches the central BH of a galaxy, both its stellar components are tidally disrupted in sequence, immediately after their tidal separation. Such events are usually known as double tidal disruptions and their representative signature is expected to be a double-"humped" accretion flare. However, it is neither easy nor common to identify double tidal disruptions, given that their associated accretion flares seem to be often single-peaked, just like in the case of single-star tidal disruptions, and their percentage of occurrence is only about the 10% of all tidal disruption events (chapter 5). Identifying double tidal disruption events would mean to be able to predict subsequent periodic single-star tidal disruptions: indeed, after the binary break-up, generally only one binary component binds to the BH (e.g. Antonini et al. 2011) and, if only partially destroyed during the double tidal disruption, it could be repeatedly disrupted over multiple orbits around the BH, lighting up better modellable recurrent single-peaked accretion flares.

No candidate double tidal disruption had ever been identified before PS16dtm, a UV/optical luminous transient discovered on August, 2016 at the centre of a narrow-line Seyfert 1 galaxy, till now classified as a single-star tidal disruption event (Blanchard et al. 2017). The two "humps" clearly visible in its bolometric light curve (Figure 6.2) led me to investigate the hypothesis of a double tidal disruption event. Through high-resolution GADGET2 hydrodynamical simulations of Newtonian close binary-BH parabolic encounters, PS16dtm was associated with a double tidal disruption of a close unequal-mass binary by a BH of $10^7 \mathrm{M}_\odot$ (Figure

6.7), ending up with the total ripping apart of the more massive star and the partial stripping of the less massive star, which also became bound to the BH, thus maybe undergoing another tidal disruption in the next future. Surely, the simulated double tidal disruption will not be the only one which resembles the bolometric light curve of PS16dtm, but it is one solution that could explain PS16dtm. General relativistic effects would somehow influence the parameters of the encounter, but this is beyond the aim of this work. In the context of PS16dtm, it is worth mentioning the interpretation that Leloudas et al. (2016) gave to the emission coming from the double-"humped" transient ASASSN-15lh. They interpret this source as a single-star tidal disruption event and associate the two peaks that characterise ASASSN-15lh light curve with debris circularisation and accretion onto the BH, respectively. For these two peaks to be so far, the circularisation time must be much smaller than the accretion time. This could happen under the influence of general relativistic effects, close to a highly massive ($\sim 10^8 \mathrm{M}_\odot$), rapidly spinning BH. For PS16dtm this would mean considering a BH about 10^2 times more massive than estimated by Blanchard et al. (2017).

The host galaxy of PS16dtm is active. Tidal disruption events in active galaxies would be more difficult to be revealed because of the higher overall emission (e.g. Komossa 2012), but active galaxies are predicted to host more tidal disruption events due to the perturbing presence of the pre-existing disc (e.g. Karas & Šubr 2007). Also IC3599 was classified as a tidal disruption event occurring in an active galaxy (Campana et al. 2015). Specifically, this consists of recurrent partial tidal disruptions of a single star on a bound orbit around the central BH. And one of the mechanisms that could explain the origin of the periodically stripped star is exactly the double tidal disruption.

Chapter 7

The past, the present, the future: concluding remarks

Massive black holes (MBHs) live at the centre of most galaxies (e.g. Kormendy & Richstone 1995; Kormendy & Gebhardt 2001). When accreting much matter, they emit huge amounts of energy, becoming bright active galactic nuclei (AGNs), though typically AGNs have short duty cycles and are in a low-luminosity state most of the time (Ho 2008). The brightening up of the central BH of a galaxy can also be powered by the tidal disruption of a star wandering around it (Rees 1988). Indeed, a star in the galactic nuclear star cluster can be scattered very close to the BH by dynamical mechanisms (section 1.1), thus strongly experiencing its tidal field (Alexander 2012; Merritt 2013). As the stellar self-gravity fails in resisting the BH tidal force, the star is disrupted (Hills 1975). A fraction of the produced stellar debris binds to the BH (e.g. Lacy et al. 1982; section 1.2, Figure 1.3), circularises and accretes onto it (section 1.3), powering a characteristic emission (e.g. Rees 1988; Phinney 1989; Lodato & Rossi 2011; Guillochon & Ramirez-Ruiz 2015b;

Piran et al. 2015; section 1.4).

In the case of rapid debris circularisation into an accretion disc around the BH and small accretion time (e.g. Ulmer 1999), the resulting bolometric accretion luminosity evolves in time, to a good approximation, following a power law of index $-5/3$ after peak (Equation 1.24; e.g. Evans & Kochanek 1989), even though its early trend depends on the stellar internal structure and the intensity of the disruption (Lodato et al. 2009; Guillochon & Ramirez-Ruiz 2013; 2015a). The bulk of the accretion luminosity is expected to lie in the UV/soft X-ray energy band (e.g. Lodato & Rossi 2011), with a possible optical/UV observed contribution if it gets reprocessed. When its peak significantly exceeds the Eddington luminosity of the BH, at early times a fraction of the accreting debris is probably ejected in a wind, which is associated to an optical/UV emission (e.g. Strubbe & Quataert 2009; Lodato & Rossi 2011). In the case of slow debris circularisation (Guillochon & Ramirez-Ruiz 2015b; Hayasaki et al. 2016), the accretion emission is delayed or even slowed down and lowered for a long accretion time (Shiokawa et al. 2015). In this latter case, the main observed emission is likely to come from the circularisation phase and lies in the optical energy band (Piran et al. 2015; Wevers et al. 2017).

Tidal disruption events provide a unique way to detect otherwise quiescent BHs in a mass interval somewhat complementary to that probed in surveys of bright AGNs (Vestergaard & Osmer 2009). Considering solar-mass stars, (non-rotating) BHs of mass lower than about $10^8 \mathrm{M}_\odot$ can be revealed from the observation of tidal disruption flares (Equation 1.17). To date, about 70 candidates have been identified (https://tde.space; Auchettl et al. 2017; chapter 2), mainly in the optical, UV and soft X-rays, but also at radio and hard X-ray wavelengths thanks to the launching of accretion-powered relativistic jets (e.g. Bloom et al. 2011; Cenko et

al. 2012b; Brown et al. 2015). This is a rather small number, but with the advent of new telescopes such as LSST and ZTF, together with Pan-STARRS and ASAS-SN, coupled with the numerous theoretical studies carried out on tidal disruption events (e.g. see references in chapter 1), more and more candidates are fated to be discovered.

A couple of years ago, I studied XMMSL1J063045.9-603110 adding this source to the tidal disruption candidate list (chapter 3; Mainetti et al. 2016a). This transient source was detected to be bright in the soft X-rays during an *XMM-Newton* slew and later showed an X-ray flux decay by a factor of about 10 in twenty days. Following *XMM-Newton* and *Swift* X-ray observations revealed an approximately $-5/3$ power law X-ray flux decay over time by a factor of about 115 in a month and a half (Figure 3.3), an X-ray spectrum representative of a thermal accretion disc (Figure 3.2) and also a temperature decrease (section 3.4). Also, at about the same time, a possible counterpart blazed up at lower energies (Figure 3.1). Optical observations (Figure 3.4) testify that XMMSL1J063045.9-603110 is probably associated with an extremely dim and small galaxy or even a very bright globular cluster with an intermediate-mass BH at its centre, though deep spectroscopic observations are needed to provide more information. To date, very few tidal disruption candidates have been associated to dwarf galaxies hosting intermediate-mass BHs (e.g. Ghosh et al. 2006; Maksym et al. 2013; 2014a; 2014b; Donato et al. 2014), and the discovery of new members of this class could bring towards the confirmation of the existence of intermediate-mass BHs, the connecting bridge between stellar-mass and massive BHs and the likely raw material that makes up MBHs (e.g. Merloni & Heinz 2013; Volonteri 2010).

The literature of tidal disruption events basically deals with the full disruption

of a star when significantly approaching the central BH of a galaxy. However, it could also happen that the BH tidal influence on the star is not strong enough to totally rip it apart, thus leaving a stellar remnant only stripped of its outer material. In these cases, one could speak about partial tidal disruption events (e.g. Guillochon & Ramirez-Ruiz 2013). The demarcation line between the total and the partial tidal disruption of a star orbiting very close to a BH is a critical pericentre distance from the compact object, usually assumed to be the so-called BH tidal radius (Equation 1.1): if $r_{\rm p} < r_{\rm t}$ the star would be fully disrupted, otherwise it would suffer only partial disruption. However, the need to define the effective critical distance where the stellar self-gravity is completely overwhelmed by the BH tidal force (indeed, $r_{\rm t}$ is only the distance where the BH tidal force equates the stellar self-gravity at the stellar surface; e.g. Lacy et al. 1982) induced Guillochon & Ramirez-Ruiz (2013; 2015a) first, and then me (chapter 4; Mainetti et al. 2017), to perform a series of high-resolution hydrodynamical simulations of star-BH Newtonian parabolic encounters, by considering two different internal stellar structures and by changing the orbital pericentre of the star (e.g. Figures 4.2 and 4.3), in order to evaluate for each encounter the fraction of stellar mass loss (section 4.2). The use of different simulation codes (section 4.1) did not significantly influence the results in the case of the least centrally concentrated stars (Figure 4.4, polytropic index $5/3$), while when considering more centrally concentrated stars (Figure 4.5, polytropic index $4/3$) Lagrangian codes came out to better resolve the dynamics of the core with respect to Eulerian codes (section 4.1). For less and more centrally concentrated stars, respectively, the demarcation between total and partial tidal disruptions turned out to lie at $(0.92 \pm 0.02)^{-1} r_{\rm t}$ and $(2.01 \pm 0.01)^{-1} r_{\rm t}$ from the BH. Flares from total and partial tidal disruptions are expected to show a somehow different appearance

(Guillochon & Ramirez-Ruiz 2013; 2015a), so that it might be worthwhile in the near future to perform some high-resolution Lagrangian simulations, as opposed to Eulerian simulations, of stellar disruptions in the aim at getting their associated light curves. This would be a new step in better modelling tidal disruption candidates.

Based on what said, then, a star orbiting very close to the central BH of a galaxy can be totally or partially disrupted by the BH tidal field, lighting up the compact object via gas accretion. This phenomenon can repeat if the star, not fully disrupted, is on a bound orbit (e.g. MacLeod et al. 2013). Because of the multiplicity of stars in binary systems (e.g. Duquennoy & Mayor 1991; Fischer & Marcy 1992), also binary stars may (under certain conditions; section 5.1) experience in pairs tidal disruption, immediately after being tidally separated. The total or partial consumption of both the binary components by the BH is expected to power a characteristic double-peaked accretion flare (Mandel & Levin 2015). Generally, the tidal binary break-up leaves one star bound to the BH and the other unbound (e.g. Antonini et al. 2011), and the former, if only partially disrupted, can be repeatedly disrupted, powering multiple single-peaked accretion flares. Thanks to a series of hydrodynamical simulations of Newtonian double tidal disruptions (chapter 5; sections 5.4.2 and 5.4.3; Mainetti et al. 2016b), I found that accretion flares from them should reveal a more prominent knee, rather than a double peak, when decreasing the strength of the disruption (Figure 5.4) and when elevating the difference between the mass of the star which leaves the system after binary separation and the mass of the companion (Figure 5.6). Moreover, $10^6 - 10^7 \mathrm{M}_\odot$ BHs seem to be more favourable to the observation of such a knee (section 5.5). It is not easy to observationally identify double tidal disruption candidates, given that their associated accretion flares are often single-peaked, as in the case of single-star

tidal disruption events, and they are quite rare events (section 5.1). However, the detection of characteristic double tidal disruption accretion flares can anticipate the possible onset of periodic single-peaked flares, associated with the iterated partial tidal disruption of the binary component which binds to the BH after binary break-up, which can then be predicted, follow-up and better modelled.

The first double tidal disruption candidate ever might be identified in PS16dtm (chapter 6), a bright nuclear transient associated with a narrow-line Seyfert 1 galaxy initially classified as a single-star tidal disruption event (Blanchard et al. 2017). The two "humps" visible in its bolometric light curve (Figure 6.2) drove me to investigate its classification as a double tidal disruption event. Through high-resolution Newtonian hydrodynamical simulations (section 6.2), I identified at least one plausible solution of stellar binary-BH parameters which leads to PS16dtm bolometric light curve: a close circular binary consisting of $0.5\mathrm{M}_{\odot}$ and $1\mathrm{M}_{\odot}$ stars, which were partially and fully disrupted, respectively, by a $10^{7}\mathrm{M}_{\odot}$ BH. The transient observability only at UV/optical wavelengths could also justify the need of a small radiative efficiency (Figure 6.7): indeed, optically thin, geometrically thick and advection-dominated accretion discs typically emit at these wavelengths and have small radiative efficiencies (e.g. Narayan 2004). The significant drop in the host galaxy X-ray emission during the transient UV/optical flare could be interpreted as due to the obscuration of the pre-existing disc in the active galaxy by the stellar debris resulting from the double tidal disruption.

General relativistic effects may influence the stellar debris evolution (section 1.3), and vary it with respect to the Newtonian regime. In the general relativistic regime, stars are expected to spend more time near the BH, where tidal forces are important, and to lose more mass. Stellar debris are likely to be more greatly

spread in orbital specific energies, the first returning time at pericentre of the most bound material is expected to be shorter and the peak of the rate of material returning at pericentre is probably higher. The combination of in- and out-of-plane relativistic precessions, then, sets the debris circularisation around the BH, with the in-plane precession resulting in a more efficient circularisation and the out-of-plane precession delaying it. The debris accretion onto the BH is driven by the viscous time, significantly prolonged in the case of massive and highly spinning BHs. Thus, the outcoming emission is expected to be somehow different than in the Newtonian regime, but hydrodynamical simulations of tidal disruptions also including general relativistic effects are needed to be performed, especially when deep encounters are modelled. Moreover, stars and binaries on elliptical orbits around BHs should be considered, given that the accretion flares arising from their tidal disruption could be somehow different from flares associated with parabolic close encounters.

One of the main perspectives regarding tidal disruption events is the opportunity to identify new tidal disruption candidates, offered by telescopes such as LSST and ZTF. Indeed, for example LSST should allow the observation at lower energies of at least 100 tidal disruption events per year. This will pave the way for monitoring their evolution also at higher energies with facilities such as *XMM-Newton*, *Chandra* and *Swift* and thus modelling and classifying them as total or partial, but also single-star or double, based on their light curves. Posterity will judge.

Bibliography

Abt, H. A., 1983, ARA&A, 21, 343

Abt, H. A. & Levy, S. G., 1976, ApJS, 30, 273

Agertz, O., Moore, B. et al., 2007, MNRAS, 380, 963

Alexander, T., 2012, EPJ Web Conf., 39, 05001

Alexander, K. D., Berger, E. et al., 2016, ApJL, 819, L25

Alexander, K. D., Wieringa, M. H. et al., 2017, ApJ, 837, 153

Amaro-Seoane, P., Miller, M. C. & Kennedy, G. F., 2012, MNRAS, 425, 2401

Antonini, F., Lombardi, J. C., Jr & Merritt D., 2011, ApJ, 731, 128

Arcavi, I., Gal-Yam, A. et al., 2014, ApJ, 793, 38

Arcavi, I., Wolf, W. M. et al., 2016, ApJ, 819, 35

Armas Padilla, M., Wijnands, R. et al., 2017, ATel, 10224

Auchettl, K., Guillochon, J. & Ramirez-Ruiz, E., 2017, ApJ, 838, 149

Ayal, S., Livio, M. & Piran, T., 2000, ApJ, 545, 772

Bade, N., Komossa, S. & Dahlem, M., 1996, A&A, 309, L35

Balsara, D. S., 1989, Ph.D. Thesis, Univ. Illinois at Urbana-Champaign

Bardeen, J. M., Press W. H. & Teukolsky, S. A., 1972, ApJ, 178, 347

Barnes, J. & Hut, P., 1986, Nature, 324, 446

Bauer, F. E., Treister, E. et al., 2017, MNRAS, 467, 4841

Begelman, M. C., Volonteri, M. & Rees, M. J., 2006, MNRAS, 370, 289

Berger, M. J., & Colella, P., 1989, Journal of Computational Physics, 82, 64

Berger, M. J., & Oliger, J., 1984, Journal of Computational Physics, 53, 484

Bicknell, G. V. & Gingold, R. A., 1983, ApJ, 273, 749

Blagorodnova, N., Gezari, S. et al., 2017, ApJ, 844, 46

Blanchard, P. K., Nicholl, M. et al., 2017, ApJ, 843, 106

Bloom, J. S., Giannios, D. et al., 2011, Science, 333, 203

Bonnerot, C., Price, D. J. et al., 2017, MNRAS, 469, 4879

Bonnerot, C., Rossi, E. M. et al., 2016, MNRAS, 455, 2253

Bower, G. C., Metzger, B. D. et al., 2013, ApJ, 763, 84

Brandt, W. N., Pounds, K. A. & Fink, H., 1995, MNRAS, 273, L47

Brassart, M. & Luminet, J. P., 2008, A&A, 481, 259

Brassart, M. & Luminet, J. P., 2010, A&A, 511, 80

Brockamp, M., Baumgardt, H. & Kroupa, P., 2011, MNRAS, 418, 1308

Bromley, B. C., Kenyon, S. J. et al., 2012, ApJL, 749, L42

Brown, J. S., Holoien, T. W.-S. et al., 2017a, MNRAS, 466, 4904

Brown, J. S., Kochanek, C. S. et al., 2017b, preprint, (arXiv:1704.02321)

Brown, G. C., Levan, A. J. et al., 2015, MNRAS, 452, 4297

Burrows, D. N., Kennea, J. A. et al., 2011, Nature, 476, 421

Campana, S., Mainetti, D. et al., 2015, A&A, 581, A17

Cannizzo, J. K., Lee, H. M. & Goodman, J., 1990, ApJ, 351, 38

Cappelluti, N., Ajello, M. et al., 2009, A&A, 495, L9

Carter, B. & Luminet, J. P., 1983, A&A, 121, 97

Carter, B. & Luminet, J. P., 1985, MNRAS, 212, 23

Cenko, S. B., Bloom, J. S. et al., 2012a, MNRAS, 420, 2684

Cenko, S. B., Cucchiara, A. et al., 2016, ApJL, 818, L32

Cenko, S. B., Krimm, B. et al., 2012b, ApJ, 753, 77

Chen, X., Madau, P. et al., 2009, ApJ, 697, L149

Chen, X., Sesana, A. et al., 2011, ApJ, 729, 13

Cheng, K. S., Chernyshov, D. O. et al., 2016, ApJL, 816, L10

Chornock, R., Berger, E. et al., 2014, ApJ, 780, 44

Churazov, E., Gilfanov, M. et al., 1996, ApJ, 471, 673

Cossins, P. J., 2010, arXiv:1007.1245

Crumley, P., Lu, W. et al., 2016, MNRAS, 460, 396

Cullen, L. & Dehnen, W., 2010, MNRAS, 408, 669

Dai, L., McKinney, J. C. & Miller, M. C., 2015, ApJL, 812, L39

Davis, D. S. & Mushotzky, R. F., 2004, ApJ, 604, 653

Dehnen, W. & Aly, H., 2012, MNRAS, 425, 1068

Denisenko, D., 2017, ATel, 10217

Diener, P., Frolov, V. P. et al., 1997, ApJ, 479, 164

Diener, P., Kosovichev, A. G. et al., 1995, MNRAS, 275, 498

Donato, D., Cenko, S. B. et al., 2014, ApJ, 781, 59

Dong, S., Chen, P. et al., 2016a, ATel, 9843

Dong, S., Shappee, B. J. et al., 2016b, Science, 351, 257

Donley, J. L., Brandt, W. N. et al., 2002, AJ, 124, 1308

Dou, L., Wang, T. et al., 2016, ApJ, 832, 188

Dou, L., Wang, T. et al., 2017, ApJL, 841, L8

Drake, A. J., Djorgovski, S. G. et al., 2011, ApJ, 735, 106

Duquennoy, A. & Mayor, M., 1991, A&A, 248, 485

Esquej, P., Saxton, R. D. et al., 2007, A&A, 462, L49

Esquej, P., Saxton, R. D. et al., 2008, A&A, 489, 543

Esquej, P., Saxton, R. D. et al., 2012, EPJWC, 3902004E

Evans, C. R. & Kochanek, C. S., 1989, ApJ, 346, L13

Evans, P. A., Osborne, J. P. et al., 2014, ApJS, 210, 8

Farrell, S. A., Webb, N. A. et al., 2009, Nature, 460, 73

Feng, H., Ho, L. C. et al., 2015, ApJ, 807, 185

Ferrarese, L. & Ford, H., 2005, Space Sci. Rev., 116, 523

Fischer, D. A. & Marcy, G. W., 1992, AJ, 396, 178

Foley, R. J., Blanchard, P. K. et al., 2015, ATel, 6877

Frank, J. & Rees, M. J., 1976, MNRAS, 176, 633

French, K. D., Arcavi, I. & Zabludoff, A., 2016, ApJL, 818, L21

Gaskell, C. M. & Rojas-Lobos, P. A., 2014, MNRASL, 438, L36

Gelbord, J. M., Mullaney, J. R. & Ward, M. J., 2009, MNRAS, 397, 172

Gezari, S., 2012, EPJ Web Conf., 39, 03001

Gezari, S., Basa, S. et al., 2008, ApJ, 676, 944

Gezari, S., Chornock, R. et al., 2012, Nature, 485, 217

Gezari, S., Halpern, J. P. et al., 2003, ApJ, 592, 42

Gezari, S., Halpern, J. P. et al., 2004, ApJ, 601, 1159

Gezari, S., Heckman, T. et al., 2009, ApJ, 698, 1367

Gezari, S., Martin, D. C. et al., 2006, ApJ, 653, L25

Ghosh, K. K., Suleymanov, V. et al., 2006, MNRAS, 371, 1587

Godoy-Rivera, D., Stanek, K. Z. et al., 2017, MNRAS, 466, 1428

Greene, J. E. & Ho, L. C., 2007, ApJ, 670, 92

Greiner, J., Schwarz, R. et al., 2000, A&A, 362, L25

Gromadzki, M., Hamanowicz, A. & Wyrykowski, L., 2017, ATel, 9977

Grupe, D., Beuermann, K. et al., 1995, A&A, 299, L5

Grupe, D., Komossa, S. & Saxton, R., 2015, ApJL, 803, L28

Grupe, D., Thomas, H. -C. & Leighly, K. M., 1999, A&A, 350, L31

Grupe, D., Wills, B. J. et al., 2004, AJ, 127, 156

Guillochon, J., Manukian, H. & Ramirez-Ruiz, E., 2014, ApJ, 783, 23

Guillochon, J., Ramirez-Ruiz, E. et al., 2009, ApJ, 705, 844

Guillochon, J. & Ramirez-Ruiz, E., 2013, ApJ, 767, 25

Guillochon, J. & Ramirez-Ruiz, E., 2015a, ApJ, 798, 64

Guillochon, J. & Ramirez-Ruiz, E., 2015b, ApJ, 809, 166

Guillochon, J., Ramirez-Ruiz, E. & Lin, D., 2011, ApJ, 732, 74

Hahn, O., Teyssier, R. & Carollo, M., 2010, MNRAS, 405, 274

Halpern, J. P., Gezari, S. & Komossa, S., 2004, ApJ, 604, 572

Hayasaki, K., Stone, N. C. & Loeb, A., 2013, MNRAS, 434, 909

Hayasaki, K., Stone, N. C. & Loeb, A., 2016, MNRAS, 461, 3760

Heintz, W. D., 1969, J. R. Astron. Soc. Can., 63, 275

Hills, J. G., 1975, Nature, 254, 295

Hills, J. G., 1988, Nature, 331, 687

Ho, L. C., 2008, ARA&A, 46, 475

Ho, L. C., Kim, M. & Terashima, Y., 2012, ApJL, 759, L16

Holoien, T. W.-S., Kochanek, C. S. et al., 2016a, MNRAS, 455, 2918

Holoien, T. W.-S., Kochanek, C. S. et al., 2016b, MNRAS, 463, 3813

Holoien, T. W.-S., Prieto, J. L. et al. 2014, MNRAS, 445, 3263

Hongbin, J. & Xin, D., 2005, J. Comput. Physics, 202, 699

Hopkins, P. F., 2013, MNRAS, 428, 2840

Hopkins, P. F., 2015, MNRAS, 450, 53

Hryniewicz, K. & Walter, R., 2016, A&A, 586, A9

Hung, T., Gezari, S. et al., 2017, ApJ, 842, 29

Hut, P. & Makino, J., 1995, ApJ, 443, L93

Irwin, J. A., Brink, T. G. et al., 2010, ApJ, 712, L1

Irwin, J. A., Henriksen, R. N. et al., 2015, ApJ, 809, 172

Ivanov, P. B. & Novikov, I. D., 2001, ApJ, 549, 467

Ivanov, P. B., Polnarev, A. G. & Saha, P., 2005, MNRAS, 358, 1361

Jonker, P. G., Glennie, A. et al., 2013, ApJ, 779, 14

Jonker, P. G., Torres, M. A. P. et al., 2010, MNRAS, 407, 645

Kann, D. A., Greiner, J. & Rau, A., 2011, ATel, 3813

Karas, V. & Šubr, L., 2007, A&A, 470, 11

Kasen, D. & Ramirez-Ruiz, E., 2010, ApJ, 714, 155

Kennea, J. A., Evans, P. A. et al., 2017a, ATel, 10215

Kennea, J. A., Siegel, M. H. et al., 2017b, ATel, 10216

Kesden, M., 2012, Phys. Rev. D, 85, 024037

Khabibullin, I. & Sazonov, S., 2014, MNRAS, 444, 1041

Khokhlov, A., Novikov, I. D. & Pethick, C. J., 1993a, ApJ, 418, 163

Khokhlov, A., Novikov, I. D. & Pethick, C. J., 1993b, ApJ, 418, 181

Kippenhahn R. & Weigert A., 1994, Stellar Structure and Evolution. Springer-Verlag, Berlin

Kobayashi, S., Laguna, P. et al., 2004, ApJ, 615, 855

Kochanek, C. S., 1994, ApJ, 422, 508

Komossa, S., 2012, EPJ Web Conf., 39, 02001

Komossa, S., 2015, J. High-Energy Astrophys., 7, 148

Komossa, S. & Bade, N., 1999, Proceedings of "Highlights in X-ray astronomy", held in Garching, June 1998; B. Aschenbach et al. (eds.)

Komossa, S. & Greiner, J., 1999, A&A, 349, L45

Komossa, S., Halpern, J. et al., 2004, ApJ, 603, L17

Komossa, S., Zhou, H. et al., 2008, ApJ, 678, L13

Kong, A. K. H., Jin, R. et al., 2017, ATel, 10245

Kormendy, J. & Gebhardt, K., 2001, in 20th Texas Symposium On Relativistic Astrophysics, eds. J. C. Wheeler, & H. Martel (New York: Am. Inst. Phys.), AIP Conf. Proc., 586, 363

Kormendy, J. & Richstone, D., 1995, ARA&A, 33, 581

Krimm, H. A., Kennea, J. A. et al., 2011, ATel, 3384

Krolik, J. H. & Piran, T., 2011, ApJ, 743, 134

Lacy, J. H., Townes, C. H. & Hollenbach, D. J., 1982, ApJ, 262, 120

Laguna, P., Miller, W. A. et al., 1993, ApJ, 410, L83

LaMassa, S. M., Cales, S. et al., 2015, ApJ, 800, 144

Laney, C., 1998, Computational Gasdynamics. Cambridge Univ. Press, Cambridge

Latif, M. A., Schleicher, D. R. G. et al., 2013, MNRAS, 433, 1607

Lawrence, A., Bruce, A. G. et al., 2016, MNRAS, 463, 296

Lei, W.-H., Yuan, Q. et al., 2016, ApJ, 816, 20

Leloudas, G., Fraser, M. et al., 2016, Nature Astronomy, 1, 2

Levan, A. J., Tanvir, N. R. et al., 2011, Science, 333, 199

Levan, A. J., Tanvir, N. R. et al., 2016, ApJ, 819, 51

Leveque, R. J., 1998, in Steiner O., Gautschy A., eds, Saas-Fee Advanced Course 27, Computational Methods for Astrophysical Fluid Flow. Springer, Berlin, p. 1

Li, L.-X., Narayan, R. & Menou, K., 2002, ApJ, 576, 753

Lightman, A. P. & Shapiro, S. L., 1977, ApJ, 211, 244

Lin, D., Carrasco, E. R. et al., 2011, ApJ, 738, 52

Lin, D., Godet, O. et al., 2017a, MNRAS, 468, 783

Lin, D., Guillochon, J. et al., 2017b, Nature Astronomy, 1, 0033

Lin, D., Irwin, J. A. et al., 2013, ApJL, 776, L10

Lin, D., Maksym, W. P. et al., 2015, ApJ, 811, 43

Liu, S.-F., Guillochon, J. et al., 2013, ApJ, 762, 37

Liu, F. K., Li, S. & Komossa, S., 2014, ApJ, 786, 103

Lodato G., 2012, EPJ Web Conf., 39, 01001

Lodato, G., King, A. R. & Pringle, J. E., 2009, MNRAS, 392, 332

Lodato, G. & Rossi, E. M., 2010, MNRAS, 476, 359

Luminet, J. P. & Carter, B., 1986, ApJS, 61, 219

Luminet, J. P. & Marck, J. -A., 1985, MNRAS, 212, 57

Luminet, J. P. & Pichon, B., 1989, A&A, 209, 85

MacLeod, M., Ramirez-Ruiz, E. & Guillochon, J., 2012, ApJ, 757, 134

MacLeod, M., Ramirez-Ruiz, E. et al., 2013, ApJ, 777, 133

Madau, P. & Rees, M. J., 2001, ApJ, 551, L27

Magorrian, J. & Tremaine, S., 1999, MNRAS, 309, 447

Mainetti, D., Campana, S. & Colpi, M., 2016a, A&A, 592, A41

Mainetti, D., Lupi, A. et al., 2016b, MNRAS, 457, 2516

Mainetti, D., Lupi, A. et al., 2017, A&A, 600, A124

Maksym, W. P., Lin, D. & Irwin, J. A., 2014a, ApJL, 792, L29

Maksym, W. P., Ulmer, M. P. & Eracleous, M., 2010, ApJ, 722, 1035

Maksym, W. P., Ulmer, M. P. et al., 2013, MNRAS, 435, 1904

Maksym, W. P., Ulmer, M. P. et al., 2014b, MNRAS, 444, 866

Mandel I. & Levin Y., 2015, ApJ, 805, L4

Mangano, V., Burrows, D. N. et al., 2016, ApJ, 817, 103

Manukian, H., Guillochon, J. et al., 2013, ApJ, 771, L28

Margutti, R., Metzger, B. D. et al., 2017, ApJ, 836, 25

Marinucci, A., Matt, G. et al., 2015, MNRAS, 447, 160

Mayer, L., 2017, Nature Astron., 1, 0108

Merloni, A., Dwelly, T. et al., 2015, MNRAS, 452, 69

Merloni, A. & Heinz, S., 2013, in Extragalactic Astronomy and Cosmology, ed. W. Keel, Stars and Stellar Systems, Planets (Springer), 6, 503

Merritt, D., 2013, Classical and Quantum Gravity, 30, 244005

Merritt, D. & Poon, M. Y., 2004, ApJ, 606, 788

Miller, M. C., Freitag, M. et al., 2005, ApJ, 631, L117

Miller, M. C. & Hamilton, D. P., 2002, MNRAS, 330, 232

Miller, J. M., Kaastra, J. S. et al., 2015, Nature, 526, 542

Monaghan, J. J., 1992, ARA&A, 30, 543

Monaghan, J. J. & Lattanzio, J. C., 1985, A&A, 149, 135

Moran, E. C., Barth, A. J. et al., 2007, ApJ, 668, L31

Munoz-Darias, T., Jimenez-Ibarra, F. et al., 2017, ATel, 10221

Narayan, R., 2004, arXiv:astro-ph/0411385

Negoro, H., Kawamuro, T. et al., 2017, ATel, 10208

Nikołajuk, M. & Walter, R., 2013, A&A, 552, A75

Nolthenius, R. A. & Katz, J. I., 1982, ApJ, 263, 377

Öpik E., 1924, Publ. Tartu Astrofizica Obs., 25, 1

Osterbrock, D. E. & Pogge, R. W., 1985, ApJ, 297, 166

Palaversa, L., Gezari, S. et al., 2016, ApJ, 819, 151

Pasham, D. R., Cenko, S. B. et al., 2015, ApJ, 805, 68

Peebles, P. J. E., 1972, ApJ, 178, 371

Peery, K. & Imlay, S., 1988, Blunt-body flow simulations (American Institute of Aeronautics and Astronautics), 2904+

Peng, F.-K., Tang, Q.-W. & Wang, X.-Y., 2016, ApJ, 825, 47

Perets, H. B., Hopman, C. & Alexander, T., 2007, ApJ, 656, 709

Perets, H. B., Li, Z. et al., 2016, ApJ, 823, 113

Perley, R. A., Röser, H.-J. & Meisenheimer, K., 1997, A&A, 328, 12

Phinney, E. S., 1989, in Proc. 136th IAU Symp, The Center of the Galaxy

Piran, T., Svirski, G. et al., 2015, ApJ, 806, 164

Poon, M. Y. & Merritt, D., 2004, ApJ, 606, 774

Portegies Zwart, S. F. & McMillan, S. L. W., 2002, ApJ, 576, 899

Price, D. J., 2005, arXiv (astro-ph/0507472)

Price, D. J., 2012, in Astronomical Society of the Pacific Conference Series, Vol. 453, Advances in Computational Astrophysics: Methods, Tools, and Outcome, ed. R. Capuzzo-Dolcetta, M. Limongi, & A. Tornambe', 249

Ptak, A. & Griffiths, R., 1999, ApJ, 517, L85

Ramirez-Ruiz, E. & Rosswog, S., 2009, ApJL, 697, L77

Rauch, K. P. & Ingalls, B., 1998, MNRAS, 299, 1231

Rauch, K. P. & Tremaine, S., 1996, New Astron., 1, 149

Ravi, V. & Shannon, R. M., 2015, ATel, 6904

Read, A. M., Saxton, R. D. & Esquej, P., 2011a, ATel, 3811

Read, A. M., Saxton, R. D. & Esquej, P., 2011b, ATel, 3821

Rees, M. J., 1988, Nature, 333, 523

Regan, J. A., Visbal, E. et al., 2017, Nature Astron., 1, 0075

Rosswog, S., Ramirez-Ruiz, E. & Hix, W. R., 2008, ApJ, 679, 1385

Rosswog, S., Ramirez-Ruiz, E. & Hix, W. R., 2009, ApJ, 695, 404

Runnoe, J. C., Cales, S. et al., 2016, MNRAS, 455, 1691

Sani, E., Lutz, D. et al., 2010, MNRAS, 403, 1246

Saxton R. D., Motta S. E. et al., 2015, MNRAS, 454, 2798

Saxton, R. D., Read, A. M. et al., 2008, A&A, 480, 611

Saxton, R. D., Read, A. M. et al., 2012, A&A, 541, A106

Saxton, R. D., Read, A. M. et al., 2017, A&A, 598, 29

Schlegel, D. J., Finkbeiner, D. P. & Davis, M., 1998, ApJ, 500, 525

Sesana A., Madau P. & Haardt F., 2009, MNRAS, 392, 31

Shakura, N. I. & Sunyaev, R. A., 1973, A&A, 24, 337

Shidatsu, M., Tachibana, Y. et al., 2017, ATel, 10222

Shields, J., Stanek, K. Z. et al., 2017, ATel, 10227

Shiokawa, H., Krolik, J. H. et al., 2015, ApJ, 804, 85

Smartt, S. J., Valenti, S. et al., 2015, A&A, 579, A40

Smith, K. W., Wright, D. et al., 2016, ATel, 9401

Sokolovsky, K., Wyrzykowski, L. et al., 2017, ATel, 10006

Soltan, A., 1982, MNRAS, 200, 115

Spitzer, L., 1987, Dynamical evolution of globular clusters. Princeton, NJ, Princeton University Press, 1987, 191 p.

Springel, V., 2005, MNRAS, 364, 1105

Springel, V., 2010, MNRAS, 401, 791

Stanway, E. R., Levan, A. J. & Brown, G. C., 2017, ATel, 10025

Stone, N. C., 2013, Tidal Disruption of Stars by Supermassive Black Holes. Doctoral dissertation, Harvard University

Stone, N. C. & Loeb, A., 2011, MNRAS, 412, 75

Stone, N. C. & Metzger, B. D., 2016, MNRAS, 455, 859

Stone, N. C., Sari, R. & Loeb, A., 2013, MNRAS, 435, 1809

Storchi-Bergmann, T., Eracleous, M. et al., 1995, ApJ, 443, 617

Strotjohann, N. L., Saxton, R. D. et al., 2016, A&A, 592, A74

Strubbe, L. E. & Murray, N., 2015, MNRAS, 454, 2321

Strubbe, L. E. & Quataert, E., 2009, MNRAS, 400, 2070

Strubbe, L. E. & Quataert, E., 2011, MNRAS, 415, 168

Strüder, L., Briel, U. et al., 2001, A&A, 365, L18

Sulentic, J. W., Marziani, P. et al., 1995, ApJ, 438, L1

Tachibana, Y., Yoshii, T. et al., 2017, ATel, 10223

Tadhunter, C., Spence, R. et al., 2017, Nature Astronomy, 1, 0061

Terashima, Y. & Wilson, A. S., 2003, ApJ, 583, 145

Truelove, J. K., Klein, R. I. et al., 1997, ApJ, 489, L179

Turner, M. J. L., Abbey, A. et al., 2001, A&A, 365, L27

Ulmer, A., 1999, ApJ, 514, 180

van Velzen, S., Anderson, G. E. et al., 2016, Science, 351, 62

van Velzen, S., Farrar, G. R. et al., 2011, ApJ, 741, 73

Vaughan, S., Edelson, R. & Warwick, R. S., 2004, MNRAS, 349, L1

Vestergaard, M. & Osmer, P. S., 2009, ApJ, 699, 800

Vinkò, J., Yuan, F. et al., 2015, ApJ, 798, 12

Volonteri, M., 2010, Nature, 466, 1049

Wadsley, J. W., Veeravalli, G. & Couchman, H. M. P., 2008, MNRAS, 387, 427

Wang, J. & Merritt, D., 2004, ApJ, 600, 149

Wang, T.-G., Zhou, H.-Y. et al., 2011, ApJ, 740, 85

Wang, T.-G., Zhou, H.-Y. et al., 2012, ApJ, 749, 115

Warner, B., 2002, AIP Conf. Ser., 637, 3

Wevers, T., van Velzen, S. et al., 2017, MNRAS, 471, 1694

Wilson, A. S., Young, A. J. & Shopbell, P.L., 2001, ApJ, 547, 740

Wolter, A., Trinchieri, G. & Colpi, M., 2006, MNRAS, 373, 1627

Wyrzykowski, Ł., Zieliński, M. et al., 2017, MNRAS, 465, L114

Yang, C.-W., Wang, T.-G. et al., 2013, ApJ, 774, 46

Yu, Q. & Tremaine, S., 2002, MNRAS, 335, 965

Yu, W., Yan, Z. & Zhang, W., 2015, ATel, 6887

Zauderer, B. A., Berger, E. et al., 2011, Nature, 476, 425